2021

Impact of Targeting Glycosylated Ceramides on Tumorigenic Properties, and Characterization of Sphingolipids in Head and Neck Tumors

Katherine E. Hylton
Virginia Commonwealth University

Impact of Targeting Glycosylated Ceramides on Tumorigenic Properties, and Characterization of Sphingolipids in Head and Neck Tumors

A thesis submitted in partial fulfillment of the requirements for the degree of Master of Science in Biology at Virginia Commonwealth University.

By:

Katherine Elizabeth Hylton

BS: Biological Sciences – North Carolina State University

P.I.: Santiago Lima, PhD

Assistant Professor, Virginia Commonwealth University

Virginia Commonwealth University

Richmond, Virginia

August 2021

Acknowledgments

Completing this degree has been a challenging but rewarding experience, and I believe my time at VCU has provided me with the academic and scientific rigor that has helped me become a better biologist. I would like to thank my P.I., Dr. Santiago Lima, for the opportunity to work in his lab and for his guidance throughout the past two years. His encouragement, honesty, insight, patience, and support have been vital to my growth and maturation as a scientist. I also thank my committee members Dr. Jason Newton, Dr. Derek Prosser, and Dr. Sarah Rothschild for providing insightful feedback and dedicating their time to help me develop and present my research. I truly appreciate my fellow MS lab mates Crystal Turner and April Boyd, who were a wonderful source of camaraderie, my study buddies, and ever-patient ears to my questions. Thank you to Madisyn Rigsby for showing me the ropes when I first joined the lab. I would also like to express my gratitude to the lab postdoc, Dr. Andrea Anderson, who was ceaselessly kind and helpful, and brought a smile to my face every day. Finally, I would like to express my deep gratitude to my external support network. My parents, David Hylton and Robin Smith, have always provided me with unconditional love and encouragement, and my boyfriend John Rorie has been an unwavering source of support throughout my graduate journey. A sincere thank you to all of you for helping me to get to the point where I am today.

Table of Contents

List of Tables and Figures

Chapter 1 Tables

Chapter 1 Figures

Chapter 2 Tables

Chapter 2 Figures

Abstract

Sphingolipids play a crucial role in signaling, membrane structure, and migration, making them important molecules in cancer development, metastasis, and drug resistance. While some sphingolipids have been associated with pro-apoptotic or pro-survival behaviors, the role of many sphingolipids in cancer remains poorly defined. Chapter 1 of this study investigated the impact of three enzymes that compose most of the ceramide to Lc3 ceramide pathway – UGCG, GBA, and B3GNT5 – and how their alteration impacts chemoresistance and basal membrane invasion *in vitro*. It was found that the CBE-induced inhibition of GBA, which converts glucosylceramide to ceramide, has no effects on invasion or on chemotherapeutic resistance to cisplatin or vinorelbine. UGCG, which converts ceramide to glucosylceramide, can be inhibited by eliglustat and PPMP. PPMP treatment at higher concentrations caused decreased viability in lung adenocarcinoma compared to lung squamous carcinoma, and when in combination with vinorelbine, PPMP caused reduced viability in colon adenocarcinoma, a trend not seen in colon carcinoma. Changes in cellular behavior demonstrated in response to PPMP, but not eliglustat, suggest that the response may be attributed to the off-target inhibition of ACS, and not UGCG itself. Interestingly, both PPMP and high concentrations of eliglustat increased levels of transwell invasion in colon adenocarcinoma. CRISPR-Cas9 induced partial knockout of B3GNT5, which is the sole enzyme converting lactosylceramide to Lc3 ceramide, did not affect transwell invasion, but it did result in higher resistance to vinorelbine in combination with PPMP. An acyl-chain analysis of sphingolipid species in the altered cell line found increased C24:1 at all tested species, and increased glucosylceramide and lactosylceramide. Chapter 2 of this study analyzed sphingolipid acyl chain length in normal and tumor head and neck tissue, finding C16, C24:1, and C24 are significantly raised in tumor tissue, with C24:1 Cer and MonoHex significantly increased only in African Americans. Comparison of normal tissues indicated that Caucasians had significantly more C16 LacCer and C24:1 Cer than African Americans, which could be correlated to poorer head and neck cancer prognosis in African Americans. In tumor tissue, C16 SM and C24:1 LacCer were significantly higher in females than males. Together, these two chapters further cancer sphingolipid research by recognizing PPMP and vinorelbine as a potential co-treatment to increased chemotherapeutic cytotoxicity, discovering that reduced B3GNT5 raises GlcCer levels in cervical cancer, and identifying acyl chain lengths that may serve as future markers of cancer diagnosis and prognosis.

Introduction

Sphingolipids

Sphingolipids, a class of lipid once thought to only play a role in cellular membrane structure, have been found to be key regulators of signaling for cell growth, metastasis, proliferation, senescence, and cell death (1). Sphingolipids are fundamentally composed of a fatty amino alcohol called a sphingoid base (typically sphingosine) amide-linked to a fatty acid chain (2, 3). The high variability of sphingolipid function comes from the varying headgroups, which can range from a single hydrogen (making ceramide) to complex glycoconjugates. In the *de novo* pathway, sphingoid base synthesis begins with the condensation of palmitate and serine by serine palmitoyl transferase, making 3-keto-dihydrosphingosine, which is then reduced to dihydrosphingosine (2, 4). Ceramide synthases then amino-acylate the dihydrosphingosine with a carbon chain of varying length, creating various dihydroceramide species (2). The desaturation of dihydroceramide results in ceramide, which is considered the center of the sphingolipid biosynthesis pathway and is the precursor to many complex sphingolipids (2, 4). In alternative methods of ceramide generation, sphingomyelin (SM) in the plasma membrane can be metabolized to Cer via SMases. The endosomal (salvage) pathway can also degrade both SM and GlcCer (by SMases and glucosidases, respectively) back to Cer, which is further degraded by acid CDase to sphingosine, which can leave the lysosome and move between membranes, allowing it to re-enter ceramide synthesis pathways (4).

Glycosphingolipids are composed of a ceramide attached to a sugar moiety via a β-glycosidic bond and are the major glycolipids of animals (5). These molecules can vary widely in complexity and function, being composed of one to up to twenty sugar residues, and can include twelve different sugars (5). They are located on the outer leaflet of the plasma membrane, often

in lipid rafts, where they function in *trans* by mediating cell-cell interactions—they also operate in *cis* by regulating protein activities in the plasma membrane (5, 6). Lipid rafts of heterogeneous glycosphingolipids—sometimes referred to as glycosynapses—hold many presumed functions, including clustering and regulating signaling and adhesion molecules, as well as organizing cargo sorting for both secretory and endocytic pathways (5). These reactions are all carbohydrate-dependent, and can trigger cellular signaling pathways to alter phenotype through motility, activation, and growth (7). While glycosphingolipids are not necessary for life to exist, they are required for the development of multicellular eukaryotes (5).

Glycosphingolipids in cancer

Aberrant expression of glycosphingolipids has been associated with cancer transformation, malignancy, and drug resistance (8, 9). Several glycosphingolipids have been identified as prognostic markers, and the upregulation of some sphingolipid synthases has been associated with chemotherapeutic resistance (10). In breast cancer, for example, several glycosphingolipids, such as the gangliosides GD2 and GD3, have been identified as prognostic markers, while upregulation of GD3 synthase ST8SIA1 may be involved in gefitinib resistance (10, 11). Similarly, Gg4 and its synthase B3GALT4 have been found to be significantly reduced during TGF-β induced epithelial-mesenchymal transition (EMT), which plays a crucial role in cancer cell metastasis (12). In non-small cell lung cancer, increased expression of Gb3 on the cell surface leads to cisplatin resistance, while reduced glucosylceramide synthase (UGCG) expression leads to cisplatin cytotoxicity (13). In both lung and colorectal cancer, α-galactosylceramide (α-GalCer) has been identified to exert an anti-tumor effect and increases expression of tumor growth suppressor IFN-γ (interferon gamma) in natural killer T cells (10, 14). Aberrant glycosphingolipid levels have been identified as a molecular marker or associated

with cancer phenotypes in melanoma, leukemia, and ovarian cancers, with preliminary research also indicating GSL plays a role in bladder, renal, gastric, and prostate cancers (10). Given current knowledge on the associations between GSLs and cancer, as well as the function of GSLs in cellular signaling, cell-cell communication, and protein modulation, understanding how these molecules contribute to tumorigenesis, metastasis, and drug resistance may offer novel approaches to cancer treatment in a variety of tumor types.

B3GNT5 and Lc3 ceramide

In the *de novo* pathway, ceramide (Cer) is formed on the cytosolic surface of the endoplasmic reticulum and is transported by the protein FAPP2 to the cytosolic leaflets of the Golgi, where it is glycosylated by UGCG to become glucosylceramide (GlcCer) (4). Once GlcCer is translocated to the luminal Golgi via the ABC transporter protein MDR-1 (also known as P-glycoprotein), it is galactosylated to create lactosylceramide (LacCer) (4). LacCer is a metabolic branching point for the creation of many complex glycosphingolipids; from here, the molecule can produce the asialo, ganglio, globo, isoglobo, lacto, or neo-lacto sphingolipid series (5, 11). Lactotriaosyl ceramide (Lc3Cer) is synthesized by B3GNT5 via the transfer of N-acetylglucosamine from UDP-N-acetyl-D-glucosamine to LacCer (15, 16). Lc3Cer is the precursor molecule to all lacto- and neo-lacto-series of glycolipids, which are prominent in secretory and hematopoietic tissues, respectively (Figure 1) (6). Lc3Cer is expressed in most human tissues and is preferentially expressed on the cell surface (16).

B3GNT5, or β1,3-galactosyltransferase 5, was identified and structurally classified by Togayachi et al. in 2001 (17). The protein was predicted to be a class-II transmembrane enzyme located in the Golgi membrane, consisting of an NH2 terminal cytoplasmic domain, a

transmembrane segment, and large stem region and catalytic domain (17). B3GNT5 is the sole synthase for Lc3 ceramide (18). The *B3GNT5* gene is expressed in almost all human tissues, though at varying levels. Notably high levels are found in areas including the lung, colon, placenta, testis, and cerebellum (17).

While not much literature has been published on B3GNT5 with respect to cancer, the gene is a promising target for cancer research. High expression of the gene is a marker of poor prognosis in renal, pancreatic, and liver cancers, and lung cancer patients with high expression of *B3GNT5* had a significantly lower survival rate than patients with a low level of expression (19). Similarly, high levels of *B3GNT5* expression were observed in malignant breast cancer and negatively associated with patient prognosis (9). Patients with acute myeloid leukemia exhibited a significantly higher amount of Lc3Cer in their bone marrow, with 16-fold higher expression levels of *B3GNT5* compared to normal patients (20). High *B3GNT5* expression has also been identified in glioblastoma and has been attributed to a hypomethylated promoter (21). When profiling genes associated with non-small cell lung cancer, concordant differences were found in expression level and copy number for B3GNT5 between adenocarcinoma and squamous cell carcinoma (22). *B3GNT5* is also highly overexpressed in primary and metastatic pancreatic cancer cells and may be associated with high keratan sulfate expression in these tumors, which has been correlated with lower rates of pancreatic cancer patient survival (23). In The Cancer Genome Atlas's PanCan genomic meta-analysis of 32 cancer types, alterations of the *B3GNT5* gene occurred in more than 10% of cases in seven different cancer types, with the majority of alterations being amplifications (Figure 2) (The cBio Cancer Genomics Portal, www.cbioportal.org) (24).

Gastric infection by *Helicobacter pylori* causes chronic inflammation, and 1-3% of cases lead to gastric cancer, typically the Lauren intestinal-type gastric adenocarcinomas. In comparing gastric samples from *H. pylori* infected and non-infected patients, patients with infection demonstrated a significantly higher level of *B3GNT5* expression (25). Subsequent studies later showed that *H. pylori* infection remodels the glycosylation profile of the gastric mucosa, causing an increase in α 2,3 sialylation, sialyl-Lewis X, and sialyl-Lewis A. Infected patients presented significantly increased amounts of the cytokines IL-6, IL-8, IFN-γ, and TNF-α. TNF-α is recognized as an activator of NF-κB, a nuclear transcription factor, as it binds to the NF-κB inhibitor IκB and phosphorylates it, flagging it for degradation. Bioinformatic analysis indicates that the promoter for *B3GNT5* presents several highly conserved possible binding sites for NF-κB, thus suggesting that increase of the TNF- α in the gastric mucosa in response to *H. pylori* infection may trigger upregulation of the *B3GNT5* gene (26). Due to the intricate connections between B3GNT5 and signaling molecules, its frequency of mutation in some cancers, and its role as the sole precursor to the lacto- and neolacto series of sphingolipids, B3GNT5 offers a promising venue for cancer study.

Ceramide and Glucosylceramide

Upstream of Lc3Cer, one of its precursors, GlcCer, demonstrates impact of aberrant sphingolipid levels. Cer is converted to GlcCer via UDP-Glucose Ceramide Glucosyltransferase (UGCG), and the GlcCer is converted back to Cer by Glucosylceramidase 1 (GBA) (27). Cer levels are often increased in response to cellular stress and can cause apoptosis and cell cycle arrest, behaviors that can prevent the growth of cancer. However, the formation of GlcCer by UGCG reduces the amount of available Cer, and thus reduces the apoptotic potential of cancer cells; as a result, UGCG is overexpressed in many chemoresistant cancers (28). GBA expression,

on the other hand, has not been significantly associated with cancer phenotypes. Loss-of-function mutations in the GBA1 gene are the cause of Gaucher disease, a lysosomal storage disorder. The disease has been associated with a higher likelihood of cancer, further suggesting the correlation between GlcCer and malignancy (27). Conduritol-β-Epoxide (CBE) is an irreversible inhibitor of GBA which is often used to mimic Gaucher disease, while eliglustat tartrate (eliglustat) is an inhibitor of UGCG used as treatment for Gaucher disease (29). Along with DL-threo-1-Phenyl-2-palmitoylamino-3-morpholino-1-propanol (PPMP), which also inhibits UGCG, these drugs can be used to study the effects of UGCG or GBA dysregulation on cancer behavior (1). Alternatively, UGCG inhibiting drugs could be utilized as a chemotherapeutic co-treatment to reduce cancer drug resistance.

Sphingolipid chain length in cancer

Ceramide is likely the most-studied sphingolipid, as it is the precursor to most complex sphingolipids. Numerous studies have suggested that ceramide has pro-apoptotic, and thus anti-cancerous, properties (1, 27). However, the quantification of ceramide chain lengths has suggested that the acyl chain length of the molecule may dictate the pro- or anti-apoptotic properties of ceramide (30-32). There are six ceramide synthases (CerS1-6), which form dihydroceramide from dihydrosphingosine and acyl-CoA in the *de novo* pathway or ceramide from sphingosine and acyl-CoA in the salvage pathway (4, 33). Each synthase is specific to a few acyl chain lengths. CerS1 has a substrate specificity towards C18:0 and C18:1 acyl-CoAs and is expressed largely in the brain and testis (34). CerS1 expression has been associated with pathogenesis of head & neck squamous cell carcinoma (30). CerS2 is the most ubiquitous and abundant, appearing in most tissues: It has substrate specificity for C20, C22, C24:0, C24:1, and C26:0 acyl-CoAs (35). Because CerS2 creates long-chain ceramides, it is critical for cellular

function, but it appears to be tissue dependent regarding whether it is up- or downregulated in cancers. Cer3 has a limited distribution, occurring in the gastrointestinal tract, bone marrow, thyroid, skin, and testes, but it has the broadest substrate specificity, using C18 to C26:0 acyl-CoAs (34). CerS4 is most prominent in the skin and has a substrate specificity towards C18:0 and C20:0 acyl-CoAs. Multiple studies have found CerS4 mRNA to be upregulated in estrogen-receptor positive breast cancer (32); however, increased levels of C18 and C20 ceramides have also been found to promote apoptosis (36). CerS5, which is abundant in the brain, has substrate specificity to C14 and C16 acyl-CoA, but has some specificity to C18:0 as well – mRNA overexpression of the enzyme has been found in several cancers (34). CerS6 has a broad but low distribution and substrate specificity for C14:0 and C16:0 acyl-CoA and has also been found to be overexpressed in many cancers (34). Investigating sphingolipids by chain length may indicate misregulation of specific CerS or may identify specific chain lengths involved in pro-cancerous behavior.

Aims

Aim 1: To optimize the transwell invasion technique for studying the role of sphingolipids in cellular invasion. In this aim, I will develop a protocol for transwell invasion assays that is consistent and cost-effective, resulting in an in vitro model of basal membrane invasion. Given the wide variety of published transwell assay protocols, I will optimize a transwell invasion assay protocol for cancer cells based on common techniques and optimizing components such as membrane composition, cell seeding density, and incubation time.

Aim 2: To study if drugs targeting the ceramide-to-glucosylceramide pathway impact chemotherapeutic cytotoxicity. In this aim, I will determine optimal test concentrations for the drugs eliglustat and PPMP, which inhibit UGCG, and CBE, which inhibits GBA. I will then test a low, medium, and high concentration of the drug combined with the chemotherapeutic cisplatin or vinorelbine at a range of concentrations and quantify cell viability via CCK-8 assay. Viability will be compared across concentrations of drug.

Aim 3: To examine if the knockout of *B3GNT5* via CRISPR-Cas9 in cancer cell lines results in decreased metastatic potential and drug resistance. In this aim, I will examine how decreasing expression of the *B3GNT5* gene via CRISPR-Cas 9 knockout in cancer cells impacts metastatic migration and resistance to chemotherapeutics. To accomplish this, the *B3GNT5* gene will be knocked out of the genome of cancer cell lines with a commercially available CRISPR-Cas9 kit. Western blotting will be performed to confirm successful knockout. Metastatic potential will then be measured via a Transwell invasion assay, where the percent migration of cells through a Matrigel covered membrane (to simulate extracellular matrix) is quantified and compared to the migration of non-knockout cell lines. Knockout *B3GNT5* cells will also be compared to control cells via an CCK-8 cytotoxicity assay, where concentrations of

chemotherapeutic will be administered to cells, and the amount of metabolic activity will be subsequently quantified via spectrophotometry. Changes in sphingolipid abundance in response to knockout will be observed by mass spectrometry (MS).

Aim 4: To investigate if human head and neck cancers have altered sphingolipid levels compared to normal head and neck tissues, and identify race dependent sphingolipid levels. In this aim, I will study paired tumor and normal adjacent uninvolved head and neck tissues collected from African American and Caucasian American patients at the VCU Health Tissue and Data Acquisition and Analysis Core (TDAAC). MS will be performed on the tissues to quantify sphingolipid concentrations and varying chain lengths, and variations in sphingolipid abundance will be quantified using AB Sciex Analyst 1.6.2. Additionally, samples will be analyzed by race and gender to observe any differences in sphingolipid levels.

Chapter 1: Impact of Targeting Glycosylated Ceramides on Tumorigenic Properties

Methods

Cell Culture

Several different human cell lines were used in this research. H460 cells were derived from large cell lung carcinoma, HCT116 cells were derived from colorectal carcinoma, HT29 cells were derived from colorectal adenocarcinoma, SKLU-1 cells were derived from lung adenocarcinoma, SK-MES-1 cells were derived from metastatic lung squamous cell carcinoma, HN12 cells were derived from head and neck carcinoma, and HeLa cells were derived from cervical adenocarcinoma. HBEC cells are derived from human bronchial epithelial cells, and HEK293FT cells are derived from human embryonic kidney cells transformed with SV40 large T antigen (37). SALE cells are derived from small airway epithelial cells, and SALEK cells are SALE cells expressing a mutated KRAS protein (38). All cell lines were maintained using aseptic technique in a Type IIa biosafety cabinet and kept in an incubator set to 37 °C and 5% CO_2. A list of cell types with culture media is presented in Table 1.

Transwell Invasion Assay

To prepare the Matrigel membrane needed for the Transwell Invasion Assay, tips, a 24 well cell culture plate, Millicell 8.0 µm Culture Plate Inserts (12 mm diameter, Cat #: PI8P01250), and serum-free medium were pre-chilled to 4 °C. Matrigel solidifies to a gel at room temperature, making it imperative that it is handled and kept on ice to prevent premature gelling. On ice in a biosafety cabinet, each insert was removed from packaging and placed in a well of 24-well plate using sterile tweezers. An aliquot of Matrigel Growth Factor Reduced (Corning, Cat.#356230) was thawed under cold running water, then diluted in serum-free

medium at a ratio of 1:2. Using pre-chilled tips, 45 µL of diluted Matrigel was manually added to the center of each insert. Any bubbles in the Matrigel can cause uneven distribution, so any bubbles accidentally added were immediately removed via gentle pipetting. A pre-chilled tip and gentle rocking were used to spread the Matrigel to ensure complete membrane coverage. After the Matrigel dilution was evenly distributed, the plate was incubated at 37 °C for 1 hour for the Matrigel to solidify. Once Matrigel solidified, the assay was performed. Cells were detached from their culture plate using Tryspin/EDTA, then trypsin was inactivated using complete media containing fetal bovine serum (FBS). The tube was centrifuged for 2 minutes at 400 x g to pellet the cells, the media was aspirated, and the pellet was resuspended in serum-free media. The cells were washed a second time by re-spinning and aspirating and were resuspended in serum-free media. The cellular concentration was then diluted to the intended seeding density (i.e. 100,000 cells/well) and 200 µL of the cells are added to the inner chamber of the insert. To the outer chamber (between the insert and the well wall), 500 µL of media with 10% FBS was added, as FBS serves as the chemoattractant to promote transmembrane migration. After confirmation that there were no bubbles and no inserts were floating, the plate was incubated at 37 °C and 5% CO_2 for 24-72 hours (cell type dependent).

Note: Repeated freeze-thawing of Matrigel should be avoided to preserve integrity. Stock Matrigel was divided on ice into working volume aliquots (200 or 500 µL) to be thawed as needed under cold running water and kept on ice.

To fix and stain the inserts for observation and quantification, the media and residual Matrigel were aspirated from both the inner and outer chamber. 500 µL of 70% ethanol was then added to the outer chamber of each well for 15 minutes at ambient temperature to fix the cells to the membrane. After this step, all subsequent steps may be performed outside of the biosafety

cabinet if desired. The inserts were transferred to a new well on the plate to dry, then a damp cotton swab was used to gently but thoroughly remove any residual cells or Matrigel on the top of the membrane. To stain the cells, 250 µL 0.5% crystal violet (in distilled water and filtered) was added to the outer chamber and allowed to incubate for 30 minutes. The insert was then thoroughly rinsed in water to remove excess stain. When needed, a damp cotton swab was used to remove residual stain on the interior of insert, which was then rinsed in a second beaker of water. After drying, inserts were inverted and imaged via dissecting microscope.

To quantify invasion via spectrophotometry, the dried insert was placed in a clean well and 250 µL of 33% acetic acid was added to the outer chamber, incubating for 10 minutes on a shaking plate at ambient temperature. The insert was drained and discarded, and 100 µL of the eluate was transferred to a 96-well microplate, which was measured on at plate spectrophotometer at 595 nm optical density.

CCK-8 Assay

In the morning, 10,000 cells in 100 µL complete media were seeded per well of a 96 well tissue culture microplate. In the afternoon, all test compounds were added to the cells in triplicate, ensuring that equal volumes of vehicle are added to each well and that dimethyl-sulfoxide (DMSO), if the vehicle, does not exceed 1.5% of total well volume. Blank wells contained 100 µL of complete media. Cells were incubated 72 hours in an incubator set to 37 °C, 5% CO_2. To quantify the amount of living cells, 10 µL of Cell Counting Kit-8 (CCK-8) solution was added to each well and incubated at 37 °C. A microplate reader was used to measure the absorbance at 460 nm, with measurements started 15 minutes post CCK-8 addition and taken in 15 minute intervals thereafter. Calculation of percent survival was performed by subtracting the

mean absorbance from the blank from the mean absorbance of each well, then dividing the test value by the control value. An ANOVA statistical test was performed to determine significance.

Lysate collection

Collecting cell lysate was necessary for both protein quantification/Western blotting and MS. After prechilling all reagents, the culture plate was set on ice, the culture medium was aspirated, and cells were washed with phosphate buffered saline (PBS). For MS, 200 µL of PBS with Halt (ThermoFisher Cat # 78429), a protease inhibitor, was added to the plate, while samples for Western blotting received 200 µL of TNE with Halt. TNE buffer was composed of 20 mM HEPES pH 7.4, 250 mM NaCl, 1% Triton X-100, 1 mM DTT, 1mM EDTA, and 20% glycerol. The cells were manually detached from the plate using a cell scraper. For MS, 100 µL of the resuspended cells were added to a mass spectrometry tube containing 1 mL of 4 °C methanol. Residual cells were then used for quantification. The samples were pulse sonicated at 25% intensity, then centrifuged for 10 minutes at 4 °C and 4,122 x g. The supernatant was transferred to a new tube for quantification.

Bradford Protein Assay

To quantify protein concentration, 1 µL of sample lysate was added to 200 µL of 1X Bradford reagent (BioRad Cat. #5000006) in a 96 well plate, then run in a microplate reader at 595 nm (performed in triplicate). Protein concentration was calculated by the formula derived from a pre-established standard curve:

$$[\text{Concentration in mg/mL}] = ([\text{average absorbance}] - 0.3384)/0.1225$$

For Western blotting, all samples were diluted to the concentration of the least concentrated sample, and Bradford assay was repeated until all samples were approximately equal concentrations.

TCA precipitation

For an alternative method of Western blotting, Bradford quantified protein samples were precipitated instead of being diluted to equal concentrations. After quantification, 0.11X volume of 10% trichloroacetic acid (TCA) in water was added to each sample, which was then vortexed and kept on ice for 30 minutes. Samples were spun at 4,122 x g for 10 minutes at 4 °C, and supernatant was discarded. The pellet was resuspended in 4X western blot dye (diluted into 1X in 1M Tris-HCl pH 7.8) and incubated at 80 °C on a shaking plate at 10,000 rpm for 10 minutes. Samples loaded to Western blot each had the same amount of protein added to each well, so less concentrated samples had a higher volume loaded, and vice versa.

Western Blotting

Samples were mixed with 4X Western Blot Loading Buffer (250 mM Tris-HCl, 500 mM DTT, 10% SDS, 0.5% bromophenol blue, and 50% glycerol) then loaded into a 10% SDS-PAGE gel, along with BioRad Precision Plus Protein Standards (Cat.# 1610394). The gel was run at 150V for approximately 45 minutes, or until the loading dye front ran off the bottom of the gel. Using a blot transfer machine, the samples were transferred from the gel to a PVDF membrane, transferring at 2 volts per blot for 8 minutes. The membrane was rinsed in Tris buffered saline with 1% Tween 20 (TBS-T, pH 7.4), then blocked in 5% milk made in TBS-T. Primary solutions were made in 2% bovine serum albumin (BSA) in TBS-T and incubated overnight at 4 °C. The primary antibody dilution of B3GNT5 antibodies was 1:1000, and the dilution of β-tubulin (β-

tub) and GADPH antibodies was 1:3000. After incubation, the blots were washed in TBS-T three times for ten minutes, then added to the secondary antibody solution, made of 5% milk in TBS-T with a 1:5000 dilution of anti-rabbit antibody. Blots were incubated in this solution for 1-2 hours at room temperature on a shaker, then rinsed three times in TBS-T. Blots were then incubated for 1 minute in pico or dura chemiluminescent substrate and imaged using a BIORad ChemiDoc imaging system. Blot quantification was performed using ImageJ software.

SNAP i.d. 2.0 Immunodetection

After SDS-PAGE transfer to a membrane, protein immunodetection can be accelerated by using The SNAP i.d.® 2.0 Protein Detection System (Millipore Sigma) in lieu of overnight Western incubation. This protocol was adapted from Millipore Sigma's "30-minute Immunodetection Protocol Using the SNAP i.d.® 2.0 System." After protein transfer, the PVDF membrane was cut to the desired size, and placed protein side down in a dampened blot holder. The blot holder was gently rolled to remove bubbles and placed protein side up in the blot holding frame. The frame was placed in the base and 30 mL of 0.5% milk (in TBS-T) was added as blocking solution. The frame was pressed down, and vacuum applied. Once empty, primary antibody solution (1:1667 B3GNT5 or 1:5000 β-tub in 0.5% milk) was added to each blot and allowed to incubate for 10 minutes. Collection trays were placed under each blot, so that when the vacuum was applied, excess primary antibody solution was collected in the trays. The residual solution was re-applied to the blot, and the 10-minute incubation and aspiration was repeated twice more. The collection trays were removed, and the blot was washed 4 times with approximately 15 mL TBS-T with the vacuum continuously running. The vacuum was turned off, and 5 mL of secondary antibody solution (1:5000 anti-rabbit antibody in 0.5% milk) was

incubated on the blot for 10 minutes. The TBS-T wash was performed four more times. The blot was then removed and imaged as described in the previous section.

siRNA Transfection

The protocol for forward siRNA transfection was adapted from SigmaGen's "A General Guide for Transfecting Mammalian Cells" and Eupheria Biotech's "esiRNA Transfection Conditions for Various Cell Lines & Phenotypes." siRNA sequences are provided in Table 2. Cells were seeded in a six well plate the day prior to be 70-80% confluent during transfection, with the media changed 30-60 minutes prior to the experiment. For each well to be transfected, 1 µL B3GNT5 siRNA (Eupheria Biotech Cat # EHU151711-50UG) was diluted in 50 µL serum-free media, and 3.0 µL PolyJet was diluted in a separate 50 µL of serum-free media. The PolyJet solution was immediately mixed into the siRNA solution and allowed to incubate for 10 minutes, then the mixture was added drop-wise to the well and slowly swirled. Cells were incubated 72 hours before collection. An adaptation of this protocol using DharmaFect 1 or DharmaFect 3 used a transfection mixture of 10 µL siRNA in 190 µL serum-free media and 10 µL of DharmaFect (1 or 3) and 190 µL serum-free media, as adapted from manufacturer guidelines – Media in well was scaled down to result in the same total volume of 2 mL.

Reverse transfection of B3GNT5 siRNA (first Eupheria Biotech, then Ambion - P/N AM16704, ID# 112254) was performed following Invitrogen's "Reverse Transfection of Stealth™ RNAi or siRNA using Lipofectamine™ 2000 in a 96 well plate format" protocol scaled up to a 6 well plate. Eupheria Biotech siRNA was tested at a range of concentrations, with a 5:1 ratio of siRNA to Lipofectamine 2000. Ambion siRNA reverse transfection was performed with 5 µL Lipofectamine and 75pmol siRNA. To form the siRNA-Lipofectamine 2000 complexes, Lipofectamine 2000 was gently mixed into 250 µL Opti-MEM medium and

incubated for 5 minutes. The siRNA was gently mixed with 250 µL Opti-MEM in the well of a 6-well plate. After incubation, the Lipofectamine 2000 dilution was added directly to the siRNA dilution, and the mixture was incubated for 15 minutes to allow complexes to develop. 2 mL of complete medium containing 344,000 cells was added to each well containing siRNA, and the plate was incubated 48-72 hours before collection.

Antibiotic Cytotoxicity Selection

To determine the lowest concentration of antibiotic required for complete cell death, cells were seeded into a 24 well plate, allowed to attach, and tested in triplicate at a range of antibiotic concentrations. The plate was observed daily under microscope, and media with antibiotic was replaced every 2-3 days. After approximately a week, the lowest concentration observed to have 100% cell death in all wells was chosen as the concentration for antibiotic selection in plasmid selection and lentiviral infection.

B3GNT5 Plasmid Growth and Isolation

Two B3GNT5-expressing plasmids were isolated during this study: EXW01-M67 ("M67", selection agent hygromycin) and EXW01-M68 ("M68", selection agent puromycin). This protocol was adapted from the QIAGEN protocol "Plasmid DNA Purification Using QIAGEN Plasmid Maxi Kit" and performed using QIAGEN proprietary reagents. *Escherichia coli* (*E. coli*) previously transformed with one of the plasmids and kept in frozen glycerol stock was sampled with clean pipette tip and incubated overnight in Luria broth with ampicillin at 37 °C and 250 rpm. The culture was transferred to a large polypropylene centrifuge container and spun at 4000 x g for 15 minutes at 4 °C. The container was inverted to drain supernatant, and the pellet was thoroughly resuspended in 10 mL of Buffer P1 and transferred to a smaller

polypropylene centrifuge tube. Ten mL of Buffer P2 was added, and the tube was gently mixed by inversion, causing a color change due to the activation of LyseBlue in Buffer P1. Ten mL of prechilled Buffer P3 was added, mixed gently, and the sample was left on ice, resulting in the formation of a fluffy-looking white precipitate. The tube then underwent centrifugation in a floor centrifuge equipped with Sorvall SS-34 rotor for 30 minutes at 13,000 rpm and 4 °C. The supernatant was transferred to a new tube and centrifuged at the same speed for 15 more minutes. DNA was collected from the supernatant via a Buffer QBC equilibrated QIAGEN-tip 500 column, washed twice with 30 mL Buffer QC, and eluted with 15 mL of Buffer QF. Isopropanol was added to the eluate to cause DNA precipitation, and the tube was centrifuged at 11,000 rpm in the floor centrifuge for 30 minutes at 4 °C. The supernatant was discarded, and the resulting DNA pellet was washed with 5 mL of 70% ethanol, centrifuged at 11,000 rpm for 10 minutes, and then allowed to airdry overnight. Once dried, the pellet was resuspended in 50-100 µL of PCR-grade water, and the DNA concentration was determined via Nanodrop.

Plasmid Transfection

This protocol was adapted from SignaGen's "PolyJet In Vitro DNA Transfection Reagent" protocol scaled to a six well plate. Approximately 30-60 minutes before transfection, the media on 70-80% confluent cells split the day prior was changed. One µg of plasmid DNA was diluted and gently mixed in 50 µL of serum-free media, and 3 µL of PolyJet was diluted in a separate 50 µL of serum-free media (following the suggested 3:1 DNA to PolyJet recommendation). The PolyJet dilution was immediately transferred into the DNA dilution and thoroughly mixed. The mixture was incubated for 10-15 minutes at room temperature before being added drop-wise into the plate and gently swirled. The transfection media was replaced

with standard media 6-18 hours later to prevent PolyJet-induced cytotoxicity. Cells were collected 48-72 hours later.

Plasmid transfection is typically transient, but stable transfection may be established by isolating and growing up the few cells that have had the plasmid integrated into their genome. To do so, transfected cells were grown and split for two passages, then treated with the antibiotic selection agent that the plasmid confers resistance to. Treatment with antibiotic is continued for several days, until a control, non-transfected plate of cells indicates complete cell death and defined antibiotic resistant colonies can be identified on the transfected plate. These colonies are grown out to become a stably expressing plasmid line.

Lentiviral Transduction of CRISPR/Cas9

To establish a B3GNT5 knockout cell line, cells were infected with lentivirus containing a CRISPR/Cas9 plasmid targeting the gene. The day before infection, 3 million cells were seeded in a 10 cm dish so they would be approximately 70-80% confluent. Media was aspirated from the dish, and new media containing hexadimethrine bromide (polybrene) was added at a final concentration of 8ug/mL. Using a multiplicity of infection of 1, it was calculated that 23 µL of the virus would be needed per dish. 23 µL of the virus was added to the dish, swirled gently to mix, and incubated. Media was changed 4-72 hours post infection. The lentiviral plasmid encodes genes for puromycin resistance and green fluorescent protein (GFP), so 72 hours post transfection, puromycin was added to the media. Once an uninfected plate treated with puromycin displayed complete cell death, the surviving infected cells were grown to confluence, where they were examined for fluorescence by microscopy.

Note: Lentiviral work requires BSL-2 handling, so anything that came in contact with the virus or treated culture was thoroughly sterilized. Solid waste was disposed of in infectious waste bags, and liquid waste was bleached and disposed of. Infected plates were stored in secondary containers in the incubators to prevent cross-contamination.

Monoclonal Sorting and Clonal Selection

Once multiple confluent plates of puromycin-resistant CRISPR-edited cells were established, the cells were taken to the VCU Flow Cytometry Shared Resource (FCSR), where single cells with high GFP fluorescence were sorted into three 96 well plates. One row received 50 cells/well to establish a backup polyclonal edited line for cryopreservation. Each monoclonal line was grown out to a 48, 24, and 12 well plate, before being split into two 6 well plates, one of which was used for Western blotting to analyze B3GNT5 expression.

Mass Spectrometry – Cell Culture

Control HeLa cells and edited HeLa B3GNT5^{PKO} cells were grown in triplicate and collected as described in "Lysate Collection," then stored at -80 °C until ready for preparation. Remaining sample was used to calculate protein concentration by Bradford assay. Samples and MS internal standard were warmed to room temperature, and 250 pmol of internal standard (Avanti Polar Lipids) and 500 µL of chloroform were added to each tube, resulting in a methanol:chloroform:water ratio of 2:1:0.1. The internal standard was composed of 17-carbon chain-length analogs for sphingoid bases and sphingoid base 1-phosphates, and C12-fatty acid analogs for N-acyl sphingolipids (39). Samples were tightly capped and incubated overnight at a 48 °C water bath. The next day, samples were spun at 4,100 x g for 15 minutes at 4 °C. Each sample was decanted into a new glass test tube, which was run on a Savant Speed Vac SPD 2030

Integrated Vacuum Concentrator at 45 °C and 8 mTorr pressure for 5 hours, or until all samples were dry. Each sample was resuspended in 500 µL of LC/MS grade methanol by extensive vortexing and water bath sonication. Once completely resuspended, the samples were spun at 3,800 x g for 10 minutes, then decanted into autoloader vials without disturbing the pellet. Autoloader vials were capped and stored at -80 °C until MS, which was performed at the VCU Lipidomics Core. Data from the Lipidomics Core was manually integrated using the software AB Sciex Analyst 1.6.2. Retention times were compared to the internal standard, and the area under the peak was integrated and normalized to initial sample concentration to determine the pmol of lipid species per mg of sample protein.

Statistical Analysis

All data analysis was performed using GraphPad PRISM versions 8 & 9. Multivariate analysis was done by two-way ANOVA and Sidak's or Dunnett's multiple comparisons test. Sidak's multiple comparisons test was used for pairwise comparisons between two groups (in this case, different cell lines), while Dunnett's test was used when comparing multiple groups against a control (in this case, different drug concentrations) (40). Error bars indicate standard error of the mean (SEM). Lines of best fit were generated using a nonlinear regression fitting inhibitor vs response with variable slope. Least squares was used as the primary method of regression, but robust regression was used when data sets demonstrated heteroskedasticity, which violates the assumption of homoscedasticity necessary for least squares (41). Outliers were calculated with GraphPad's ROUT ("**Ro**bust regression and **Out**lier removal") method, with Q=1% (41). Univariate analysis was performed using the Holm-Sidak unpaired t-test. Kaplan-Meier plots were obtained from The Human Protein Atlas, which calculated mean 5-year survival of high and low gene expression and a log-rank p-value. Alteration plots were generated

using cBioPortal, which provided percent of samples altered for each of the input genes. The significance level was $\alpha = 5\%$. Unless otherwise stated, all experiments were performed in a single trial with three replicates.

Results

Transwell Invasion Assay Optimization

Optimization of Matrigel dilution, volume, cell count

To assess optimal conditions for studying cancer cell invasion, I assessed a variety of Matrigel dilutions and volumes to establish conditions that reduced, but did not fully inhibit, cellular migration. Volumes of 70 and 100 µL of Matrigel solution were tested against cell seeding densities of 50,000, 75,000, and 100,000 cells per insert. As expected, higher cell concentrations corresponded to higher levels of transwell migration [Figure 3A]. I selected a concentration of 100,000 cells per well to ensure a higher level of cellular confluency on the membrane, which would be a more accurate representation of *in vivo* conditions. I found that 70 µL of Matrigel was an adequate amount for full-membrane coverage, while volumes of 100 µL and above resulted in levels of migration more difficult to quantify, likely due to the resulting thickness of the synthetic extracellular matrix. At all tested volumes, meniscus formation was observed when the Matrigel was added to the transwell insert. This could not be resolved by manual Matrigel redistribution using a sterile pipette tip or by allowing the Matrigel to solidify while on a slowly gyrating platform, and may contribute to uneven Matrigel thickness on the membrane.

Optimization of assay incubation time

Dilutions of 1:1, 1:2, and 1:4 of growth-factor-reduced Matrigel in serum-free culture medium were tested to identify the preferred Matrigel concentration. A 1:1 Matrigel dilution resulted in low levels of migration regardless of incubation time, while 1:2 and 1:4 dilutions enabled more cellular migration and showed time dependent increases in migration [Figure 3B & C]. Invasion assays were run for 24, 48, or 72 hours to determine ideal incubation time. Predictably, transwell invasion increased at each time increment, though the level of invasion was cell line dependent - H460 cells appeared to have more invasion than HEK293FT at each observed time [Figure 4]. A 48-hour incubation was chosen given the complete membrane saturation displayed by HeLa cells at 72 hours, while other cell lines, such as H460s and HN12s, had low levels of invasion at 24 hours that were difficult to visualize or effectively quantify via crystal violet elution [Figure 3B, Figure 4].

Evaluation of FBS pre-starvation

Published transwell assay protocols conflict as to whether cells should undergo a 24 hour FBS prestarvation before seeding into the assay to promote cell reactivity to the FBS chemogradient (42-44). This was assessed in both H460 and HEK293FT cells by replacing the cell media with a complete, serum-free medium the day prior to assay setup. Compared to cells that were not prestarved, both prestarved H460 and HEK293FT cells exhibited visible decrease in transmembrane migration [Figure 4].

Invasion of nontransformed cell lines

Given that Matrigel on the Transwell membrane is intended to simulate a basement membrane, it was expected that nontransformed cells would not exhibit transmembrane invasion.

However, when comparing the nontransformed, immortalized SALEs against their KRAS overexpressing, transformed version SALEKs, SALEs were displayed visibly higher invasion than SALEKs [Figure 5].

In summary, optimizations of transwell invasion assay resulted in a protocol using 70 µL of Matrigel diluted 1:2 in serum-free medium for basal membrane simulation, and 100,000 cancer cells seeded per well and incubated for 48 hours. It was determined that FBS prestarvation does not result in increased transmembrane movement, and primary cell media, such as SABM (media for SALE cells) is growth serum free, and therefore FBS is not an appropriate chemoattractant.

Comparing cell viability of lung adenocarcinoma and squamous carcinoma in response to eliglustat, PPMP, and CBE

Before 2014, the Guidelines on the Management of Lung Cancer did not recommend that the drug therapy treatment of non-small cell lung cancers (NSCLCs) be tailored to histological type (45). However, several clinical trials have indicated that squamous and non-squamous NSCLCs have varying driver mutations which may impact resistance to chemotherapeutic drugs (45). To test for tumor type dependent responses to UGCG-inhibiting drugs, CCK-8 assays were performed on SK-MES-1, a squamous lung carcinoma cell line, and SK-LU1, a lung adenocarcinoma cell line, treating both lines with eliglustat, PPMP, or CBE to observe if the two tumor types may have differing responses to Cer/GlcCer pathway inhibitors. A CCK-8 assay quantifies cell viability through the addition of substrate WST-8 to each well, where reduction of the substrate within living cells results in the production of formazan, leading to a color change that can be detected via plate reader. There was no significant difference between SK-MES-1 and SK-LU1 at any concentration of CBE or eliglustat tested [Figure 6A&C]. However, there

was a significant interaction between cell type and PPMP concentration ($p < 0.0001$), as SKLU-1 displayed a significantly higher viability than SK-MES-1 in response to PPMP. SKLU-1 had an inhibitory concentration (IC)50 of 13.22 µM, while the IC50 of SK-MES-1 was 5.77 µM [Figure 6B].

Comparing cell viability and invasion of colon adenocarcinoma and carcinoma in response to eliglustat, PPMP, and CBE

CCK-8 assays were performed to investigate if HCT116, colon carcinoma, and HT29, a colon adenocarcinoma, would exhibit similar responses to eliglustat, PPMP, or CBE. There was no significant difference between HCT116 and HT29 at any concentration of eliglustat, PPMP, or CBE [Figure 7].

Transwell invasion assays were performed on two colorectal cancer lines treated with eliglustat, PPMP, or CBE to observe if the Cer/GlcCer pathway may play a role in basal membrane invasion. HCT116 cells showed no significant difference in migration between the vehicle controls and cells treated with eliglustat (2.5 µM), PPMP (6 µM), or CBE (50 µM) [Figure 8A & B]. However, in HT29 cells, while there was no significant difference between CBE, eliglustat (2.5 µM), and their respective vehicle controls, there was a significant migration increase of over 300% for cells treated with PPMP ($p = 0.021$) [Figure 8C & D]. There was a similarly high increase of 284% in migration of cells treated with 5 µM eliglustat ($p = 0.036$) [Figure 8D].

Comparing cell viability of colon adenocarcinoma and carcinoma in response to eliglustat, PPMP, and CBE in conjunction with cisplatin and vinorelbine

This study used two chemotherapeutic drugs: cisplatin and vinorelbine. Cisplatin is a platinum compound that impedes cell replication by crosslinking to DNA (46). The drug is a common treatment in several kinds of cancer, including colon cancer, but effective treatment is often hampered by cisplatin-resistant cells (47). UGCG overexpression has been associated with multidrug resistance, and the knockdown of UGCG expression was demonstrated to sensitize colon cancer to cisplatin (48). It has been found in lung adenocarcinoma that high GlcCer expression also leads to resistance to vinorelbine, which acts by the inhibition of microtubule formation (49, 50). Vinorelbine is currently not prescribed for colon cancer treatment due to low levels of tumor sensitivity to the drug; however, it has been discovered that cancer cells containing a mutation in BRAF (*ACS(V600E)*) or having a similar gene expression pattern ("BRAF-like") exhibit significantly more sensitivity to vinorelbine than non-BRAF-like cells (51). Given that HT29 contains the *BRAF(V600E)* mutation and HCT116 is BRAF-like, I used both cell lines in my study.

Viability of HT29 and HCT116 cells was assessed via CCK-8 assay after drug cotreatment with the two chemotherapeutic drugs, cisplatin or vinorelbine, in combination with eliglustat, PPMP, or CBE. In both cell lines, increasing concentrations of eliglustat and CBE had no observable effect on observed cellular viability in combination with either cisplatin or vinorelbine (Note: cisplatin + eliglustat was not tested in HT29) [Figure 9A-D; 10 A-C]. PPMP and cisplatin also had no significant differences in either cell line [Figure 9E, 10D]. However, in HT29 treated with PPMP and vinorelbine, cells in higher PPMP presented reduced viability at all concentrations of vinorelbine, and the interaction between the two drugs was statistically

significant (p = 0.0022) [Figure 10E]. This trend was not observed in HCT116 co-treated with PPMP and vinorelbine [Figure 9F].

Gene Expression Survival Analysis

UGCG

Using the Human Protein Atlas, levels of mRNA expression of the UGCG gene were compared to patient survival via Kaplan-Meier plot. Patient samples were grouped into either low or high expression of the gene, with the expression cut off between groups determined by the Human Protein Atlas to be the gene expression level that yields maximum difference between the two groups. In colorectal cancer (n = 597), low expression of UGCG trended toward a slightly higher five-year survival rate (62%) than high expression (60%) (p = 0.054); in colon adenocarcinoma (COAD) specifically (n = 438), low expression of UGCG also trended towards higher survival (p = 0.062), and had a ten percent higher five-year survival rate (67%) than patients with high UGCG [Figure 11A & B]. In lung cancer, there was no significant difference in survival probability (p = 0.20), with five-year survival rates of 42% and 48% in the low and high expression groups, respectively. In lung adenocarcinoma (LUAD) (n = 500), patients with high levels of UGCG trended towards higher survival with a 43% five-year survival rate, while patients with low UGCG had a 34% survival rate (p = 0.30). In lung squamous cell carcinoma (LUSC) the opposite trend was observed (n = 494), as high UGCG had a survival rate of 42% while low UGCG had a survival of 52% (p = 0.076) [Figure 11C & D]. In conclusion, there was no significant difference in survival between low and high UGCG expression in any of the examined cancers, though in all cancers but lung adenocarcinoma, lower UGCG expression trended towards higher survival.

GBA

Expression levels of GBA in colorectal cancer (n = 569) using TCGA trended towards higher GBA expression having higher survival rates (p = 0.34): five-year survival of patients with high GBA expression was 69%, while low expression was 58%; in colon adenocarcinoma, high GBA had a survival rate of 70%, while low GBA had a survival of 60% (p = 0.30) [Figure 12A & B]. In lung cancer, low expression of GBA results in significantly higher survival (p = 0.048). In LUSC, there was a significant correlation between low mRNA expression and patient survival, with survival with high GBA at 44% and survival with low GBA at 53% (p = 0.038); however, this trend was nonsignificant in LUAD, though five-year survival with high GBA was 36% and survival with low GBA was 46% (p = 0.27). [Figure 12C-E]. In conclusion, there was no significant difference in survival between low and high GBA expression in colon cancer or lung adenocarcinoma, but low expression of GBA is correlated to significantly higher patient survival.

B3GNT5

The five-year survival rate of cervical cancer patients (n = 291) trends towards higher survival with high B3GNT5 expression (p = 0.057), which has a five-year survival of 80%, while the survival rate with low B3GNT5 expression is 62%. The opposite trend is observed in head and neck cancer patients (n = 499) where low B3GNT5 expression results in significantly higher survival (p = 0.031). In head and neck cancers, five-year survival with high B3GNT5 expression is at 34%, and survival with low expression is at 50% [Figure 13]. In conclusion, there was no significant difference in survival between low and high B3GNT5 expression in cervical cancer, but low expression of B3GNT5 in head and neck cancers is correlated with significantly higher survival.

Analysis of Gene Alteration Frequency for Sphingolipid Biosynthesis Genes

GBA and UGCG

Using cBioPortal to access The Cancer Genome Atlas' PanCan database, the occurrence of alteration of the 90 genes involved in sphingolipid biosynthesis were calculated, with focus placed on GBA and UGCG. In COAD, GBA expression was altered in 1.3% of cases, while UGCG was altered in 1.1% of cases. In LUAD, GBA was altered in 10% of cases, making it the second most frequently altered of the sphingolipid biosynthesis genes, while UGCG was altered in 0.6% of cases. CERS2 was the most frequently altered gene. In LUSC, GBA was altered in 5% of cases, while UGCG was the least altered gene at 0.2% [Figure 14].

B3GNT5

The occurrence of alteration of the 90 genes involved in sphingolipid biosynthesis were also calculated with focus placed on B3GNT5. In both head & neck and cervical cancers, B3GNT5 was the most frequently altered gene of the sphingolipid biosynthesis genes, at 15% and 14% respectively [Figure 15].

siRNA knockdown of B3GNT5 expression

To identify a method by which to temporarily silence B3GNT5 in cells, which would enable examination of how the protein affects cellular behaviors such as invasion and drug resistance, I tested multiple siRNA protocols. The protocols were tested on HEK293FT cells due to their high transfection efficiency (52). B3GNT5 siRNA (Sigma, cat. # EHU151711) transfected using PolyJet (SigmaGen cat. #SL100688) yielded no visible differences in B3GNT5 abundance via Western blotting [Figure 16A]. DharmaFect 1 and DharmaFect 3 were also used to transfect the siRNA, both of which displayed no visible differences to the control [Figure

16B]. Reverse transfection of both HEK293FT and HeLa cells was performed using Lipofectamine 2000 at a variety of concentrations. In HEK293FT cells, no visible difference in B3GNT5 abundance was observed; however, at 20 and 40 µL of siRNA in HeLa cells, B3GNT5 expression appeared much fainter than the control [Figure 16C]. When repeated in triplicate with 20 µL of siRNA, there was no observable difference between the control and transfected samples [Figure 16D]. The siRNA obtained from Sigma was long, at 413 bp, so new siRNA was purchased from Ambion (AM16704 ID# 112254) at 21 bp. Reverse transfection with the Ambion siRNA using Lipofectamine 2000 in HEK293FT, HeLa, H460, and HN12 cells was performed and incubated for 48 and 72 hours. There were no noticeable decreases in B3GNT5 expression at either time in any cell line; however, incorrect cutting of the β-tubulin (β-tub) housekeeping gene Western blot makes these results inconclusive [Figure 16E]. In conclusion, no siRNA silencing of B3GNT5 was successfully utilized during this study.

Transient and stable Transfection of HeLa with B3GNT5 plasmid

HeLa cells were transfected with B3GNT5 plasmid and then underwent antibiotic selection in an attempt to create a stable B3GNT5 overexpressing line. Transfection with both M67 and M68 plasmid resulted in significant B3GNT5 overexpression, with M68 having nearly twice as high of expression as M67 [Figure 17A & B]. The M68 plasmid was selected for future experiments. To create a stably expressing HeLa line, the transfected cells were treated with 2 µg/mL puromycin until the control plate showed complete cell death, yet the antibiotic-resistant line that resulted had a similar B3GNT5 expression to the control line after several passages [Figure 17A]. The stable transfection line was therefore abandoned.

Transfection of HN12 with B3GNT5 plasmid

The head and neck tumor line HN12 was transfected with the B3GNT5 M68 plasmid, but Western blotting indicated very faint expression of B3GNT5 in the control that did not increase after transfection [Figure 17A]. Attempts to establish a stable transfection line were made with both the M67 and M68 plasmids. In both attempts, antibiotic selection resulted in major cell death (estimated less than 1% confluence after treatment), and surviving cells were unable to re-establish normal growth and confluency. Therefore, neither a transient nor stable transfection of HN12 with B2GNT5 plasmid could be established.

B3GNT5 antibody comparisons

Given the failure of siRNA knockdown and HN12 transfection, a second B3GNT5 antibody was acquired for Western blotting and the two were compared. Both antibodies were also tested using SNAP i.d. 2.0 blotting, an accelerated Western blotting method, as some antibodies are too sensitive to use the technique. It was found that both antibodies bind to B3GNT5 with similar levels of specificity in both techniques; however, it appears that the original Invitrogen antibody (Ref. # PAS-26653) has stronger affinity to endogenous B3GNT5 expression, while the Proteintech antibody (Cat. # 20422-1-AP) has stronger affinity for transfected B3GNT5 [Figure 18].

Screening for CRISPR-induced B3GNT5 knockdown

To identify and establish a B3GNT5 knockout HeLa cell line, monoclonal populations generated after CRISPR transfection were screened by Western blotting using both traditional Bradford normalization and TCA precipitation. Of the 39 clones screened, no clones exhibited complete knockout of B3GNT5 [Figure 19A & B]. The clone which will be referred to as

"B3GNT5^{PKO}" was selected for future experiments due to its consistently reduced B3GNT5 expression ($p = 0.0518$) [Figures 19C & D, 20]. Three alternative B3GNT5 knockdown clones and four polyclonal stocks were also selected as backups and cryopreserved [Figure 19A].

Invasion of B3GNT5-knockdown HeLa

To observe if levels of B3GNT5 expression could correlate to invasive behavior, HeLa and HeLa B3GNT5^{PKO} cells were compared in a Transwell invasion assay. It was hypothesized that the B3GNT5 knockdown samples would have fewer invading cells than the control samples, as other research has demonstrated B3GNT5 upregulation leads to increased transwell invasion in non-small cell lung cancer lines (53). However, the control and B3GNT5 knockdown lines had no significant difference in invasion ($p = 0.86$) [Figure 21].

HeLa B3GNT5-knockdown and Chemotherapeutic resistance

To observe if the knockdown of B3GNT5 could affect response to chemotherapeutics, HeLa and HeLa B3GNT5^{PKO} cells were exposed to varying concentrations of cisplatin, vinorelbine, and doxorubicin and quantified by CCK-8 assay. With doxorubicin, there was no statistically significant difference at any given concentration [Figure 22B]. With vinorelbine, B3GNT5^{PKO} displayed significantly higher viability at low concentrations ($p < 0.0001$ at 0.03 and 0.06 μM vinorelbine, respectively), with a statistically significant interaction between cell type and drug concentration ($p < 0.0001$) [Figure 22A]. The response to cisplatin also demonstrated that B3GNT5^{PKO} had higher levels of cellular viability than the HeLa control cells at most tested concentrations of cisplatin, and the interaction between the drug and cell type was significant ($p = 0.011$) [Figure 22C].

Given the previous discovery made that vinorelbine can work in conjunction with PPMP to reduce cell viability in some cell lines, I wanted to see if this combination may be effective in HeLa cells, and if this combination may be further effective when combined with B3GNT5 downregulation. Both HeLa and B3GNT5^{PKO} cells were co-treated with vinorelbine and PPMP at varying concentrations and quantified by CCK-8 assay. The HeLa cells with no PPMP had significantly higher viability than samples with both 5 and 10 μM PPMP at low concentrations (0.03 and 0.06 μM) of Vinorelbine ($p \leq 0.0073$). The IC50 of 0 μM PPMP was approximately 0.058, while 5 μM and 10 μM of PPMP had an IC50 of 0.042 μM and 0.039 μM, respectively. However, the triplicates of 0.03 μM Vinorelbine and no PPMP were unexpectedly high, likely due to experimental error, which may skew the data [Figure 23A]. HeLa B3GNT5^{PKO} cells exhibited a similar pattern in response to co-treatment with PPMP and vinorelbine, with higher concentrations of PPMP trending toward lower survival and IC50, though there was not a significant difference at any given concentration of PPMP [Figure 23B]. Comparing the HeLa and HeLa B3GNT5^{PKO} lines at each concentration of PPMP indicated at 0 μM and 10 μM of PPMP that cell line had a significant interaction with vinorelbine concentration ($p < 0.0001$ and $p = 0.0052$, respectively). HeLa B3GNT5^{PKO} has significantly higher survival than the HeLa control with no PPMP ($p < 0.0001$; HeLa IC50 = 0.058 μM, B3GNT5^{PKO} IC50 = 0.091 μM), as well as significantly higher survival at 10 μM PPMP ($p = 0.0015$; HeLa IC50 = 0.039 μM, B3GNT5^{PKO} IC50 = 0.061 μM) [Figure 23C & E]. The trend of increased cellular viability of HeLa B3GNT5^{PKO} can also be seen at 5 μM PPMP, but none of the observed differences between cell lines are statistically significant ($p = 0.490$; HeLa IC50 = 0.042 μM, B3GNT5^{PKO} IC50 = 0.065 μM) [Figure 23D]. In conclusion, B3GNT5^{PKO} demonstrated higher survival than the HeLa control line in response to vinorelbine, with or without PPMP co-treatment, but there

were no significant variations between B3GNT5^{PKO} and the HeLa control in response to cisplatin and doxorubicin.

Mass Spectrometry of HeLa B3GNT5^{PKO}

Triplicate samples of HeLa and HeLa B3GNT5^{PKO} underwent mass spectrometry at the VCU Lipidomics core and were integrated using Analyst 6.1.2 software [Sample B3GNT5 quantification in Figure 19C & D]. Lipidomics data were normalized to internal standards and sample protein concentrations. Cer, monohexosylceramide (MonoHex), sphingomyelin (SM), and LacCer were measured at the acyl chain lengths C14:0, C16:0, C18:1, C18:0, C20:0, C22:0, C24:1, C24:0, C26:1, and C26:0, and sphingosine (So), dihydrosphingosine (DHSo), sphingosine-1-phoshate (S1P), and dihydrosphingosine-1-phosphate (DHS1P) were measured at C18:0 or C18:1. MonoHex is comprised of both glucosyl- and galactosylceramide.

HeLa B3GNT5^{PKO} displayed significantly higher 24:1 ceramide, C16, C24:1, and C24:0 MonoHex, C24:1 SM, and C24:1 and C24:0 LacCer than the HeLa control samples ($p < 0.0001$ for all except C16 MonoHex, where $p = 0.0066$, and C24:1 SM, where $p = 0.029$). All other chain lengths had no significant difference [Figure 24]. The total mean ceramide levels in the HeLa B3GNT5^{PKO} trended towards a nonsignificant increase compared to the control, while the total mean MonoHex was more than 2.5 times higher than the control sample ($p = 0.0085$), and the total mean LacCer was more than 3 times higher than the control ($p = 0.041$) [Table 3] [Figure 25]. In conclusion, decreased expression of B3GNT5 resulting in increased levels of 24:1 ceramide, C16, C24:1, and C24:0 MonoHex, C24:1 SM, and C24:1 and C24:0 LacCer compared to the control, and increased the total levels of MonoHex and LacCer.

Discussion

Given the growing understanding of the role sphingolipids play in the cellular regulation and behavior, it has become increasingly important to identify how aberrance of sphingolipid pathways contribute to cancer phenotypes and poor prognosis. In this study, I have focused on the Cer to Lc3Cer pathway, and more specifically on the enzymes UGCG and GBA, which regulate Cer to GlcCer conversion, and B3GNT5, which converts LacCer to Lc3Cer. High levels of Cer have been demonstrated to have pro-apoptotic effects, while high GlcCer and Lc3Cer expression have each been associated with cancer phenotypes or drug resistance (20, 34, 54). I hypothesized that inhibition of UGCG would increase sensitivity of cancer cells to chemotherapeutics, while inhibition of GBA may promote chemotherapeutic resistance and increased basal membrane invasion. Likewise, I hypothesized that the decreased expression of B3GNT5 in cancer cells could result in increased basal membrane invasion and drug resistance. CBE was used to inhibit GBA in both lung and colon cancer cell lines. In no instance, whether by itself or in combination with cisplatin or vinorelbine, did the drug impact cell viability or drug sensitivity, as measured by CCK-8, or transmembrane invasion, as observed by Transwell invasion assay. These results suggest that GBA inhibition alone does not promote resistance to cisplatin or vinorelbine, nor does it result in increased cellular invasion.

Unlike GBA inhibition, UGCG inhibition did result in changed cellular behaviors in this study. SKLU-1, a lung adenocarcinoma, showed a significant decrease in viability as compared to SK-MES-1, a lung squamous carcinoma, when treated with high concentrations of PPMP (25.6 & 51.2 μM). Though there was no difference in drug response between cell lines for the two colon cancers, treatment with PPMP and a higher concentration of eliglustat both resulted in a significantly increased level of cellular invasion only in HT29, the colon adenocarcinoma.

HCT116 had no significant increase in invasion due to treatment with PPMP, but invasion at the higher level of eliglustat is inconclusive. Treating both HT29 and HCT116 with PPMP or eliglustat in conjunction with either cisplatin in or vinorelbine yielded a similar pattern: HCT116 showed no significant change in viability with any tested drug combination (though the cisplatin/eliglustat combination was not performed), while HT29 showed significantly less cellular viability when co-treated with vinorelbine and PPMP. Interestingly, a similar trend in HT29 viability was not observed with vinorelbine and eliglustat. In both tissue types observed, only the adenocarcinoma seemed to be sensitive to treatment, suggesting there may be carcinoma type-dependent differences in UGCG response. Invasion increases in response to both PPMP and eliglustat suggest that UGCG inhibition may, surprisingly, promote cell invasion or division. However, that cell viability was only impacted by PPMP and not eliglustat in both cell lines suggests that this response may be either in-part or fully due to off-target effects, as PPMP also inhibits 1-*O*-acylceramide synthase (ACS), while eliglustat does not (29, 55). PPMP's co-inhibition of ACS, which synthesizes ceramide, results in more highly increased levels of cellular ceramide, and thus may make the cell more prone to apoptosis than eliglustat, which is not associated with cellular ceramide increases (29).

When examining Kaplan-Meier survival plots of lung and colon cancers, there is no statistically significant correlation between UGCG expression levels and survival; however, in all cases, lower UGCG expression trends toward higher rates of survival than higher UGCG expression. In colorectal cancer and LUAD, the opposite trend can be observed regarding GBA expression, though it is not statistically significant. In LSCC, however, low GBA expression is significantly correlated to higher survival than high expression of the gene, further suggesting

that there are variations between carcinoma types which lead to variable expressions of fundamental sphingolipids and their synthases.

Unlike both UGCG and GBA, B3GNT5 expression is a known marker of poor prognosis for multiple cancers – renal, pancreatic, and liver (19). In head and neck tumors, low B3GNT5 expression is significantly correlated with high survival. In cervical cancer, however, higher B3GNT5 expression trends towards higher survival. To investigate the effects of B3GNT5 expression on cancer behaviors, molecular techniques – siRNA, plasmid transfection, or CRISPR-Cas9 editing – were undertaken, as there is no known specific inhibitor of B3GNT5. Gene silencing via siRNA was ultimately unsuccessful in this study; however, this was worked around by establishing a CRISPR-edited B3GNT5 partial knockout line in HeLa cells. Difficulty obtaining a complete knockout may be attributed to a few factors, the first being that HeLa has severe aneuploidy, containing four copies of the region of chromosome 3 where the *B3GNT5* gene is located (56). A previous study had difficulty establishing homozygous B3GNT5 knockout in mouse models, where breeding mice heterozygous for *B3GNT5* knockout did not produce any mice with a homozygous knockout, implicating that the absence of B3GNT5 in embryonic development leads to pre-implantation lethality (57). *B3GNT5* transcripts could be identified in a mouse embryo at the two-cell stage and were present throughout embryonic development (57). In a later study which did successfully knock out B3GNT5 in mice, mice that survived delivery appeared normal in early life, but developed a number of abnormalities later on, such as growth retardation, splenomegaly, fur loss, obesity, reproductive effects, and premature death (58). While it is possible that further monoclonal screenings may identify a complete knockout, the high copy number in HeLa cells and possibility that B3GNT5 is required for normal cellular proliferation make it unlikely.

Experimentation on the resulting partial knockout line, HeLa B3GNT5^{PKO}, indicated that reduced B3GNT5 does not impact transmembrane invasion, nor does it seem to impact chemotherapeutic sensitivity with the drugs tested. When treated with vinorelbine in conjunction with PPMP, however, the HeLa B3GNT5^{PKO} line appears to be less sensitive to PPMP or more resistant to vinorelbine than the HeLa control line, as the knockdown line exhibits significantly higher viability at all survivable concentrations of vinorelbine. This may suggest the lacto- and neo-lacto-series of sphingolipid pathways contribute to chemotherapeutic sensitivity, as reducing levels of their precursor enzyme increases cellular viability.

It was expected that MS analysis of HeLa B3GNT5^{PKO} would only indicate increases in LacCer, given that B3GNT5 metabolizes LacCer. However, it was found that C24:1 was significantly elevated in every sphingolipid species studied, and C16 and C24 MonoHex and C24 LacCer also presented significant increases. MonoHex encapsulates both glucosyl- and galactosylceramide, but it can be presumed that this increase in MonoHex is due largely to GlcCer, as galactosylceramide is primarily expressed in the central and peripheral nervous system, kidney, and gastrointestinal tract (59). Thus, it seems that reduced B3GNT5 increases not only total levels of LacCer, but also GlcCer, its precursor. This may indicate that reduced B3GNT5 causes increased expression of the β-galactosidase KLB1, which convert LacCer back to GlcCer (16). Increased GlcCer could also indicate increased expression of UGCG. It is also possible that increased levels of GlcCer is not caused by increases in the expression of KLB1 directly, but rather due to the increased amount of its substrate, LacCer, that results in higher amounts of LacCer to GlcCer conversion. In lung adenocarcinoma, it was found that the high expression of GlcCer was associated with vinorelbine resistance, and vinorelbine-resistant cells had aberrantly high expression of Bcl-xL, an anti-apoptotic protein that can confer multidrug

resistance phenotypes in some cancers (49). Co-treatment of vinorelbine-resistant cells with vinorelbine and PDMP, an analog of PPMP, resulted in an increase in cell apoptosis and a decrease in Bcl-xL expression (49, 60) .Therefore, the increased levels of GlcCer in the HeLa B3GNT5^{PKO} line may explain why the line exhibited higher cell viability in response to vinorelbine than the control HeLa line. Both lines saw a reduction in viability when combined with PPMP, supporting the idea that PPMP decreases GlcCer-induced chemotherapeutic resistance. Further investigations into the associations between PPMP and vinorelbine may identify PPMP as a drug worth developing pharmaceutically for co-administration with vinorelbine to reduce drug resistance during chemotherapy.

Chapter 2: Sphingolipidomic analysis of tumor and normal head and neck tissues

Significance

Head and neck cancers (HN) are the sixth most common form of cancer worldwide, and are a complex set of cancers which originate in the upper respiratory and digestive tracts (oral cavity, pharynx, larynx, sinuses, salivary glands, or thyroid) (61). Major risk factors for this cancer are smoking, alcohol use, and human papillomavirus infection, the latter of which is contributing to an increasing percentage of total cases in recent years (62). Squamous cell carcinoma (HNSSC) makes up approximately 85% of diagnosed HN, with approximately 42,000 diagnoses and 12,000 deaths in the US every year (63). Studies have indicated that racial and ethnic health disparities prevalent in the US contribute to worse prognosis for African Americans diagnosed with HN – a demographic analysis of more than 20,000 patients in Florida diagnosed with HN found that African Americans were more likely to be diagnosed at a younger age, present more advanced disease, and demonstrate a significantly poorer prognosis than their Caucasian counterparts (64). In HN, like many other cancers, altered sphingolipid levels have been observed: Decreases in ceramide have been reported, as have increases in sphingosine-1-phosphate (S1P) (65). Analysis of acyl-chain length of these sphingolipid species in HN has previously indicated that C16 Cer contributes to tumor proliferation, while C18 Cer inhibits tumor growth (66). To identify variations in sphingolipid abundance between normal and tumor tissues as well as identify possible race-dependent variations in chain-length abundance, this study will perform mass spectrometry on paired tumor and normal tissues collected from African American and Caucasian patients with HN.

Methods

Mass Spectrometry – Human Tissue

This protocol was performed as published in (39, 67), and is summarized below. Human tissue samples were received frozen at -80 °C in Optimal Cutting Temperature (OCT) compound. Because OCT interferes with accurate MS readings, it must be removed from the tissue. In preparation, 1.5 mL polypropylene tubes and 13x100mm screw-cap tubes were prelabeled with tissue identifier codes, and each polypropylene tube was weighed. Two mL of LC/MS grade methanol was added to each screw-cap tube and pre-chilled to 4 °C. Kimwipe wicks were made by twisting the Kimwipe into a thin wick 3-4 cm long and cutting with sterile scissors. Shortened pipette tips for tissue transfer were prepared by cutting 4-5 mm off a 1 mL pipette tip and returning to tip holder.

To wash sample tissues, a biosafety cabinet was equipped with a vortex, serological pipette, and ice bath. Samples to be processed were thawed on ice, and 10 mL of ice-cold water was added to each tube and allowed to equilibrate for 10 minutes. The tube was then vigorously vortexed for approximately 20 seconds until the tissue was completely resuspended in the water, adding more 10 second vortex bursts as needed until the tissue was completely detached from the tube wall. Once all samples were vortexed, they were transferred to a swinging bucket centrifuge with biocontainment lids and spun at 4,122 x g for 10 minutes at 4 °C. The supernatant was then aspirated, and the steps from water addition to aspiration were repeated twice more (sans 10 minute equilibration). After the last aspiration, it was ensured there was no gel at the bottom of the pellet, and 750 µL of ice-cold PBS in a shortened tip was used to resuspend and transfer all tissue to a 1.5 mL polypropylene tube kept on ice. Tubes were then spun at 7,000 x g for 7 minutes at 4 °C. As much supernatant as possible was aspirated, then the tubes were spun three

more minutes. The Kimwipe wicks were used to dab away any remaining wash solution without disturbing the pellet. The tubes were then weighed, and tissue weight was determined by subtracting original tube weight from tissue + tube weight. Another shortened pipette was used to collect the pellet in 300 µL ice-cold PBS and transfer it to the pre-labelled screw-cap tube containing 2 mL methanol. Samples were capped tightly and stored at -80 °C until ready for lipid extraction.

Samples and LC/MS internal standard were warmed to room temperature, and 250 pmol of internal standard was added to each tube (39). A homogenizer was used to triturate the tissue for approximately 20 seconds until no clumps of tissue were visible. The tube was then immersed in a sonicator bath for 5-10 seconds at a 45° angle to determine if clumps would re-form. If they did, the tissue was re-homogenized; if not, the tube was capped, and the next sample was processed. In the fume hood, 1 mL of LC/MS grade chloroform was added to each tube to achieve a 2:1:0.1 ratio of methanol:chloroform:water. Tubes were tightly capped, gently vortexed, and incubated overnight in a 48 °C water bath. The next day, samples were spun at 4,100 x g for 10 minutes at 4 °C to pellet insoluble debris. Each sample was decanted into a new glass test tube, which was run on a Savant Speed Vac SPD 2030 Integrated Vacuum Concentrator at 45 °C and 8 mTorr pressure for 5 hours, or until all samples were dry. Each sample was resuspended in 500 µL of LC/MS grade methanol by extensive vortexing and water bath sonication. Once completely resuspended, the samples were spun at 4,000 x g for 10 minutes, then decanted into autoloader vials without disturbing the pellet. Autoloader vials were capped and stored at -80 °C until MS, which was performed at the VCU Lipidomics Core.

Data from the Lipidomics Core was manually integrated using the software AB Sciex Analyst 1.6.2. Retention times were compared to the internal standard, and the area under the

peak was integrated and normalized to initial tissue weight to determine the pmol of lipid species per mg of tissue.

Results

Mass Spectrometry

Sixty-four paired tumor and normal head and neck tissue samples from 32 patients were obtained from the VCU Tissue Data and Acquisition Core (TDAAC), processed for analysis, analyzed by LC-ESI-MS/MS, and data integrated using Analyst 6.1.2 software. Lipidomics data were normalized to internal standards and tissue weights. Four samples were excluded from analysis due to low tissue weight (excluded if under 1.75 mg). Summary tables of p-values are listed in Tables 4-6.

Variations in Ceramide

Measurement of Cer levels at varying acyl-chain lengths (C14:0, C16:0, C18:1, C18:0, C20:0, C22:0, C24:1, C24:0, C26:1, and C26:0) identified a significant, race-independent increase in C16, C24:0, C26:1, and C26:0 Cer in tumor tissue compared to normal tissue [Figure 26A]. In African Americans, tumor tissue exhibited a significant increase in C22 and C24:1 Cer, but this difference was not significant in Caucasians [Figure 26B & C]. C26:1 Cer had significantly higher levels in combined (African American and Caucasian) tumor samples, but this increase was not observed in either African Americans or Caucasians when broken down by race. All other chain-length comparisons were nonsignificant. Comparison of normal tissues between races indicated that Caucasians have significantly more C24:1 Cer than African Americans [Figure 31A], but there were no significant racial differences in tumor tissue [Figure 32A]. In combined samples, mean total ceramide levels comprising all chain lengths was three

times higher in tumor tissue compared to normal tissue [Figure 22D]. There were no significant differences between African American and Caucasian total Cer levels in normal tissues or in tumor tissues [Figure 26E]. When separated by gender, both males and females exhibit an approximately threefold increase in total ceramide levels in tumors [Figure 26F]. There were no gender-dependent differences by chain length in normal or tumor tissues. In conclusion, increases of C16, C24:0, and C26:0 Cer in tumor tissues were seen in both races, while C22 and C24:1 Cer was only increased in African Americans. Total ceramide was increased in tumor tissues, and the trend was conserved when broken down by race or gender. Caucasian normal tissues have significantly more C24:1 Cer than African American normal tissues.

Variances in MonoHex

Measurement of MonoHex levels at varying acyl-chain lengths (C14:0, C16:0, C18:1, C18:0, C20:0, C22:0, C24:1, C24:0, C26:1, and C26:0) identified a significant, race-independent increase in C16, C24:1, C24:0, and C26:1 MonoHex in tumor tissue compared to normal tissue [Figure 27A]. In African Americans, tumor tissue exhibited a significant increase in C24:1 MonoHex, but this difference was not significant in Caucasians. C26:1 MonoHex had significantly higher levels in analysis of combined tumor samples, but this increase was not observed in either African Americans or Caucasians when broken down by race [Figure 27A-C]. All other chain-length comparisons were insignificant. There is significantly higher total MonoHex in tumor than normal tissues in combined samples [Figure 27D]. While the total ceramide levels in normal tissue between the two races is not significantly different, African Americans have significantly higher total MonoHex levels than Caucasians in tumor tissue. Thus, African American samples exhibited a more than threefold increase in MonoHex between normal and tumor tissues, while the increase in Caucasians is only twofold and nonsignificant

[Figure 27E]. Comparing normal or tumor tissue chain lengths by race resulted in no significant differences [Figures 31B, 32B]. When comparing by gender, there is no significant difference in chain length or total MonoHex between groups in normal or tumor tissues. Males have a significant increase in total MonoHex levels in tumor tissues, while the trend towards increased MonoHex levels in the tumor tissues of females is not statistically significant [Figure 27F]. In conclusion, increases of C16 and C24:0 MonoHex in tumor tissues was seen in both races, while C24:1 MonoHex was only significantly increased in African Americans. African American tumor tissues have significantly higher total MonoHex than Caucasian tumor tissue. There is a significant increase in total MonoHex in male tumor tissues, but the trend is not significant in females.

Variations in SM

Measurement of SM levels at varying acyl-chain lengths (C14:0, C16:0, C18:1, C18:0, C20:0, C22:0, C24:1, C24:0, C26:1, and C26:0) did not demonstrate any statistically significant differences between normal and tumor tissue in the combined group, nor when broken down by race [Figure 28A-C]. Comparison of normal or tumor tissues by race resulted in no significant differences [Figures 31C, 32C]. There were no significant differences in total SM levels between normal and tumor tissues when compared by race or gender [Figure 28D-F]. However, comparing tumor tissues by gender indicated females had statistically higher more C16 SM than males [Figure 33B], though there were no significant differences in normal tissue [Figure 33A]. In conclusion, there were no significant variations in SM when comparing normal to tumor tissues when broken down by race or gender. The only significant difference was a significant increase in C16 SM in female tumor tissues compared to male tumor tissues.

Variations in LacCer

Measurement of LacCer levels at varying acyl-chain lengths (C14:0, C16:0, C18:1, C18:0, C20:0, C22:0, C24:1, C24:0, C26:1, and C26:0) identified a significant, race-independent increase in C16, C24:1, and C24:0 LacCer in tumor tissue compared to normal tissue [Figure 29A]. There were no observed race-dependent variations in LacCer [Figure 29B & C]. Comparison of normal tissues by race indicated that Caucasians had significantly higher C16 LacCer than African Americans [Figure 31D], while there was no significant difference in tumor tissues [Figure 32D]. When comparing tumor tissues by gender, it was found that females had significantly higher C24:1 levels than males [Figure 33D], while there was no significant difference in normal tissues [Figure 33C]. All other chain-length comparisons were insignificant. Mean total LacCer was approximately fivefold higher in tumor tissue than normal tissue, with no significant differences when broken down by race or gender [Figure 29D-F]. In conclusion, increases in C16, C24:1, and C24:0 LacCer were significantly increased in the tumor tissue of both races. Total LacCer is significantly increased in tumor tissue, a trend conserved when broken down by race or gender. Caucasian normal tissue had significantly higher C16 LacCer than African American normal tissue, and female tumor tissue had significantly higher C24:1 LacCer than male tumor tissue.

Variations in So, DHSo, S1P, and DHS1P

For sphingosine (So) and sphingosine-1-phosphate (S1P), measured at acyl-chain length C18:1, and dihydrosphingosine (DHSo) and dihydrosphingosine-1-phosphate (DHS1P), measured at acyl-chain length C18:0, there were no significant differences between normal and tumor tissues in the combined group or when broken down by race or gender [Figure 30].

Discussion

Head and neck cancer comprises about 6% of cancer diagnoses every year and has a 5-year survival rate of only approximately 50% (63). Given that sphingolipids regulate many biological events and membrane structures, studying the role of these molecules in head and neck tumor pathogenesis may provide insights to disease progression, prognosis, and biomarkers. In this study Cer, MonoHex, LacCer, and SM were quantified at acyl chain lengths C14:0, C16:0, C18:1, C18:0, C20:0, C22:0, C24:1, C24:0, C26:1, and C26:0, and So, DHSo, S1P, and DHS1P were also quantified. Results were analyzed between tumor and normal tissue, and also compared by race, as African American patients have been identified as having worse HN prognoses than white patients. In Cer, MonoHex, and LacCer, C16 and C24 were found to be significantly elevated in the tumor tissue of both races. C24:1 LacCer was also elevated in tumor tissue of both races, while C24:1 Cer and MonoHex was only significantly elevated in African Americans. C26 Cer was also elevated in the tumor tissue of both races, as were both C26:1 Cer and MonoHex. Comparison of normal tissues indicated that Caucasians had significantly more C16 LacCer and C24:1 Cer than African Americans. When analyzed by gender, both C16 SM and C24:1 LacCer were significantly higher in the tumor tissue of females than males. Some variances in statistical significance are likely due to small sample population of females. No other significant variations were found in SM or So, DHSo, S1P, and DHS1P.

Identification of elevated C16, C24, and C24:1 in tumor tissue in this study is supported by similar published findings in HN (68), as well as other tissues like breast and colorectal cancer (32, 69). Interestingly, multiple publications on MS of HN report that tumor tissues exhibit a significant decrease in C18 Cer, which was not observed in this study (30, 68). It has been shown that C16 and C24 Cer induce apoptosis of dendritic cells, making high levels of these ceramides

a potential avoidance mechanism from immune surveillance (31). The increased levels of C22 and C24:1 Cer and C24:1 MonoHex in tumors in African American populations may contribute to the worse prognosis and more severe diagnoses presented in this demographic. Little remains published on the role of sphingolipid acyl chain lengths in cancer behavior and progression, and less is published on race dependent sphingolipid compositions of cancer. However, it has been discovered that C24:1 Cer limits the ability of ovarian cancer to metastasize by inhibiting lamellipodia formation (70). Given that C24:1 Cer had significantly higher concentrations in the normal tissue of Caucasians than in the normal tissue of African Americans, it is possible that the increased levels of C24:1 Cer reduces the severity of tumorigenesis by lowering metastatic potential. High expression of its synthase, CerS2, has been associated with lower cellular invasion and metastasis (71). Alternatively, higher levels of C24:1 Cer may just contribute to higher overall ceramide levels (though not indicated as statistically significant in this study), which has been shown to correlate with a lowered potency of proliferation in breast cancer (72). C16 SM was also found to be significantly increased in normal Caucasian tissues, but not African American tissues. While there is little published about the role of C16 SM, it is known that SM plays an important role in lipid raft formation and composition, and it has been shown that alteration of SM chain lengths can affect the ability of proteins to the lipid raft, with C16 SM preventing the association of several proteins (73). It is possible that the upregulation of C16 SM in Caucasian normal tissues results in Caucasians and African Americans having different lipid raft compositions, which could affect the signaling pathways leading to tumorigenesis. While the elevation of C16, C24, and C24:1 chain length levels in tumor tissues is a repeated and documented phenomenon, the race-dependent variations in normal tissues (C24:1 Cer and C16 SM) appear to be novel and warrant further study.

Chapter 1 Tables

Table 1. List of cell types used in this study, their tissue of origin, standard media and manufacturer, and dissociation solution.

Cell Line	Derivative Tissue	Culture Medium	Medium Manufacturer	Dissociation Solution
H460	Large cell lung carcinoma	RPMI + 10% FBS	Corning Ref. #10-040-CV	Trypsin
HBEC	Bronchial epithelial cells	Airway Epithelial Cell Basal Medium + Bronchial Epithelial Cell Growth Kit	ATCC Cat. #s PCS-300-030 & PCS-300-040	Trypsin/EDTA for Primary Cell Culture
HCT116	Colon carcinoma	DMEM + 10% FBS	ThermoFisher Cat. # 11054-001	Trypsin
HEK293FT	Embryonic kidney cells transformed with SV40 large T antigen	DMEM, high glucose, + 10% FBS	ThermoFisher Cat. # 12430-112	Trypsin
HeLa	Cervical adenocarcinoma	EMEM + 10% FBS	ThermoFisher Cat. # 11095-072	Trypsin
HN12	Head and neck carcinoma	DMEM + 10% FBS	ThermoFisher Cat. #11054-001	Trypsin
HT29	Colorectal adenocarcinoma	RPMI + 10% FBS	Corning Ref. #10-040-CV	Trypsin
SALE	Small airway epithelial cells	SABM + SAGM SingleQuots	Lonza Cat. # CC-3118	Trypsin/EDTA for Primary Cell Culture
SALEK	Small airway epithelial cells transduced with oncogenic, constitutively active mutated KRAS protein	SABM + SAGM SingleQuots	Lonza Cat. # CC-3118	Trypsin/EDTA for Primary Cell Culture
SKLU-1	Lung adenocarcinoma	EMEM + 10% FBS	ThermoFisher Cat. # 11095-072	Trypsin
SK-MES-1	Metastatic lung squamous cell carcinoma	EMEM + 10% FBS	ThermoFisher Cat. # 11095-072	Trypsin

Table 2. siRNA sequences used in this experiment.

Company	Product #	Sequence
Eupheria Biotech	EHU151711	GTCTCAGCTGAATGCCAACATCAAAACTCTGTTTGCCTTAG GAACTCCTAATCCACTGGAGGGAGAAGAACTACAAAGAAA ACTGGCTTGGGAAGATCAAAGGTACAATGATATAATTCAGC AAGACTTTGTTGATTCTTTCTACAATCTTACTCTGAAATTAC TTATGCAGTTCAGTTGGGCAAATACCTATTGTCCACATGCC AAATTTCTTATGACTGCTGATGATGACATATTTATTCACATG CCAAATCTGATTGAGTACCTTCAAAGTTTAGAACAAATTGG TGTTCAAGACTTTTGGATTGGTCGTGTTCATCGTGGTGCCCC TCCCATTAGAGATAAAAGCAGCAAATACTACGTGTCCTATG AAATGTACCAGTGGCCAGCTTACCCTGACTACACAGCCGG
Ambion	P/N: AM16704 siRNA ID#: 112254	Sense: CCAAUCGAUAAUCACAUUGtt Antisense: CAAUGUGAUUAUCGAUUGGtt

Table 3. p-values comparing HeLa and B3GNT5^{PKO} samples by acyl chain length in MS.

Acyl Chain Length	Cer	MonoHex	SM	LacCer	So/DHSo	S1P/DHS1P
C14	>0.9999	>0.9999	0.9998	>0.9999		
C16	>0.9999	**0.0066**	0.9599	0.9912		
C18:1	>0.9999	>0.9999	0.9932	>0.9999	0.1065	0.1767
C18:0	>0.9999	>0.9999	>0.9999	>0.9999	0.5336	0.8169
C20	>0.9999	>0.9999	>0.9999	>0.9999		
C22	0.9831	0.8414	0.9998	0.9988		
C24:1	**0.0001**	**<0.0001**	**0.029**	**<0.0001**		
C24	0.0989	**<0.0001**	0.6981	**<0.0001**		
C26:1	>0.9999	>0.9999	>0.9999	>0.9999		
C26	>0.9999	>0.9999		>0.9999		
Total	0.079238	**0.00851**	0.237158	**0.040769**		

Chapter 1 Figures

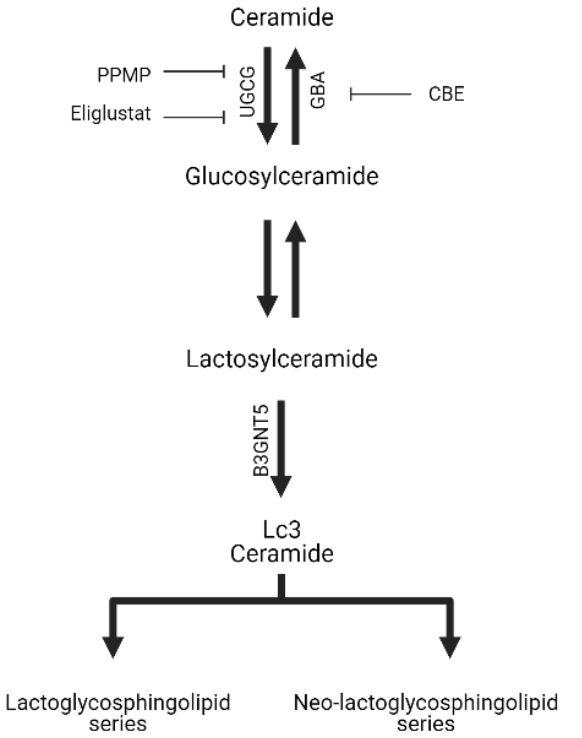

Figure 1. Ceramide to Lc3 Ceramide pathway. This diagram displays the sphingolipids of the pathway from ceramide to the lacto- and neo-lactosphingolipid series, along with the synthesizing enzymes and inhibitory drugs relevant to this study. Created in BioRender.com.

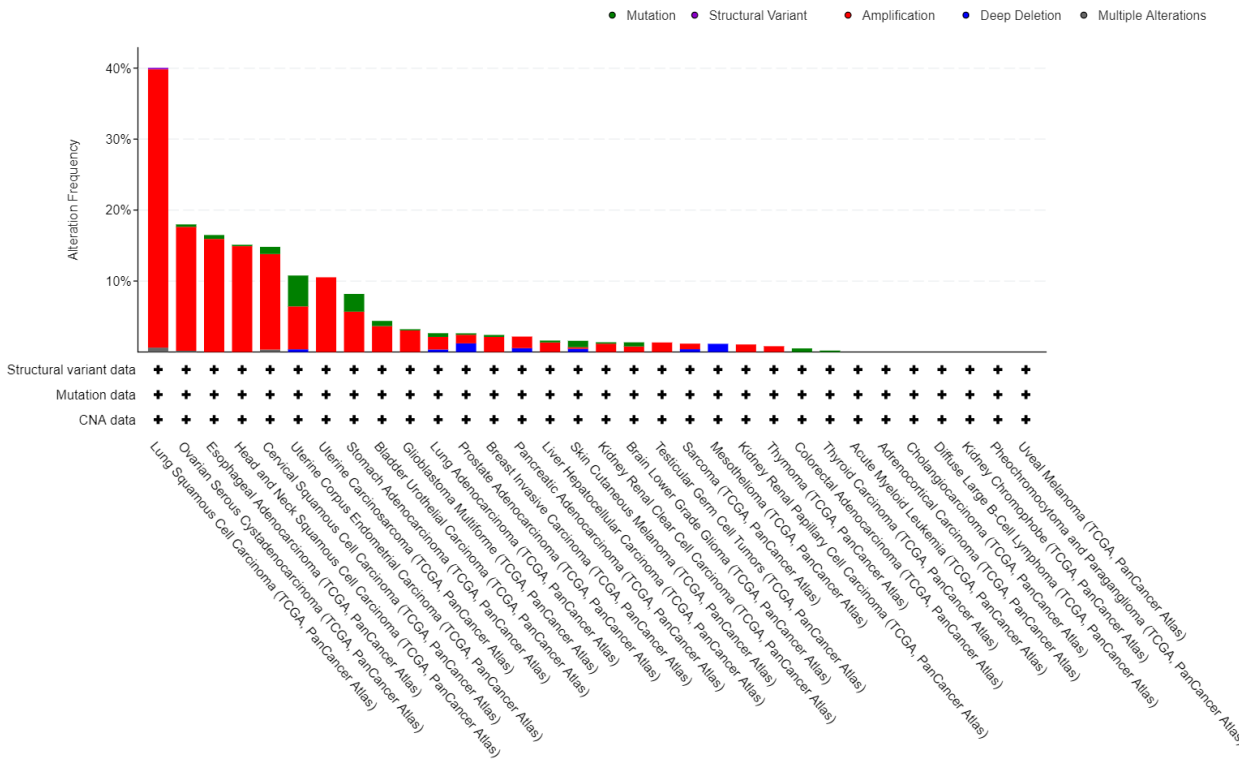

Figure 2. *B3GNT5* mutation characteristics by cancer type. Displayed are the frequency of *B3GNT5* alterations, color coded by alteration type (red signifies amplification, green signifies mutation, blue signifies deep deletion, grey signifies multiple alterations), in 32 categories of cancer compiled by The Cancer Genome Atlas (TCGA), generated with cBioPortal.

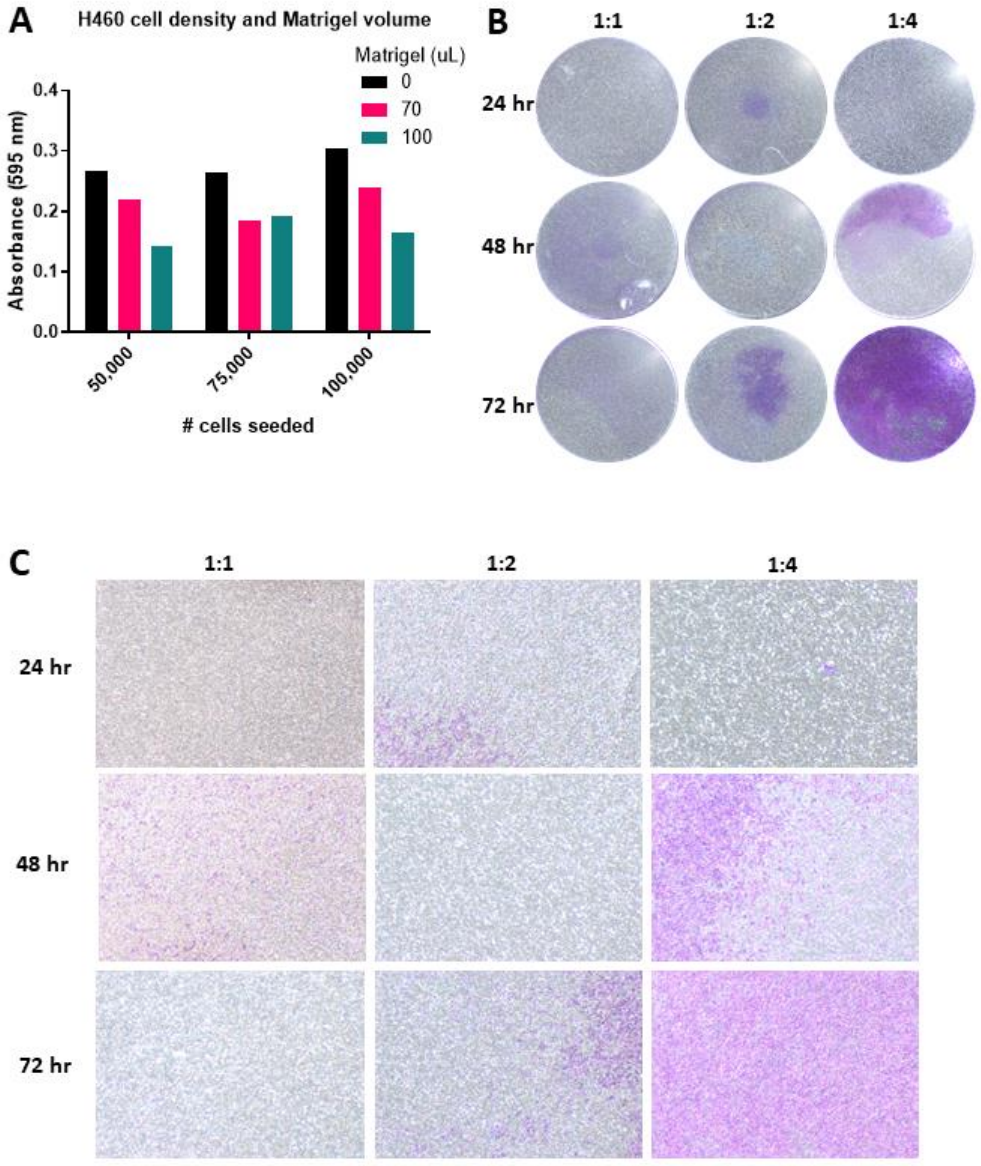

Figure 3. Transwell invasion assay optimization for Matrigel dilution, cell density, and incubation time. H460 cells on the bottom side of the Transwell membrane were fixed and stained with Crystal Violet. Purple staining indicates cells that have invaded through the Matrigel and were fixed to the posterior side of the membrane. **A:** Quantification of crystal violet staining eluted in acetic acid of 50,000-100,000 seeded cells in an empty insert or one containing 70 or 100 µL Matrigel (n=1). **B:** Inverted microscope images at 1X of stained inserts having contained a 1:1, 1:2, or 1:4 Matrigel-to-medium ratio, incubated 24-72 hours (n=1). **C:** Samples from B shown at 3X.

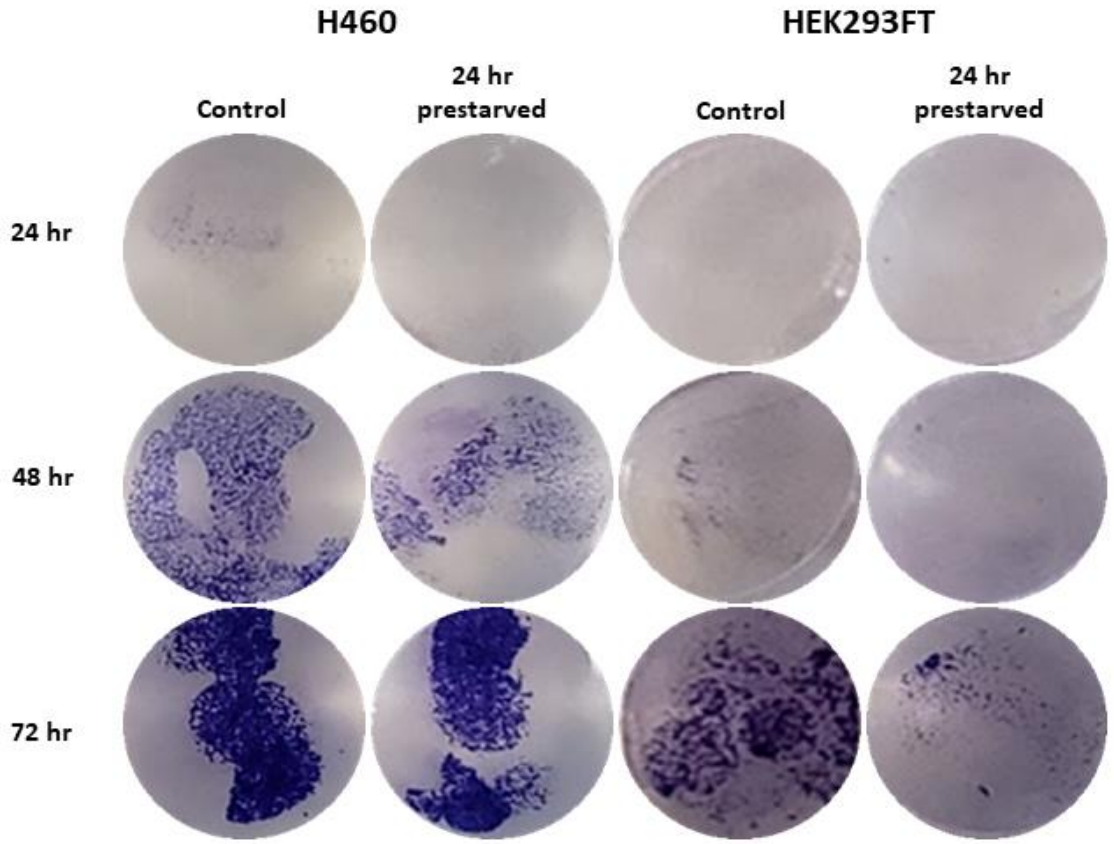

Figure 4. Effects of FBS prestarvation on transwell invasion. H460 and HEK293 cells received either standard, FBS-containing media (control) or standard media not containing FBS (prestarved) 24 hours before assay seeding. Wells fixed and stained 24, 48, or 72 hours after seeding (n=1).

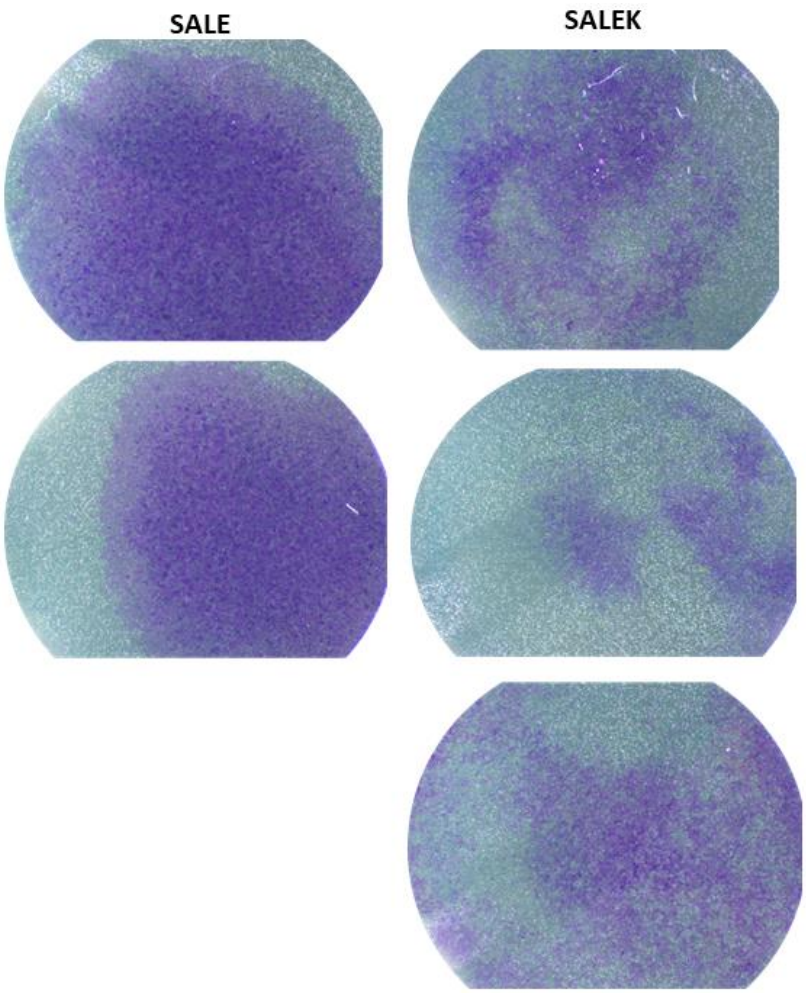

Figure 5. Comparing SALE and SALEK transwell invasion. SALE and SALEK cells were run in triplicate through Transwell Invasion Assay. Imaged via inverted microscope at 1.5X. Third SALE triplicate image lost.

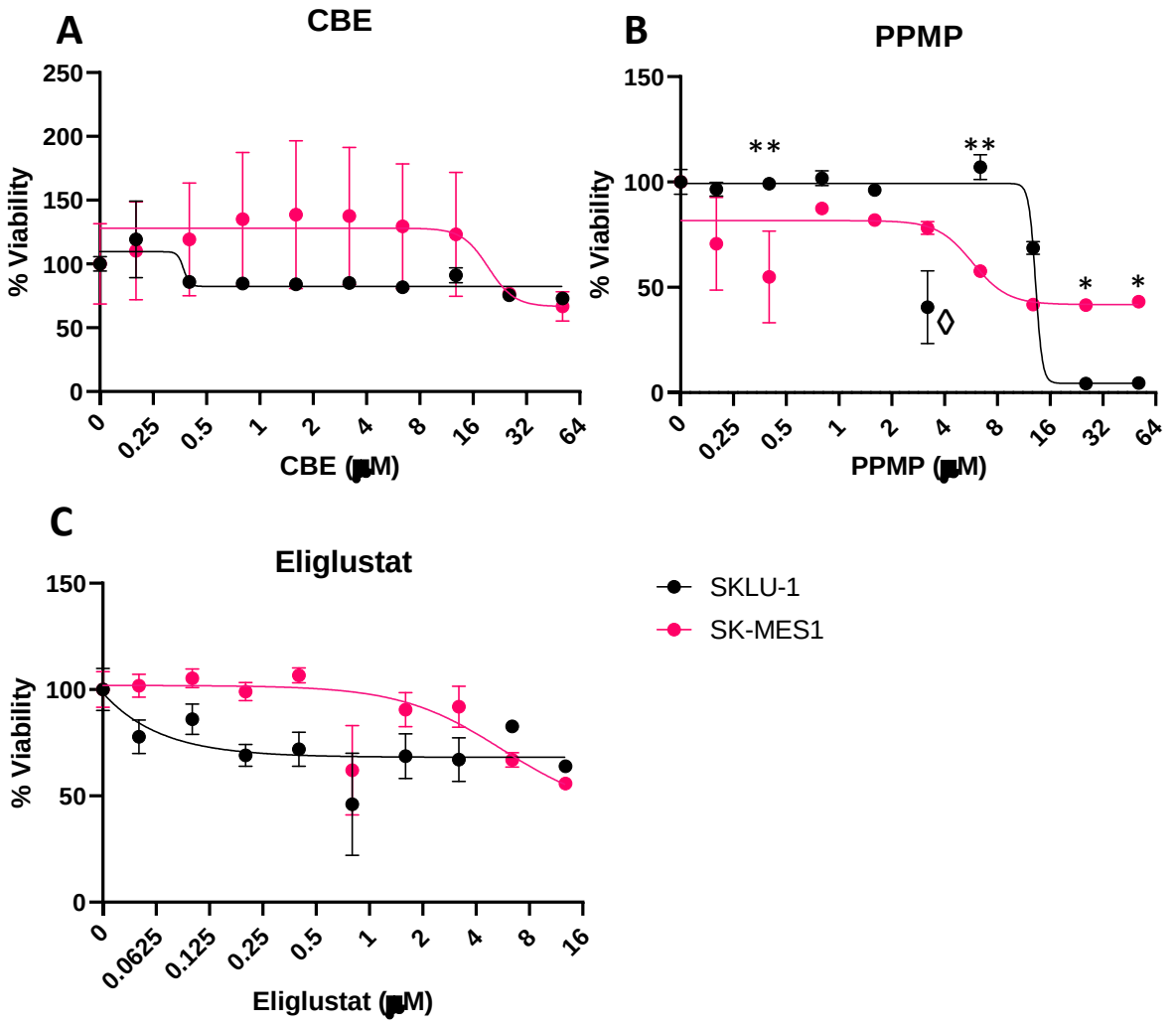

Figure 6. CCK-8 Assay of SKLU-1 and SK-MES-1 at varying concentrations of CBE, PPMP, and eliglustat. Two lung cancer lines were treated in triplicate with **A:** CBE (0-51.2 µM), **B:** PPMP (0-51.2 µM), or **C:** Eliglustat (0-12.8 µM) for 72 hrs. 2-way ANOVA with Sidak multiple comparisons test was used. XY plot graphs were used with a log(2) X axis. Error bars represent SEM. Percent viability was calculated by averaging the absorbance values, dividing each drug concentration by the untreated group, then multiplying by 100. Lines of best fit generated by nonlinear robust regression: inhibitor vs response, variable slope. * $p \leq 0.05$; ** $p \leq 0.01$, *** $p \leq 0.001$, and **** $p \leq 0.0001$; all other values are nonsignificant. ◊ indicates statistical outlier excluded from multiple comparisons test.

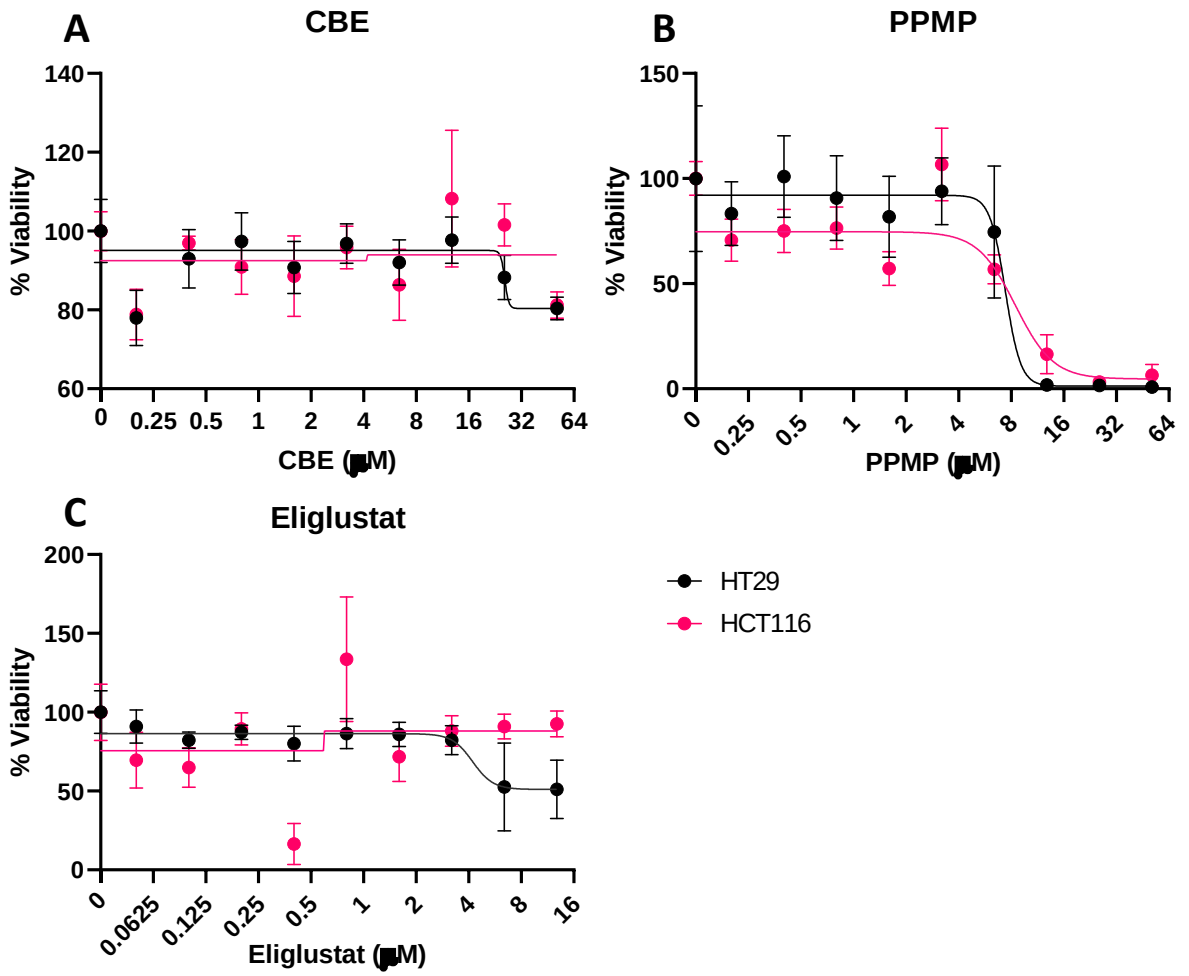

Figure 7. CCK-8 Assay of HT29 and HCT116 at varying concentrations of CBE, PPMP, and eliglustat. Two colon cancer lines were treated in triplicate with **A:** CBE (0-51.2μM), **B:** PPMP (0-51.2 μM), or **C:** Eliglustat (0-12.8 μM) for 72 hrs. 2-way ANOVA with Sidak multiple comparisons test was used. XY plot graphs were used with a log(2) X axis. Error bars represent SEM. Lines of best fit generated by nonlinear robust regression: inhibitor vs response, variable slope. Percent viability was calculated by averaging the absorbance values, dividing each drug concentration by the untreated group, then multiplying by 100. There were no significant differences between cell types.

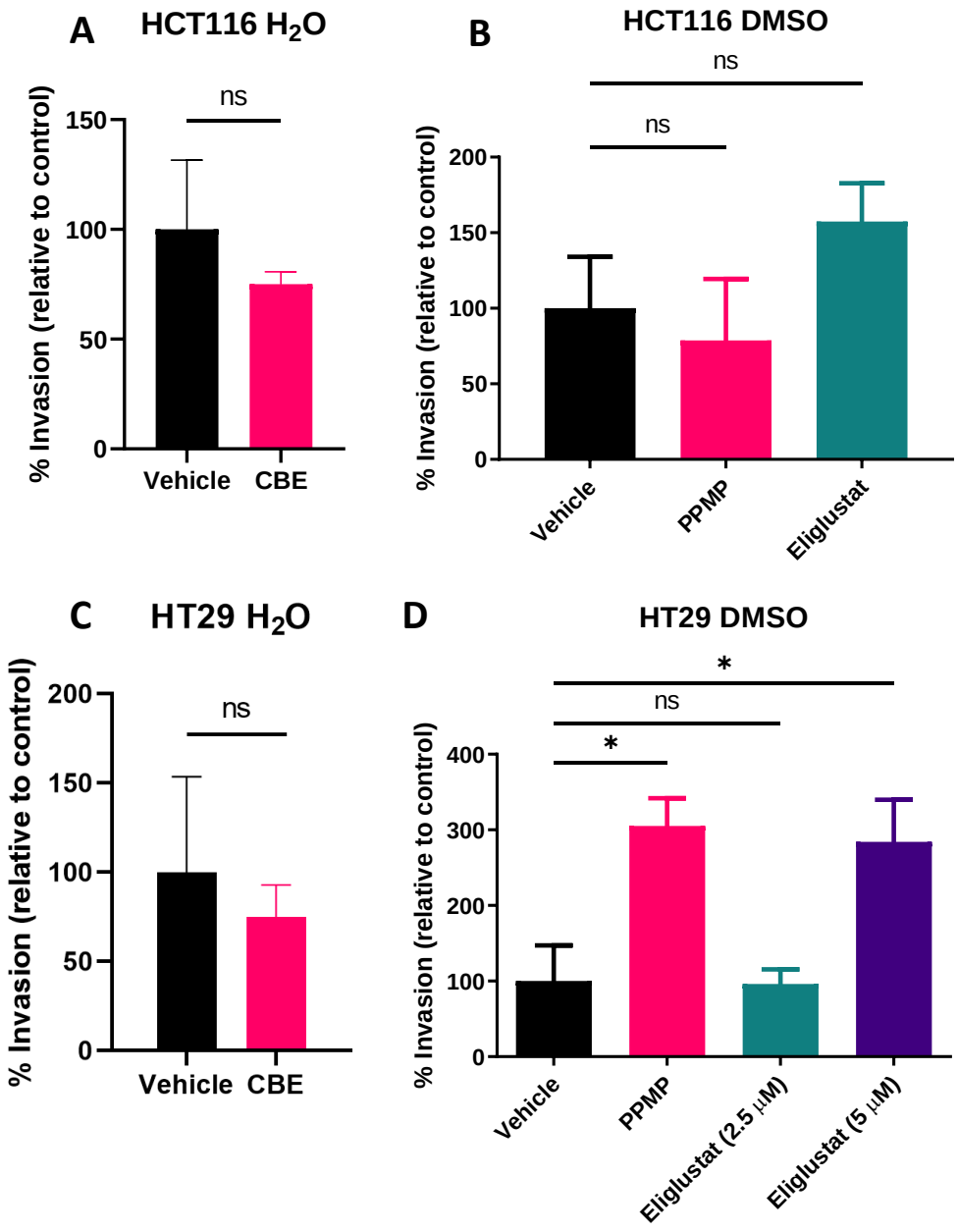

Figure 8. Transwell invasion quantification of HT29 and HCT116 treated with CBE, PPMP, or eliglustat. Two colon cancer lines were treated in triplicate with CBE (water soluble) or PPMP or Eliglustat (DMSO soluble), incubated in an invasion assay for 72 hours, then quantified via crystal violet elution. **A & C:** HCT116 or HT29 treated with water or CBE (50 µM). **B:** HCT116 treated with DMSO, PPMP (6 µM), or eliglustat (2.5 µM). **D:** HT29 treated with DMSO, PPMP (6 µM), or eliglustat (2.5 µM or 5 µM). Percent invasion was calculated by averaging the absorbance values, dividing each group by the vehicle, then multiplying by 100. Statistical significance determined by unpaired t-test for A&C, and Dunnett's multiple comparisons test for B&D. Error bars represent SEM. ns represents not significant; * $p \leq 0.05$; ** $p \leq 0.01$, *** $p \leq 0.001$, and **** $p \leq 0.0001$.

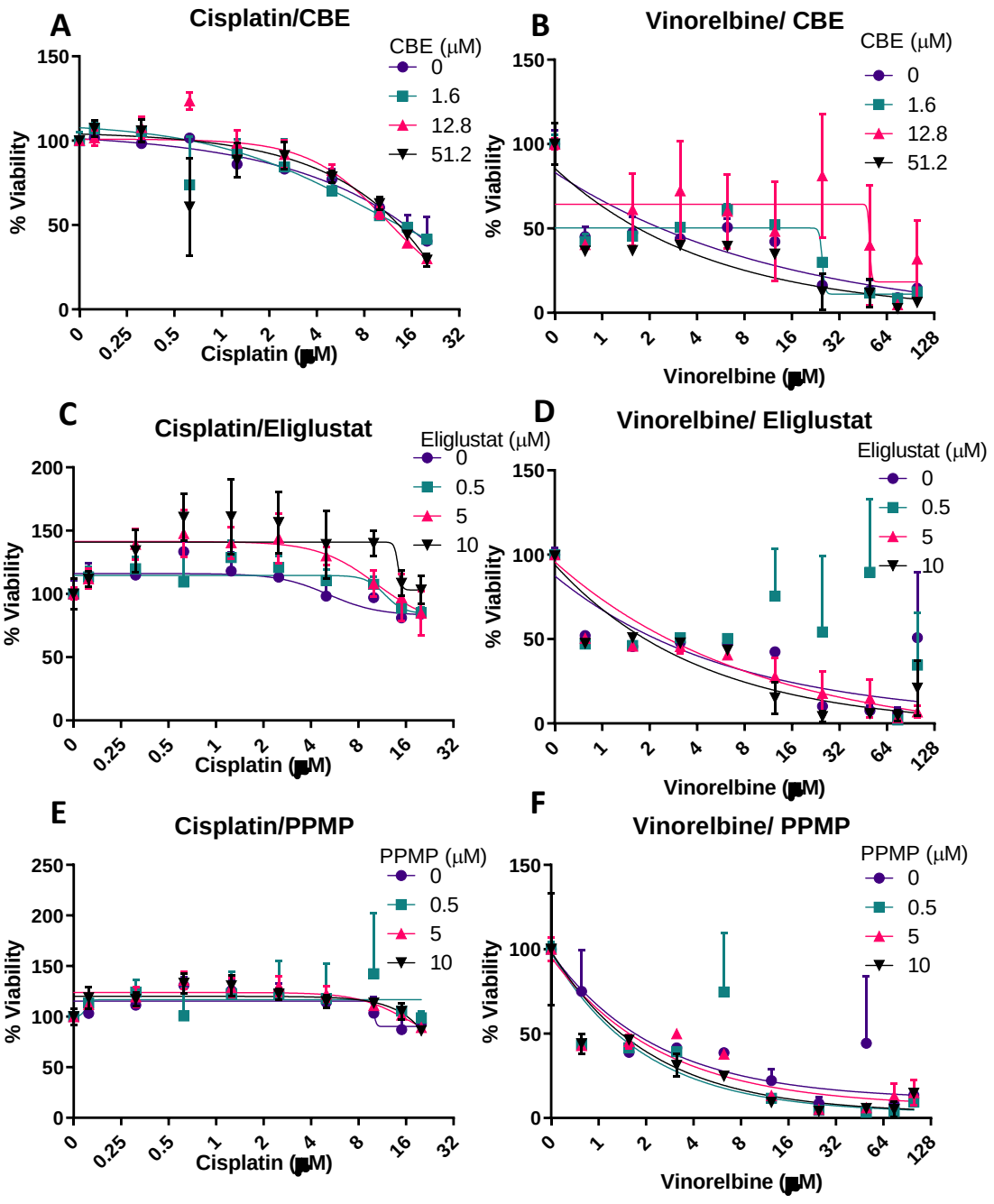

Figure 9. CCK-8 Assay of HCT116 co-treated with CBE, eliglustat, or PPMP and cisplatin or vinorelbine. HCT116 cells were treated in triplicate with **A&B:** CBE (0, 1.6, 12.6, or 51.2 μM), **C&D:** eliglustat (0, 0.5, 5, or 10 μM), or **E&F:** PPMP (0, 0.5, 5, or 10 μM), then treated with either **A,C,E:** cisplatin (0-20 μM) or **B,D,F:** vinorelbine (0-100 μM). 2-way ANOVA with Dunnett multiple comparisons test was used. XY plot graphs were used with a log(2) X axis. Error bars represent SEM. Lines of best fit generated by nonlinear robust regression: inhibitor vs response, variable slope. Percent viability was calculated by averaging the absorbance values, dividing each drug concentration by the untreated group, then multiplying by 100. There were no significant differences between zero and maximum drug concentration. Line of best fit could not be established for **D** at 0.5 μM Eliglustat.

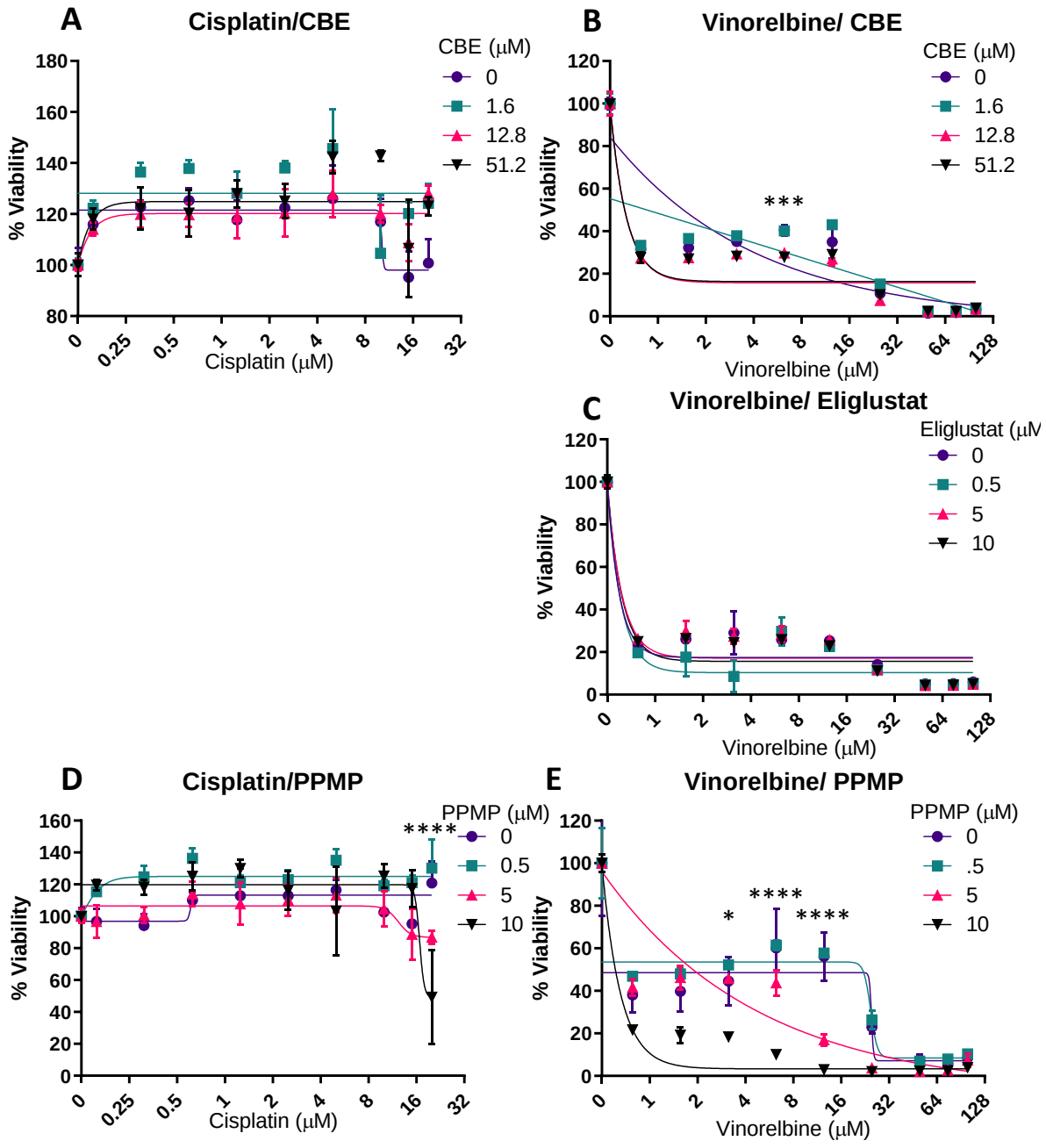

Figure 10. CCK-8 assay of HT29 co-treated with CBE, eliglustat, or PPMP and cisplatin or vinorelbine. HT29 cells were treated in triplicate with **A&B:** CBE (0, 1.6, 12.6, or 51.2 μM), **C:** eliglustat (0, 0.5, 5, or 10 μM), or **D&E:** PPMP (0, 0.5, 5, or 10 μM), then treated with either **A,D:** cisplatin (0-20 μM) or **B,C,E:** vinorelbine (0-100 μM). Cisplatin with eliglustat was not performed. 2-way ANOVA with Dunnett multiple comparisons test was used. XY plot graphs were used with a log(2) X axis. Error bars represent SEM. Lines of best fit generated by nonlinear robust regression: inhibitor vs response, variable slope. Percent viability was calculated by averaging the absorbance values, dividing each drug concentration by the untreated group, then multiplying by 100. Significance values from comparison between 0 and maximum drug concentration: * $p \leq 0.05$; ** $p \leq 0.01$, *** $p \leq 0.001$, and **** $p \leq 0.0001$.

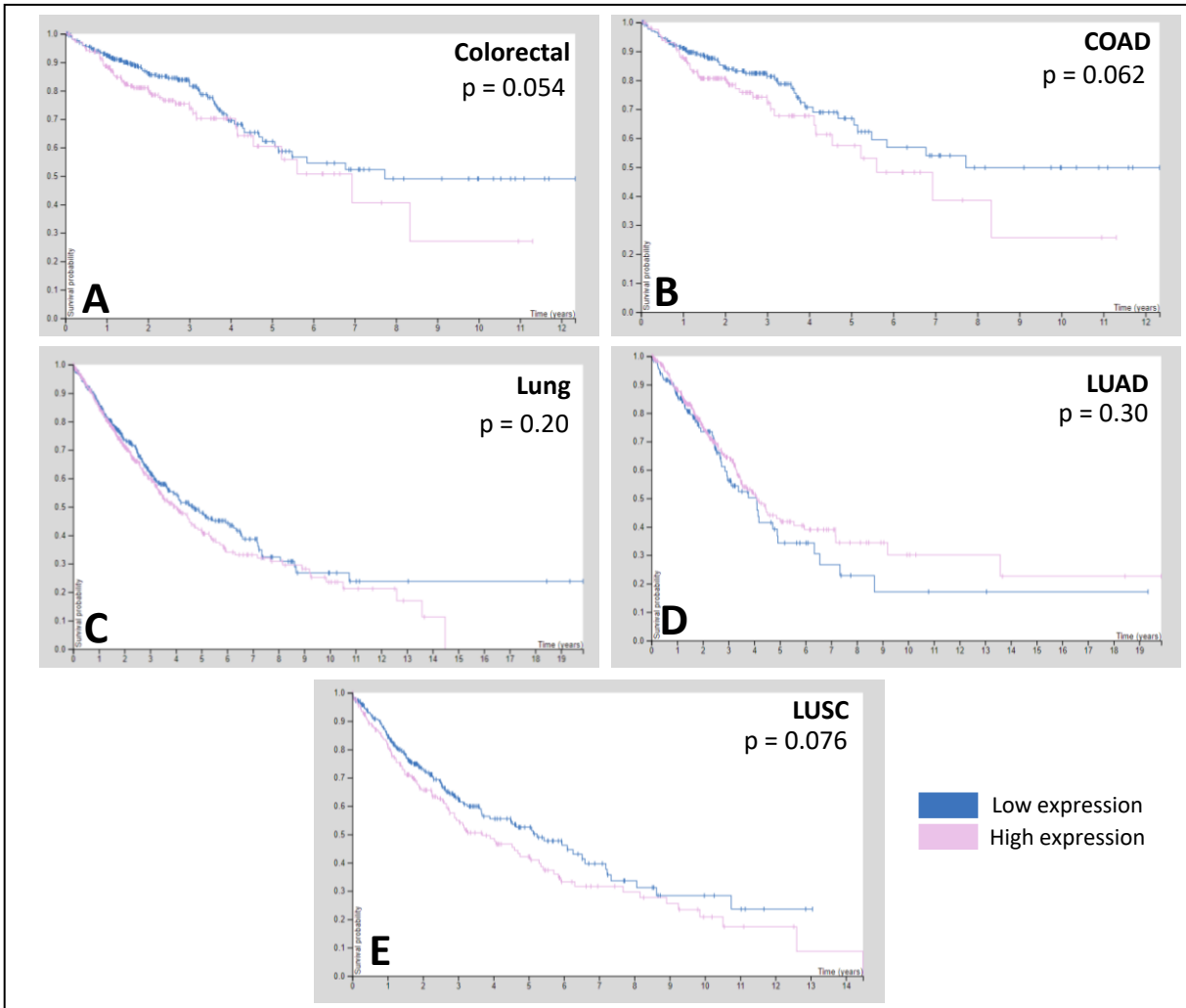

Figure 11. Kaplan-Meier plots for UGCG. Kaplan-Meier plots of survival probability relative to time (in years), where low UGCG mRNA expression is shown in blue and high expression in pink, as obtained from TCGA. **A:** Colorectal cancer – p=0.054. **B:** Colorectal adenocarcinoma – p=0.062. **C:** Lung cancer – p=0.20. **D:** Lung adenocarcinoma – p=0.30. **E:** Lung squamous carcinoma – p=0.076.

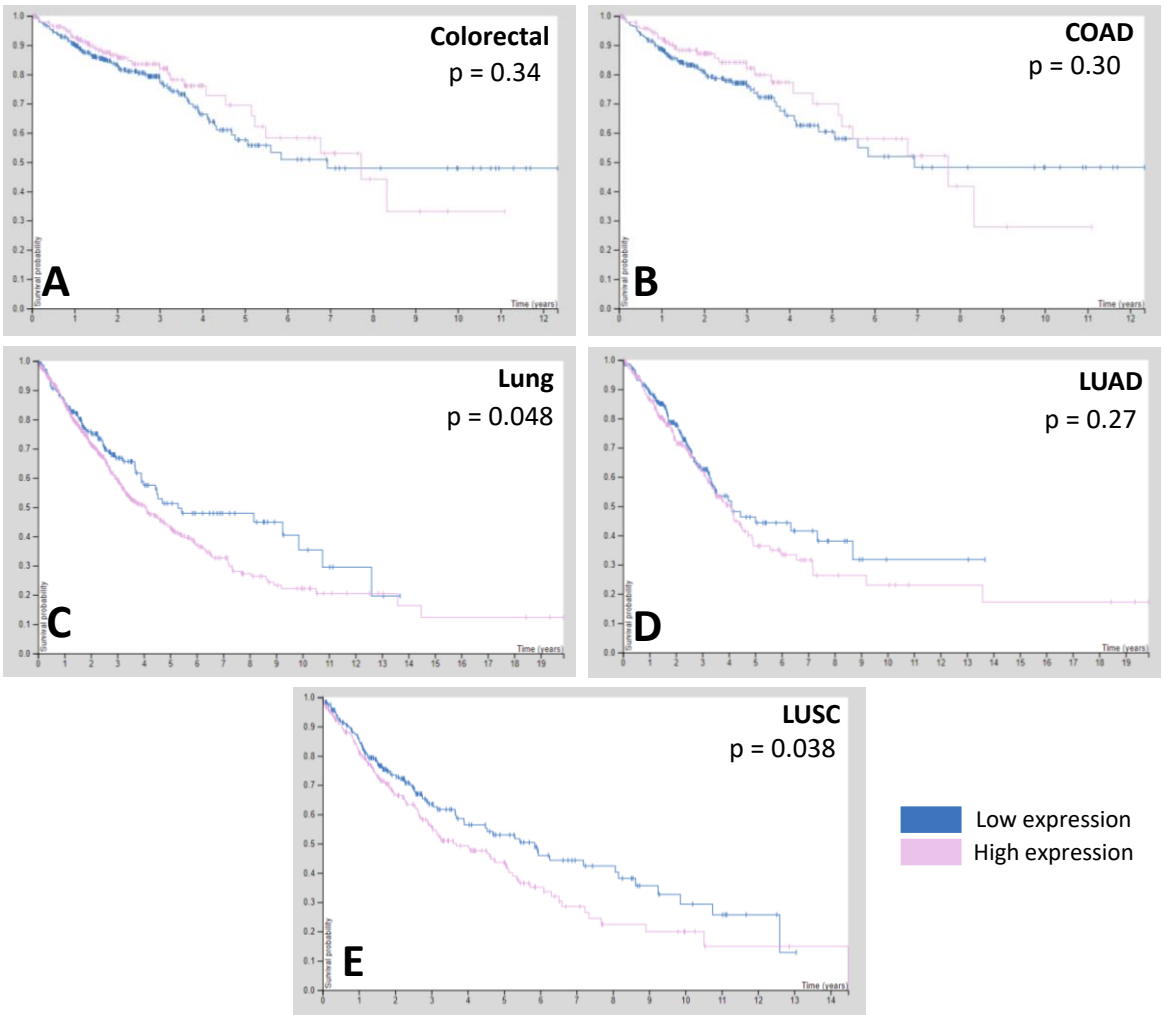

Figure 12. Kaplan-Meier plots for GBA. Kaplan-Meier plots of survival probability relative to time (in years), where low GBA mRNA expression is shown in blue and high expression in pink, as obtained from TCGA. **A:** Colorectal cancer – p=0.34. **B:** Colorectal adenocarcinoma – p=0.30. **C:** Lung cancer – p=0.048. **D:** Lung adenocarcinoma – p=0.27. **E:** Lung squamous carcinoma – p=0.038.

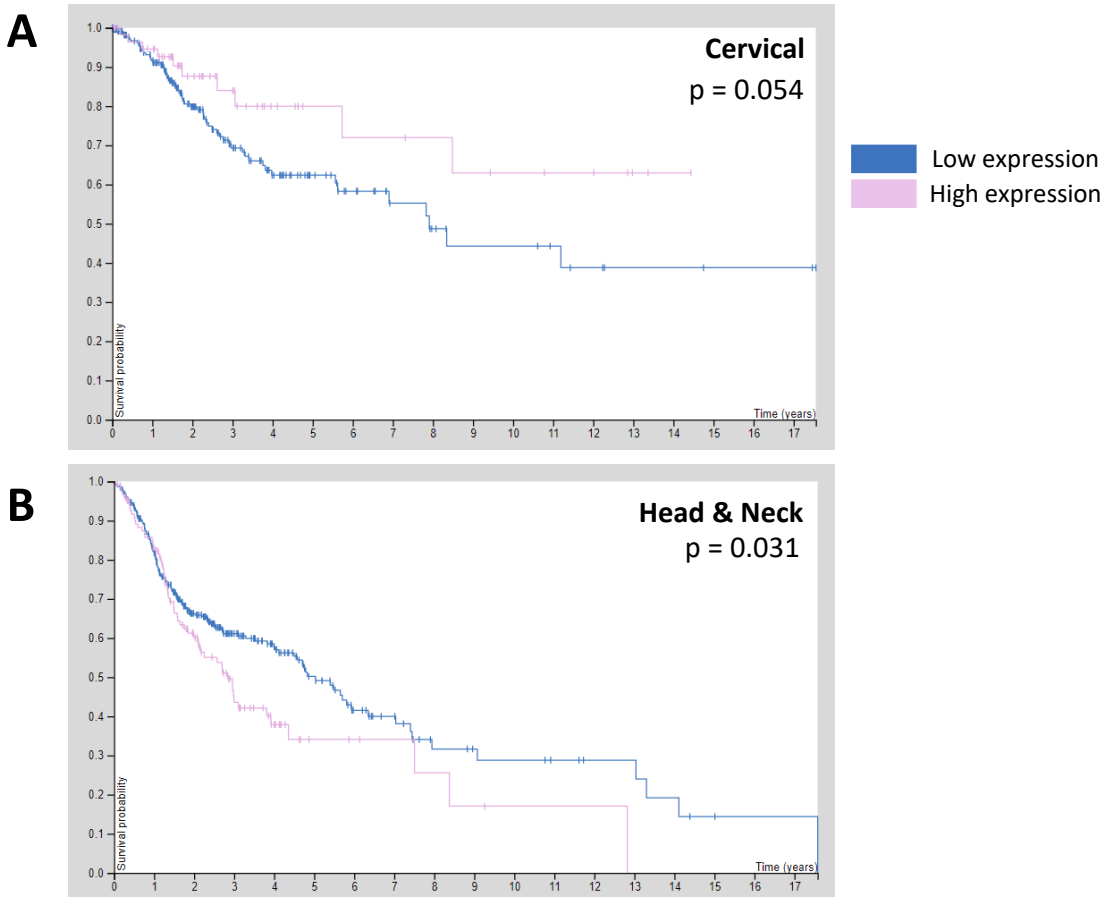

Figure 13. Kaplan-Meier plots for B3GNT5. Kaplan-Meier plots of survival probability relative to time (in years), where low B3GNT5 mRNA expression is shown in blue and high expression in pink, as obtained from TCGA. **A:** Cervical cancer – p=0.054. **B:** Head & neck cancer – p=0.031.

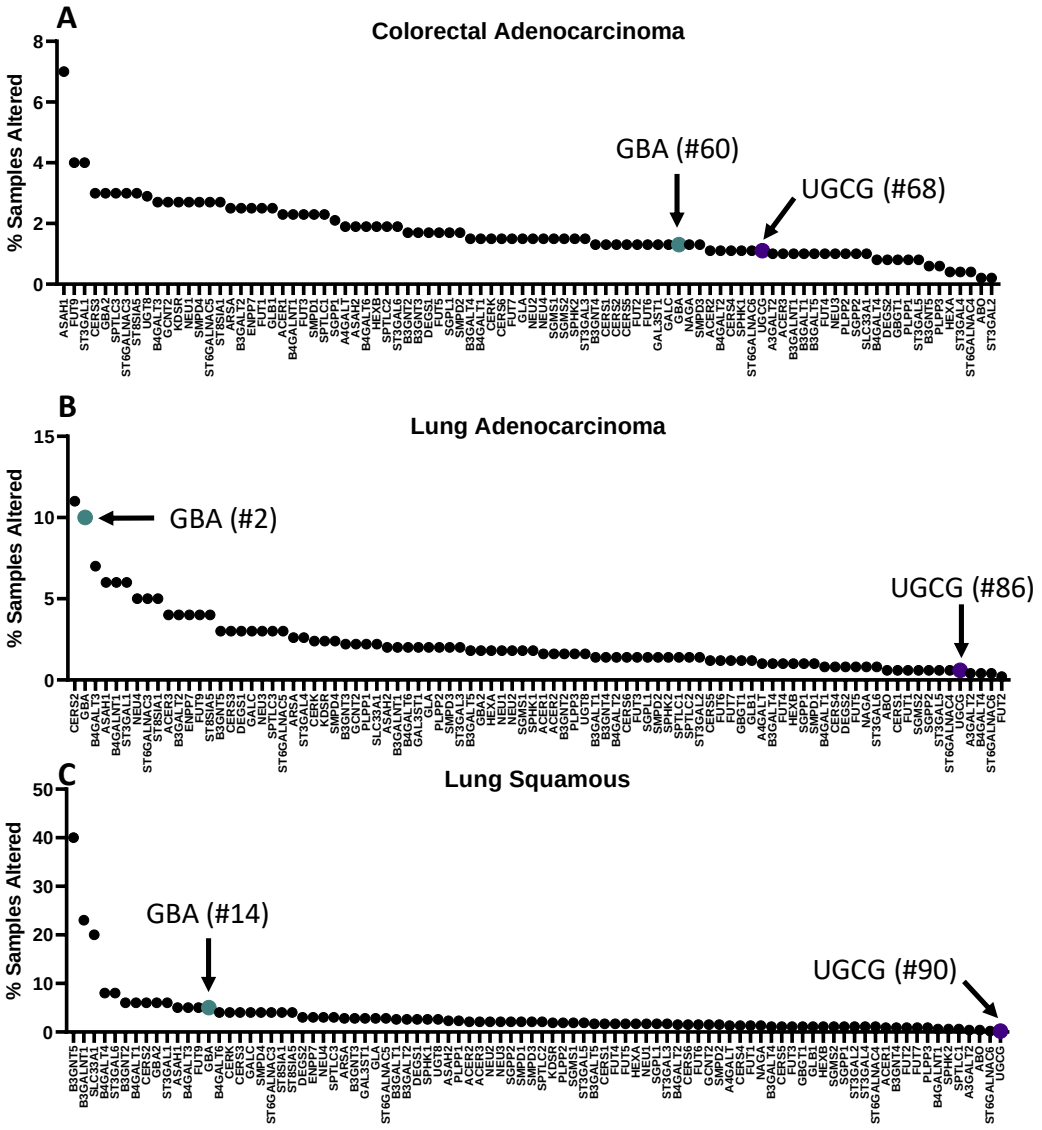

Figure 14. Rates of alteration of GBA and UGCG. Percentage of alteration occurrence in tumor samples compiled by the THPA "PanCan" survey on cBioPortal, comparing the rates of alteration of the 90 genes involved in sphingolipid biosynthesis. There is no non-adeno colon carcinoma repository. GBA is highlighted in teal, and UGCG in purple. **A:** Colorectal adenocarcinoma (n=526). **B:** Lung adenocarcinoma (n=507). **C:** Lung squamous carcinoma (n=469).

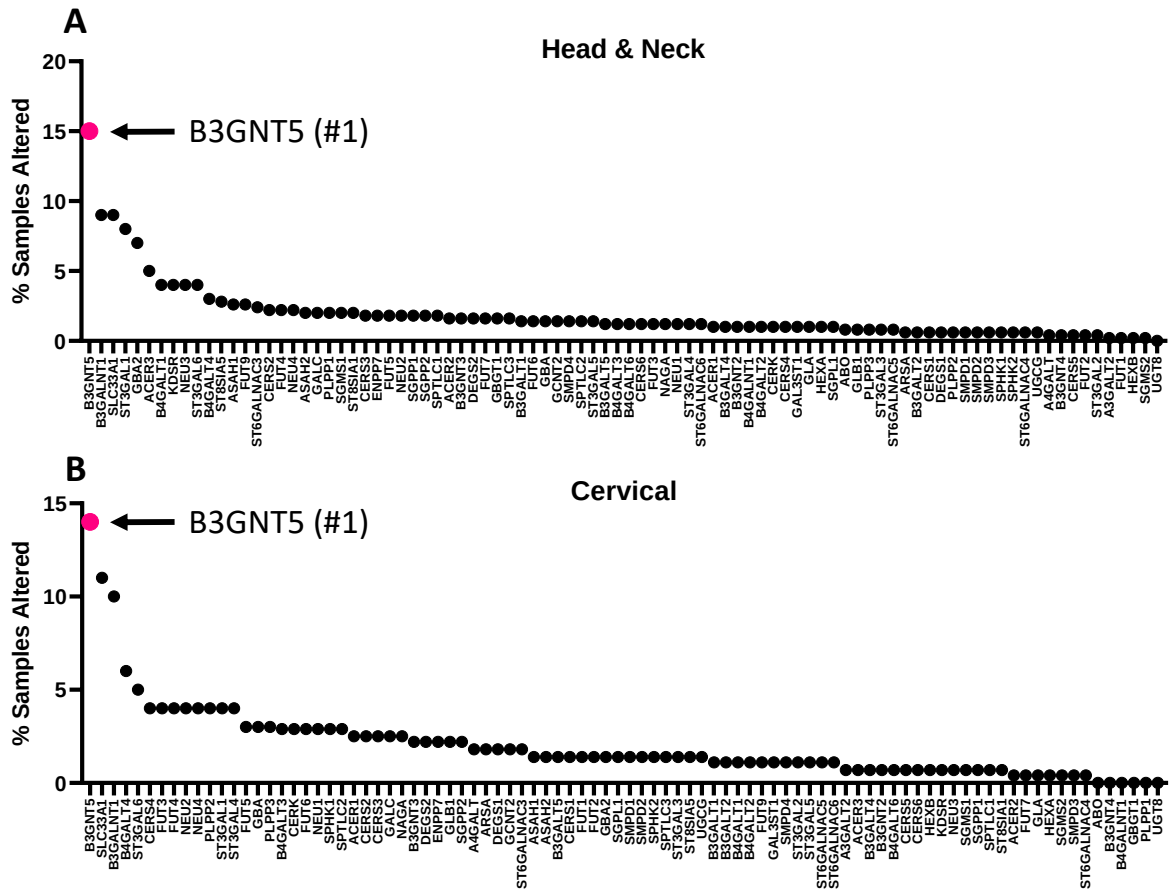

Figure 15. Rate of alteration of B3GNT5. Percentage of alteration occurrence in tumor samples compiled by the THPA "PanCan" survey, comparing the rates of alteration of the 90 genes involved in sphingolipid biosynthesis. B3GNT5 is highlighted in magenta. **A:** HN Cancer (n=496). **B:** Cervical cancer (n=273).

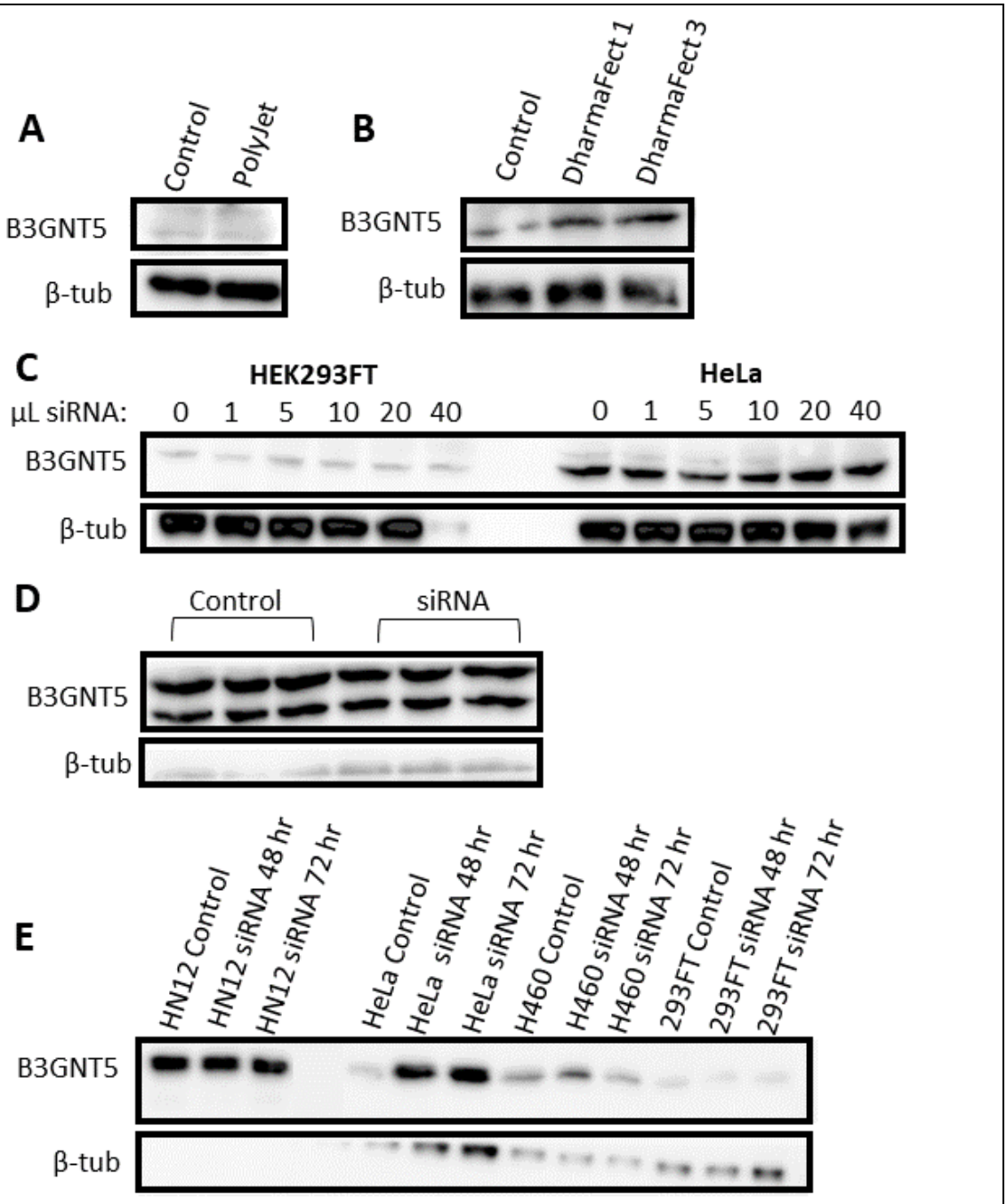

Figure 16. B3GNT5 siRNA knockdown attempts. Western blots of multiple attempted siRNA knockdowns. In blots with two bands, B3GNT5 is the top one. **A:** HEK293FT transfected with Sigma siRNA with PolyJet as a transfection reagent (n=1). **B:** HEK293FT transfected with Sigma siRNA with DharmaFect1 or 3 as transfection reagent (n=1). **C:** HEK293FT or HeLa reverse transfected with 0-40 µL Sigma siRNA with Lipofectamine 2000 as transfection reagent (n=1). **D:** HeLa reverse transfected with 20 µL Sigma siRNA in triplicate with Lipofectamine 2000 as transfection reagent. **E:** HN12, HeLa, H460, and HEK293FT transfected with Ambion siRNA with Lipofectamine as a transfection reagent with 48 or 72 hour incubations (n=1).

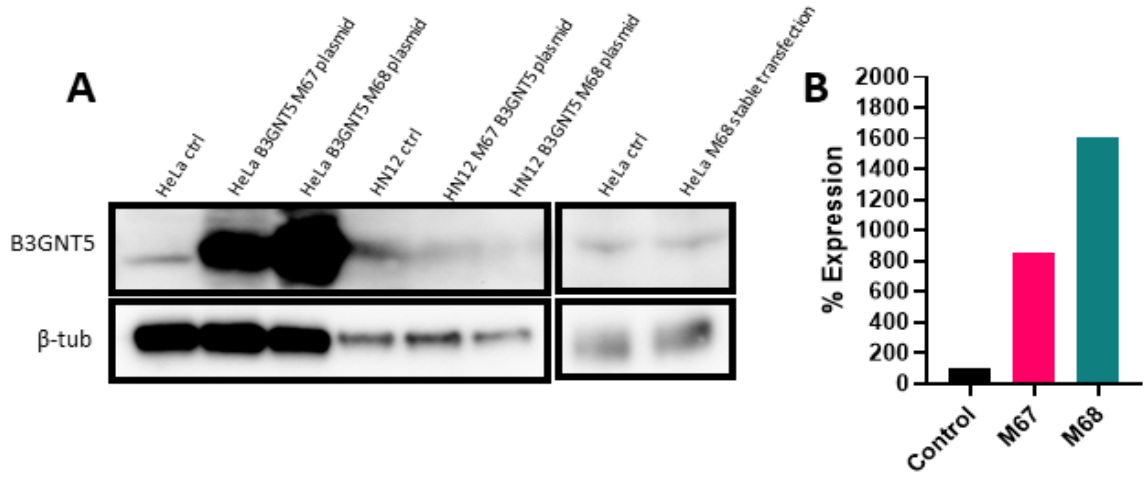

Figure 17. B3GNT5 plasmid expression. Transient and stable transfection of HeLa and HN12 with B3GNT5 plasmid. **A:** HeLa and HN12 transiently transfected with B3GNT5 M67 and M68 plasmid, as well as HeLa after several passages of stably transfected M68 plasmid (Proteintech antibody). **B:** ImageJ quantification of B3GNT5 expression after transfection from blot A, normalized to the control and β-tub expression (n=1).

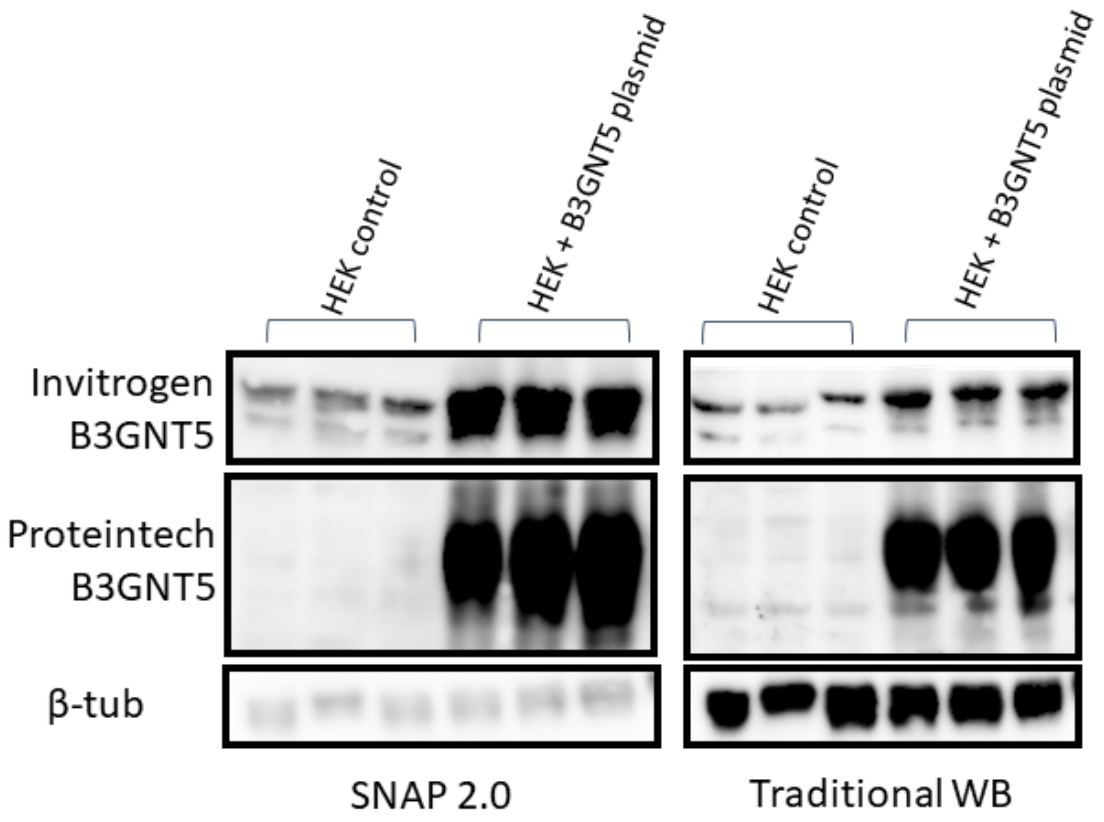

Figure 18. Comparing B3GNT5 antibodies and Western blotting techniques. Western blots testing B3GNT5 antibodies obtained from Invitrogen and Proteintech using HEK293FT and HEK293FT transiently transfected with B3GNT5 M68 plasmid. Both SNAP 2.0 quick Western blotting and traditional overnight incubation Western blotting were compared (n=3).

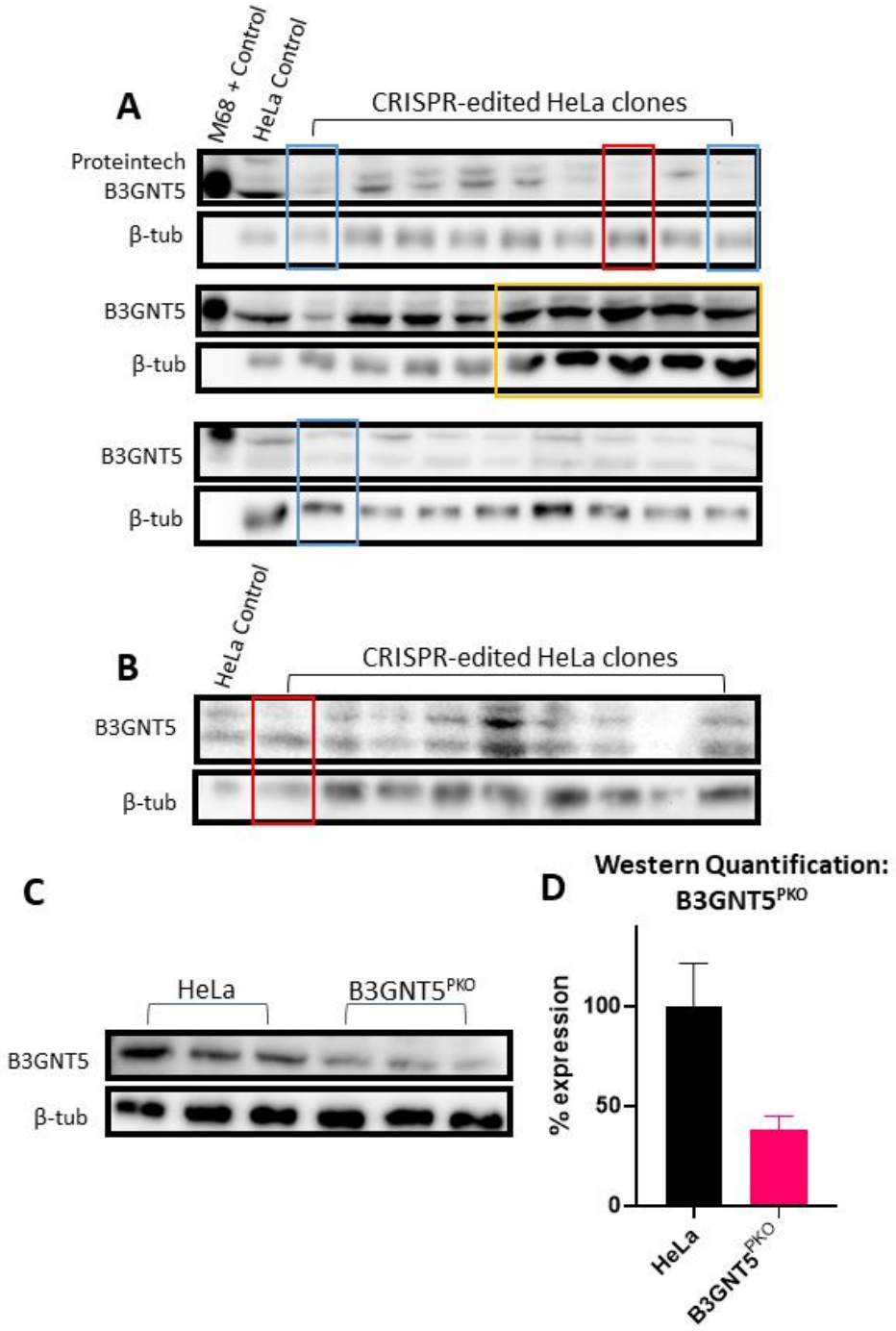

Figure 19. Screening for CRISPR-edited B3GNT5 knockout HeLa clones. Screening of polyclonal and monoclonal lines for B3GNT5 reduction or absence using Proteintech antibody. **Red box** indicates clone selected for future experiments, "B3GNT5^{PKO}"; **blue boxes** indicate backup stocks; **yellow box** indicates polyclonal edited stocks. **A:** Western blotting of edited lines using traditional sample dilution method. **B:** Western blotting of monoclonal edited lines using TCA precipitation. **C:** Triplicate samples of selected clone, B3GNT5^{PKO}. **D:** ImageJ quantification of B3GNT5 expression in C, normalized to samples' β-tub expression, compared by unpaired t-test ($p = 0.0518$, n=3). Calculated by dividing sample peak area of B3GNT5 by peak area of β-tub, averaging triplicates, dividing by control HeLa expression, and multiplying by 100.

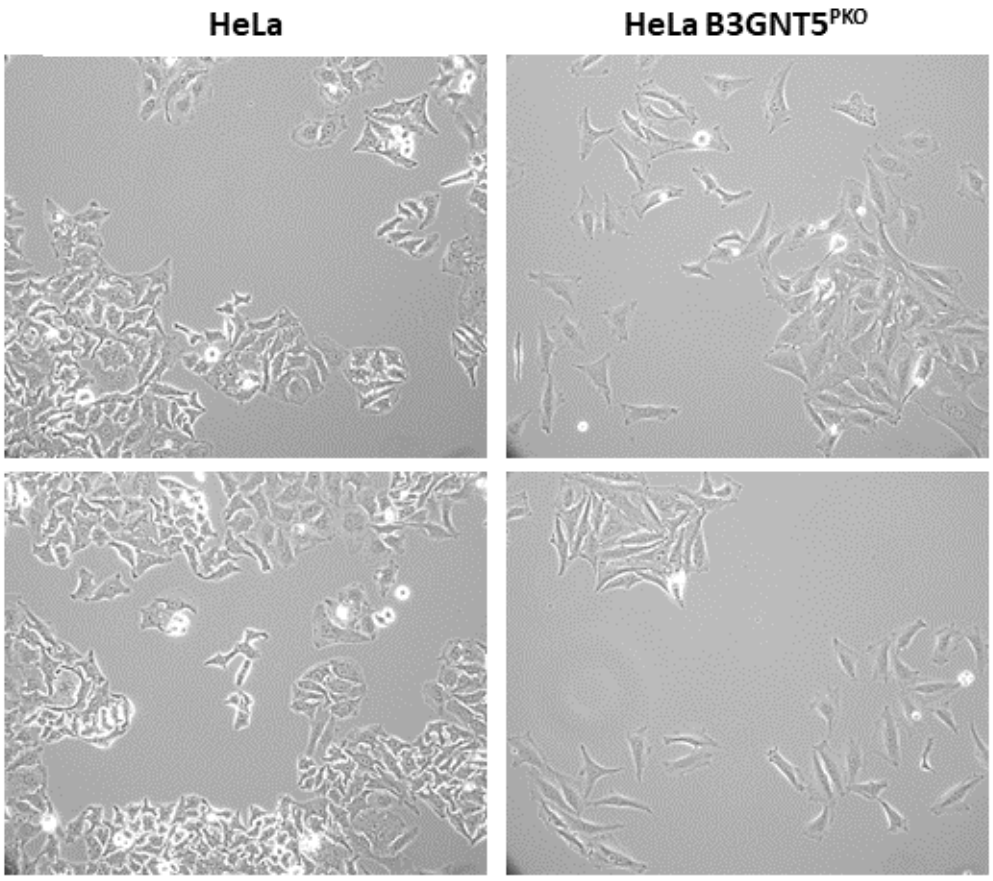

Figure 20. Images of HeLa and HeLa B3GNT5^{PKO}. Two images of HeLa and HeLa B3GNT5^{PKO}, taken at 20X magnification directly after fresh media change. B3GNT5^{PKO} cells appear to grow separately, while normal HeLa cells grow largely in clusters.

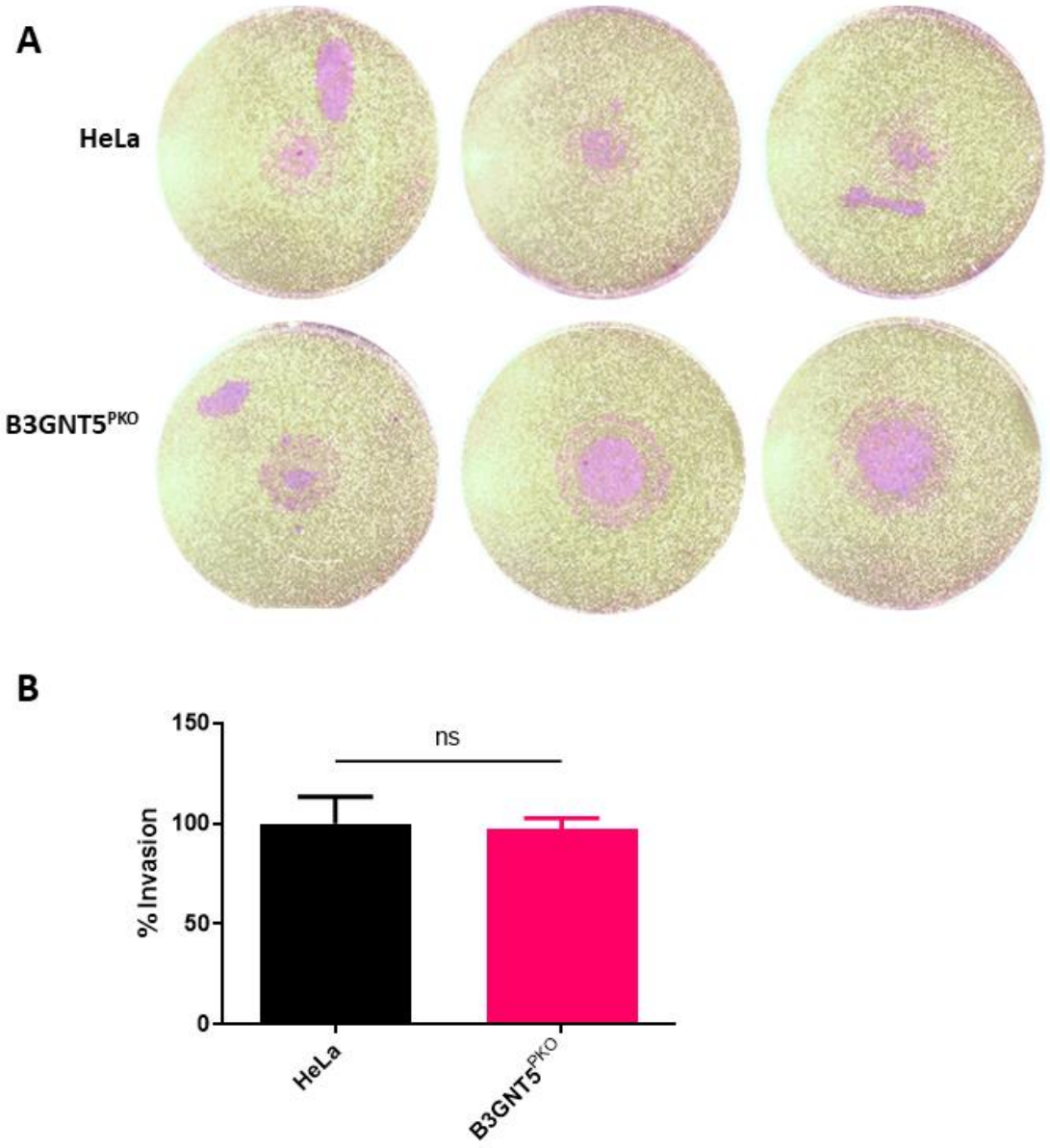

Figure 21. Transwell invasion of HeLa and HeLa B3GNT5^{PKO}. Triplicates of HeLa vs HeLa B3GNT5^{PKO} run through a Transwell Invasion assay and quantified. **A:** 1X imaging of Crystal Violet stained inserts. **B:** Quantification of Crystal Violet elution in acetic acid, normalized to HeLa invasion and compared using unpaired t-test. ns= nonsignificant.

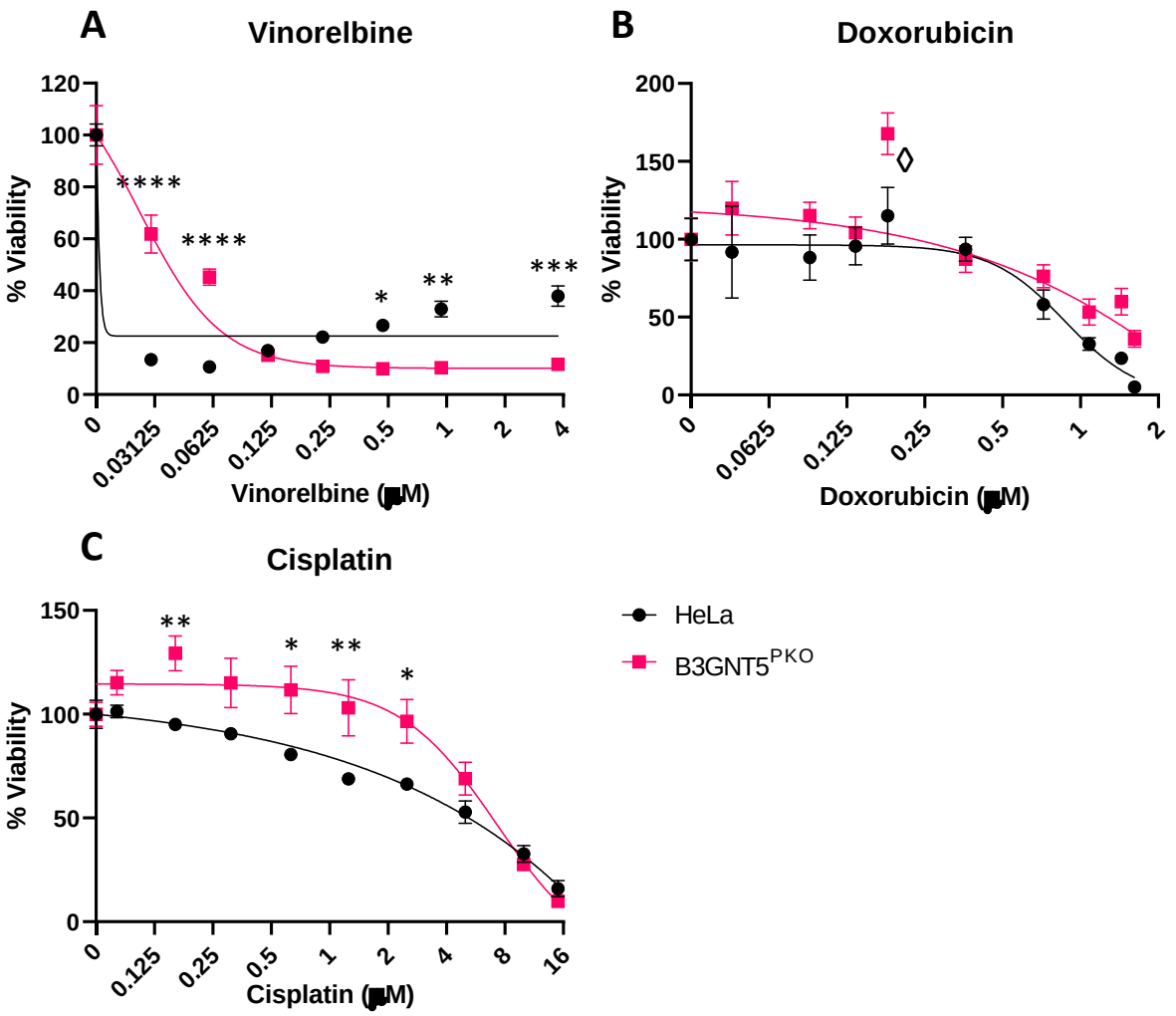

Figure 22. CCK-8 assay of HeLa vs HeLa B3GNT5^{PKO} treated with vinorelbine, doxorubicin, or cisplatin. In triplicate, HeLa and HeLa B3GNT5^{PKO} were treated with **A:** Vinorelbine (0-3.75 μM), **B:** Doxorubicin (0-1.62 μM), or **C:** Cisplatin (0-15 μM). 2-way ANOVA using Sidak multiple comparisons test was used. XY plot graphs were used with a log(2) X axis. Error bars represent SEM. Lines of best fit generated by nonlinear robust regression: inhibitor vs response, variable slope. Percent viability was calculated by averaging the absorbance values, dividing each drug concentration by the untreated group, then multiplying by 100. * $p \leq 0.05$; ** $p \leq 0.01$, *** $p \leq 0.001$, and **** $p \leq 0.0001$. ◊ indicates statistical outlier excluded from multiple comparisons test.

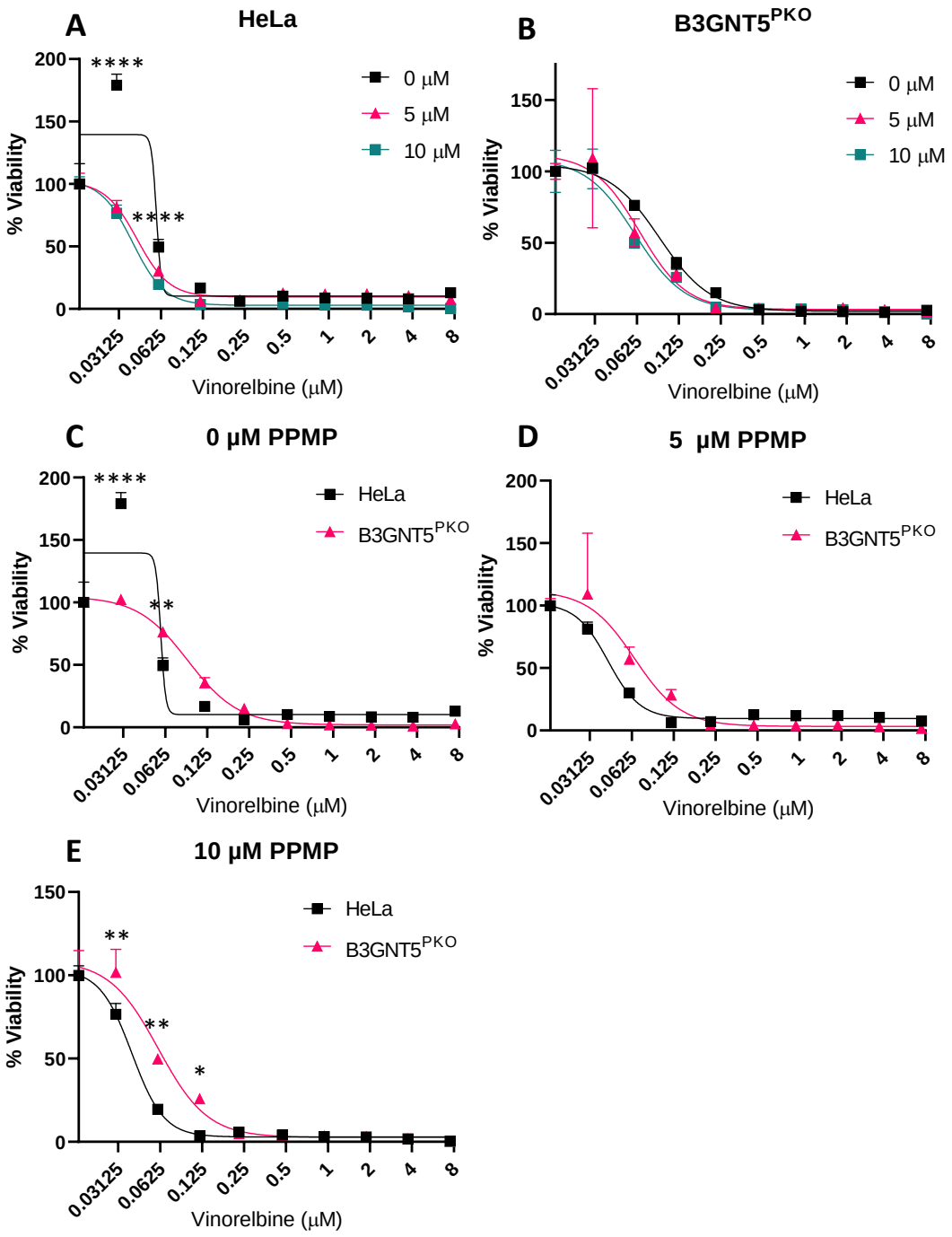

Figure 23. CCK-8 assay of HeLa and HeLa B3GNT5^{PKO} co-treated with vinorelbine and PPMP. In triplicate, HeLa and HeLa B3GNT5^{PKO} were treated with Vinorelbine (0-7.5 μM) and PPMP (0, 5, 10 μM). **A:** HeLa at all PPMP concentrations; significance shown for difference between 0 and 10 μM PPMP. **B:** B3GNT5^{PKO} at all PPMP concentrations. **C:** HeLa and HeLa B3GNT5^{PKO} with no PPMP (DMSO vehicle). **D:** HeLa and HeLa B3GNT5^{PKO} with 5 μM PPMP. **E:** HeLa and HeLa B3GNT5^{PKO} with 10 μM PPMP. 2-way ANOVA with Dunnett (A&B) or Sidak (C-E) multiple comparisons test was used. XY plot graphs were used with a log(2) X axis. Error bars represent SEM. Lines of best fit generated by nonlinear least squares regression: inhibitor vs response, variable slope. Percent viability was calculated by averaging the absorbance values, dividing each drug concentration by the control group, then multiplying by 100. * $p \leq 0.05$; ** $p \leq 0.01$, *** $p \leq 0.001$, and **** $p \leq 0.0001$; all other values are nonsignificant.

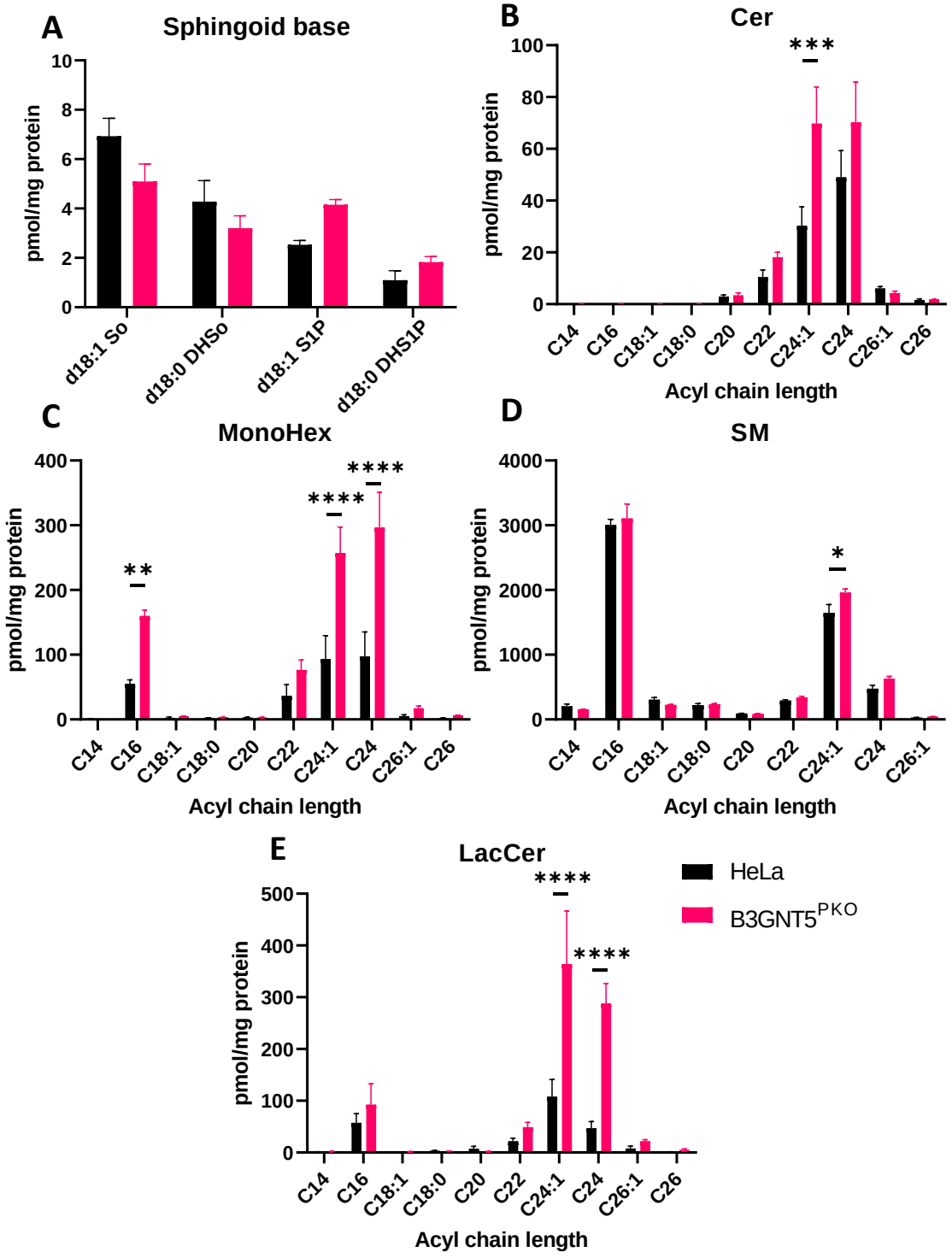

Figure 24. Sphingolipidomic Analysis of HeLa and HeLa B3GNT5^{PKO}. Triplicate samples of HeLa and HeLa B3GNT5^{PKO} were analyzed by MS. HeLa is shown in black and B3GNT5^{PKO} in magenta. **A:** concentration of So, DHSo, S1P, and DHS1P. **B:** Concentrations of C14-C26 ceramide. **C:** Concentrations of C14-C26 MonoHex. **D:** Concentrations of C14-C26:1 SM. E: Concentrations of C14-C26 LacCer. All samples were normalized to internal standards and initial sample concentration. 2-way ANOVA using Sidak multiple comparisons test was used. Grouped interleaved bar graphs showing mean and SEM bars were used. * $p \leq 0.05$; ** $p \leq 0.01$, *** $p \leq 0.001$, and **** $p \leq 0.0001$; all other values are nonsignificant.

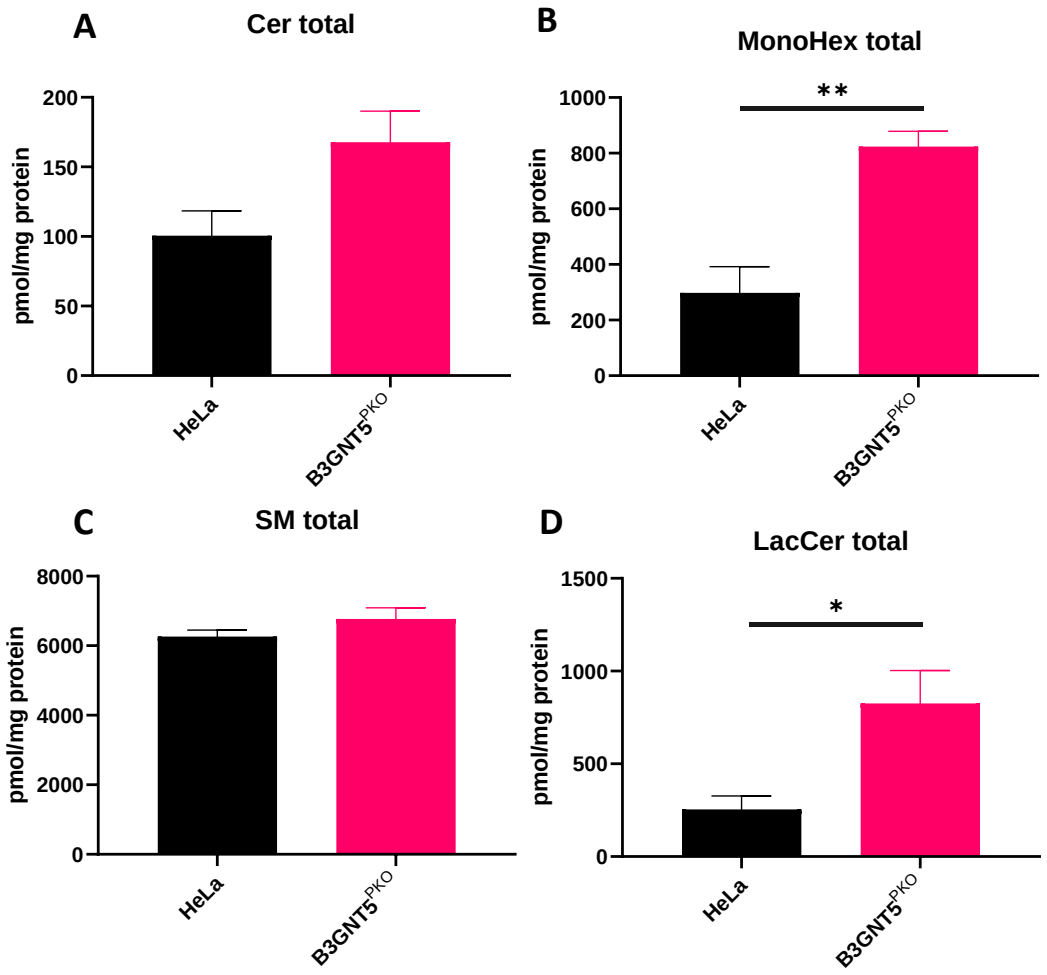

Figure 25. Total sphingolipid levels of HeLa and HeLa B3GNT5^{PKO}. Triplicate samples of HeLa and HeLa B3GNT5^{PKO} were analyzed by MS. HeLa is shown in black and B3GNT5^{PKO} in magenta. **A:** Total ceramide concentration. **B:** Total MonoHex concentration. **C:** Total SM concentration. **D:** Total LacCer concentration. All samples were normalized to internal standards and initial sample concentration. Holm-Sidak unpaired t tests were used. Bar graphs show mean and SEM bars. * $p \leq 0.05$; ** $p \leq 0.01$, *** $p \leq 0.001$, and **** $p \leq 0.0001$; all other values are nonsignificant.

Chapter 2 Tables

Table 4. p-values comparing combined HN tumor and normal samples by acyl chain length.

Acyl Chain Length	Cer	MonoHex	SM	LacCer	So/DHSo	S1P/DHS1P
C14	0.9985	>0.9999	0.7836	>0.9999		
C16	**<0.0001**	**<0.0001**	0.9999	**<0.0001**		
C18:1	>0.9999	>0.9999	0.9987	>0.9999	>0.9999	>0.9999
C18:0	0.9938	>0.9999	0.2136	>0.9999	0.5259	>0.9999
C20	0.5682	0.9966	0.9946	>0.9999		
C22	**0.0025**	>0.9999	>0.9999	0.4637		
C24:1	**<0.0001**	**0.0046**	0.9946	**<0.0001**		
C24	**<0.0001**	**<0.0001**	0.8606	**<0.0001**		
C26:1	**0.046**	**0.0372**	0.4037	>0.9999		
C26	**<0.0001**	0.0597		>0.9999		
Total	**<0.000001**	**0.000133**	0.664805	**<0.000001**		

Table 5. p-values comparing AA HN tumor and normal samples by acyl chain length.

Acyl Chain Length	Cer	MonoHex	SM	LacCer	So/DHSo	S1P/DHS1P
C14	0.9996	>0.9999	0.5585	>0.9999		
C16	**<0.0001**	**<0.0001**	0.2503	**<0.0001**		
C18:1	>0.9999	>0.9999	>0.9999	>0.9999	0.9336	>0.9999
C18:0	0.9996	>0.9999	0.1554	>0.9999	0.7242	>0.9999
C20	0.6607	0.9944	>0.9999	>0.9999		
C22	**0.0333**	0.9637	>0.9999	0.8858		
C24:1	**0.0034**	**0.0438**	>0.9999	**<0.0001**		
C24	**<0.0001**	**<0.0001**	0.81	**0.0041**		
C26:1	0.1516	0.108	0.7291	>0.9999		
C26	**0.0005**	0.3114		>0.9999		
Total	**<0.0001**	**0.0013**	>0.9999	**0.0006**		

Table 6. p-values comparing Cau HN tumor and normal samples by acyl chain length.

Acyl Chain Length	Cer	MonoHex	SM	LacCer	So/DHSo	S1P/DHS1P
C14	>0.9999	>0.9999	>0.9999	>0.9999		
C16	**<0.0001**	**<0.0001**	0.1433	**<0.0001**		
C18:1	>0.9999	>0.9999	0.9995	>0.9999	>0.9999	>0.9999
C18:0	0.9998	>0.9999	0.9808	>0.9999	0.6021	>0.9999
C20	0.9941	>0.9999	0.9875	>0.9999		
C22	0.2276	0.9995	>0.9999	0.8447		
C24:1	**0.0768**	0.351	0.8445	**<0.0001**		
C24	**<0.0001**	**<0.0001**	0.9997	**0.0042**		
C26:1	0.696	0.8108	0.8866	>0.9999		
C26	**0.0033**	0.5459		>0.9999		
Total	**0.0005**	0.2025	0.9919	**0.0002**		

Chapter 2 Figures

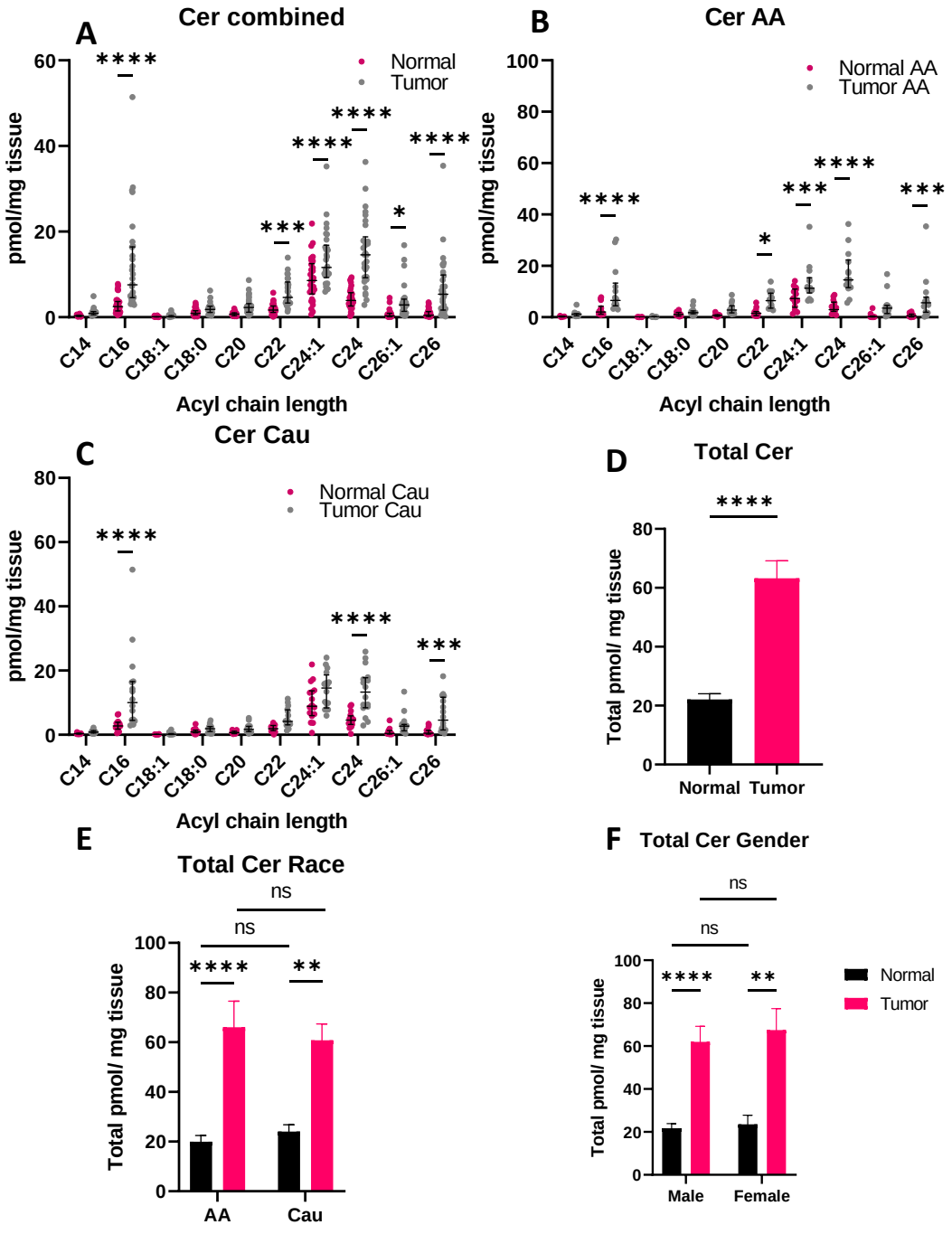

Figure 26. Head and neck Cer sphingolipid analysis. 60 paired head and neck normal and tumor tissues were analyzed by MS. **A:** Concentrations of C14-C26 Cer in African American and Caucasian samples combined (n=60). **B:** Concentrations of C14-C26 Cer in African American samples (n=28). **C:** Concentrations of C14-C26 Cer in Caucasian samples (n=32). **D:** Total Cer levels in combined samples. **E:** Total Cer levels broken down by race. **F:** Total Cer levels broken down by gender. All samples were normalized to internal standards and tissue weight. 2-way ANOVA using Sidak multiple comparisons test and Holm-Sidak unpaired t tests were used. Grouped interleaved scatter plots showing SEM bars and median box plot (A-C) or mean (D-F) were used. * $p \leq 0.05$; ** $p \leq 0.01$, *** $p \leq 0.001$, and **** $p \leq 0.0001$; all other values are nonsignificant.

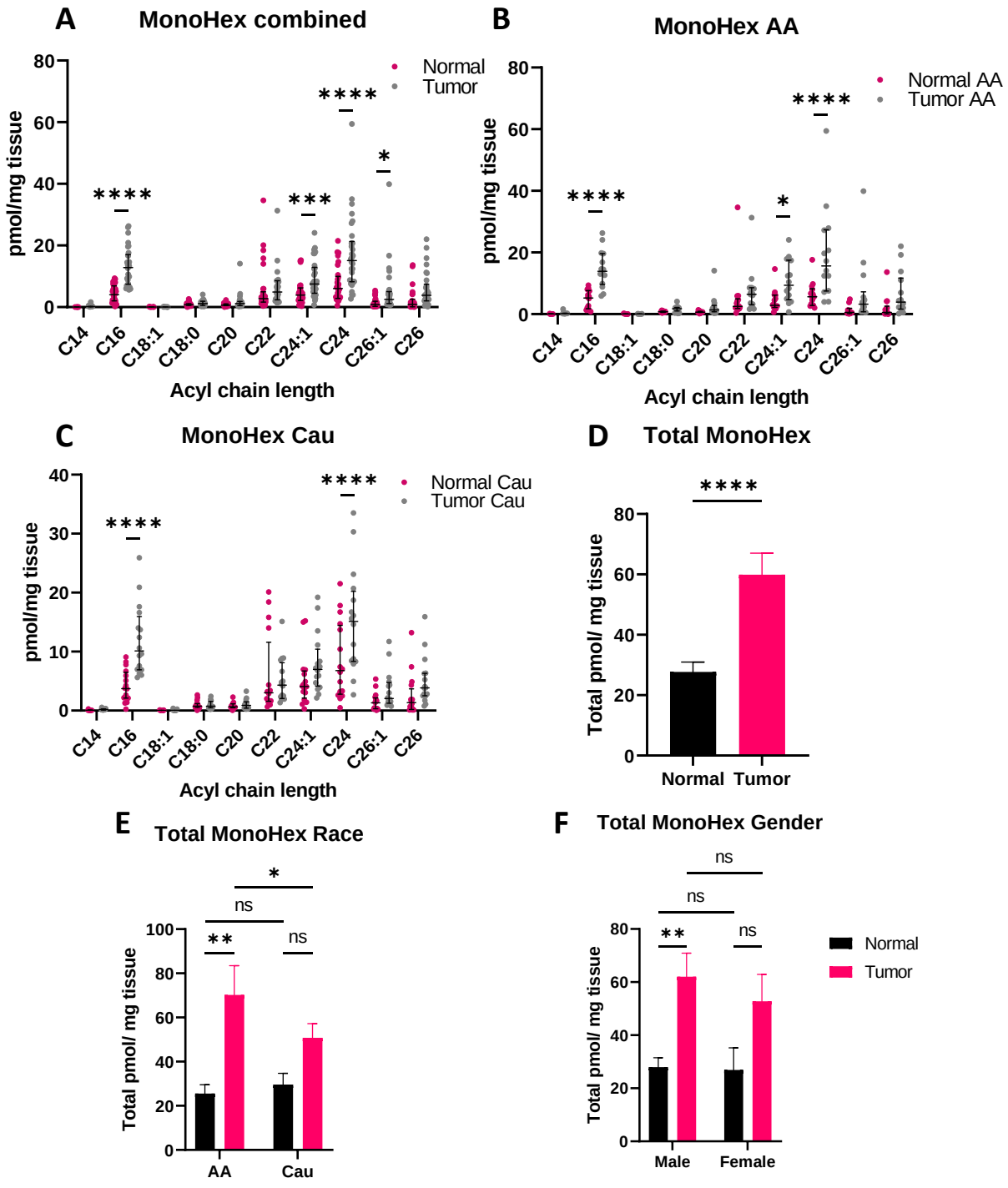

Figure 27. Head and neck MonoHex sphingolipid analysis. 60 paired head and neck normal and tumor tissues were analyzed by MS. **A:** Concentrations of C14-C26 MonoHex in African American and Caucasian samples combined (n=60). **B:** Concentrations of C14-C26 MonoHex in African American samples (n=28). **C:** Concentrations of C14-C26MonoHex in Caucasian samples (n=32). **D:** Total MonoHex levels in combined samples. **E:** Total MonoHex levels broken down by race. **F:** Total MonoHex levels broken down by gender. All samples were normalized to internal standards and tissue weight. 2-way ANOVA using Sidak multiple comparisons test and Holm-Sidak unpaired t tests were used. Grouped interleaved scatter plots showing SEM bars and median box plot (A-C) or mean (D-F) were used. * $p \leq 0.05$; ** $p \leq 0.01$, *** $p \leq 0.001$, and **** $p \leq 0.0001$; all other values are nonsignificant.

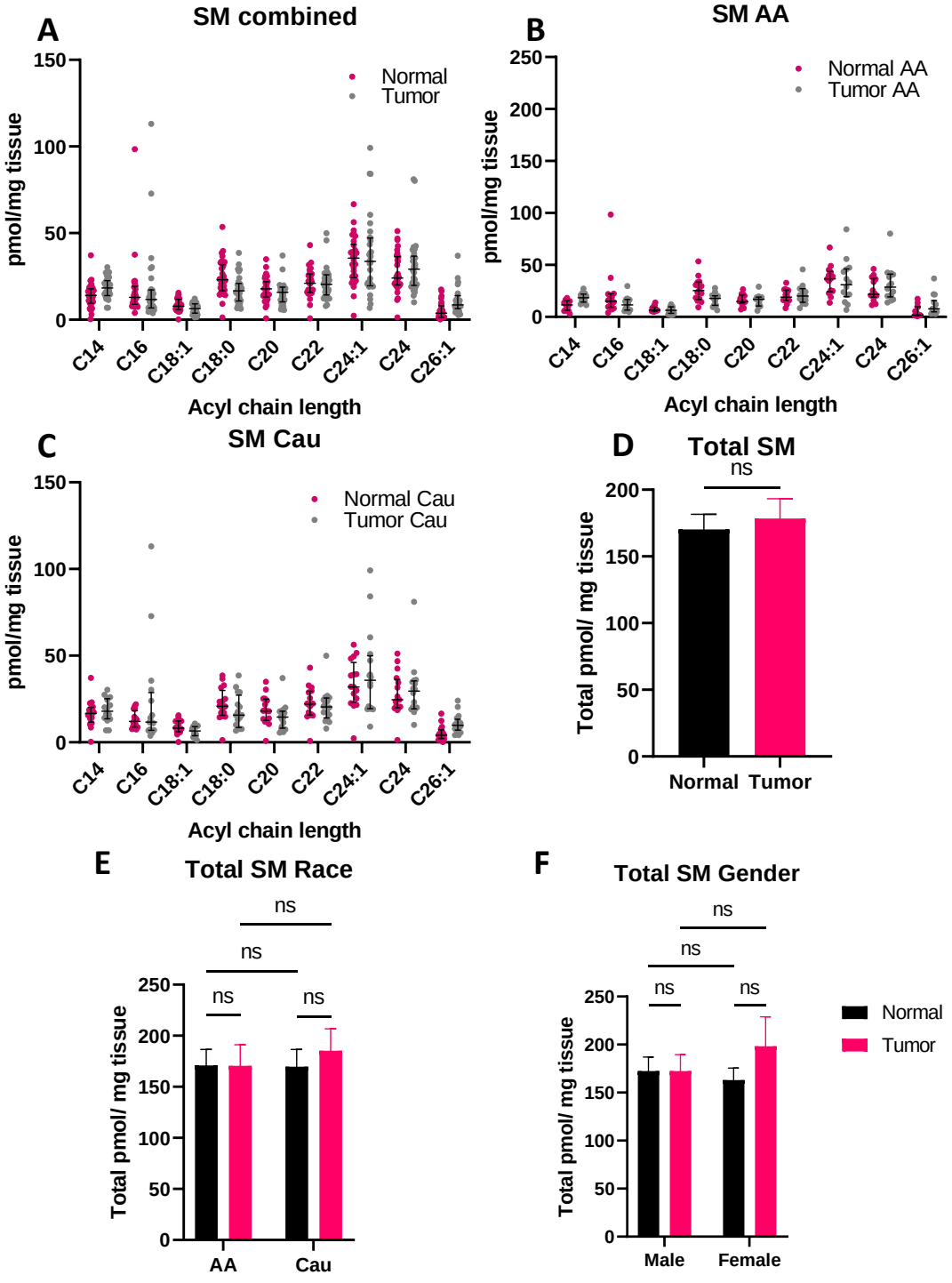

Figure 28. Head and neck SM sphingolipid analysis. 60 paired head and neck normal and tumor tissues were analyzed by MS. C26 SM excluded due to limitations in quantification range. **A:** Concentrations of C14-C26:1 SM in African American and Caucasian samples combined (n=60). **B:** Concentrations of C14-C26:1 SM in African American samples (n=28). **C:** Concentrations of C14-C26:1 SM in Caucasian samples (n=32). **D:** Total SM levels in combined samples. **E:** Total SM levels broken down by race. **F:** Total SM levels broken down by gender. All samples were normalized to internal standards and tissue weight. 2-way ANOVA using Sidak multiple comparisons test and Holm-Sidak unpaired t tests were used. Grouped interleaved scatter plots showing SEM bars and median box plot (A-C) or mean (D-F) were used. All values are nonsignificant.

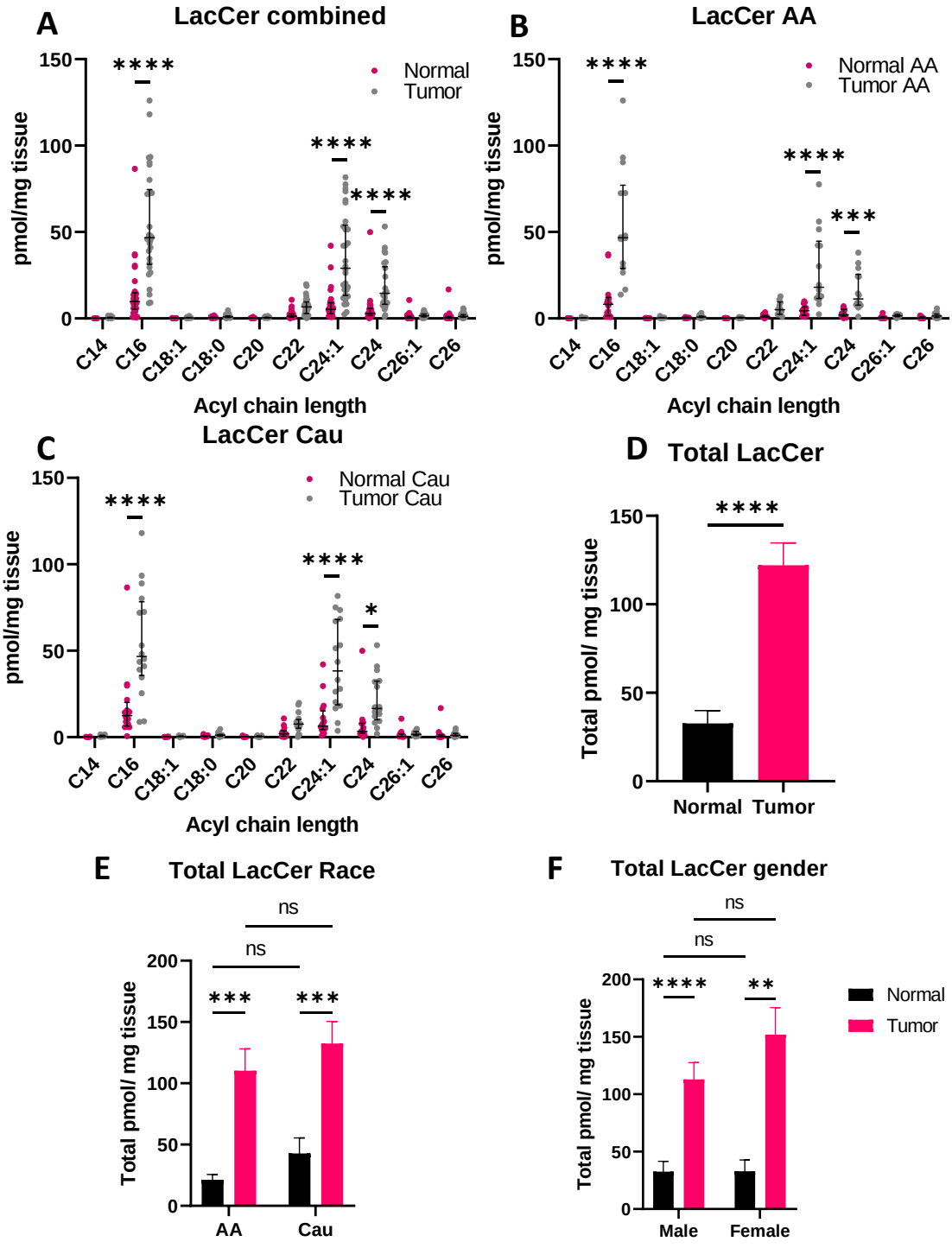

Figure 29. Head and neck LacCer sphingolipid analysis. 60 paired head and neck normal and tumor tissues were analyzed by MS. **A:** Concentrations of C14-C26 LacCer in African American and Caucasian samples combined (n=60). **B:** Concentrations of C14-C26 LacCer in African American samples (n=28). **C:** Concentrations of C14-C26 LacCer in Caucasian samples (n=32). **D:** Total LacCer levels in combined samples. **E:** Total LacCer levels broken down by race. **F:** Total LacCer levels broken down by gender. All samples were normalized to internal standards and tissue weight. 2-way ANOVA using Sidak multiple comparisons test and Holm-Sidak unpaired t tests were used. Grouped interleaved scatter plots showing SEM bars and median box plot (A-C) or mean (D-F) were used. * $p \leq 0.05$; ** $p \leq 0.01$, *** $p \leq 0.001$, and **** $p \leq 0.0001$; all other values are nonsignificant.

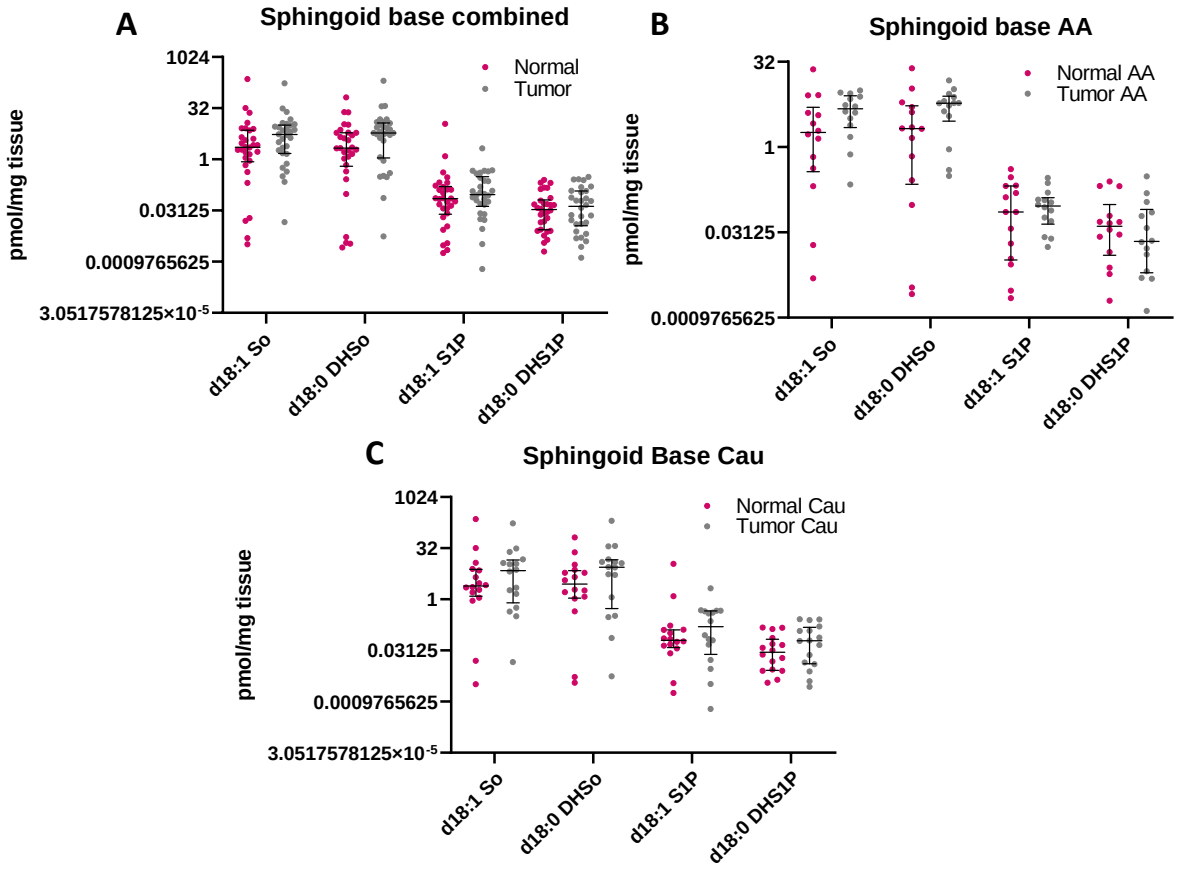

Figure 30. Head and neck sphingoid base analysis. 60 paired head and neck normal and tumor tissues were analyzed by MS. **A:** Concentrations of So, DHSo, S1P, and DHS1P in African American and Caucasian samples combined (n=60). **B:** Concentrations of So, DHSo, S1P, and DHS1P in African American samples (n=28). **C:** Concentrations So, DHSo, S1P, and DHS1P in Caucasian samples (n=32). All samples were normalized to internal standards and tissue weight. 2-way ANOVA using Sidak's multiple comparisons test was used. Grouped interleaved scatter plots showing SEM bars and median box plot were used, with the y-axis using log(2) scale. All values are nonsignificant.

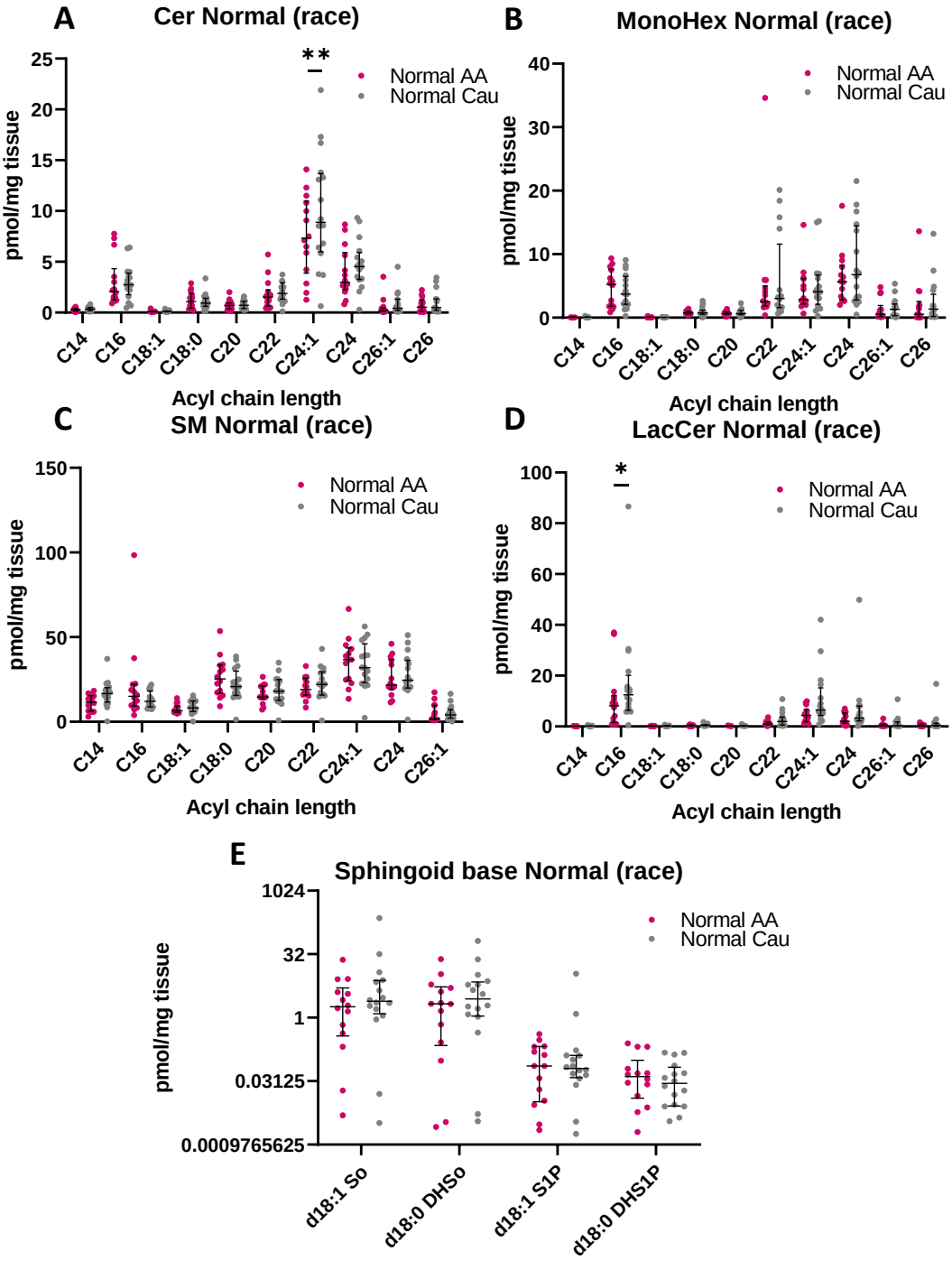

Figure 31. Comparison of sphingolipids in normal tissues by race. 30 head and neck normal tissues were analyzed by race (AA n=14, Cau n=16) by MS. **A:** Concentrations of Cer in African American and Caucasian normal tissues. **B:** Concentrations of SM in African American and Caucasian normal tissues. **C:** Concentrations of MonoHex in African American and Caucasian normal tissues. **D:** Concentrations of LacCer in African American and Caucasian normal tissues. **E:** Concentrations of So, DHSo, S1P, and DHS1P in African American and Caucasian normal tissues with a log(2) y-axis. All samples were normalized to internal standards and tissue weight. 2-way ANOVA using Sidak's multiple comparisons test was used. Grouped interleaved scatter plots showing SEM bars and median box plot were used. ns represents not significant; * $p \leq 0.05$; ** $p \leq 0.01$, *** $p \leq 0.001$, and **** $p \leq 0.0001$.

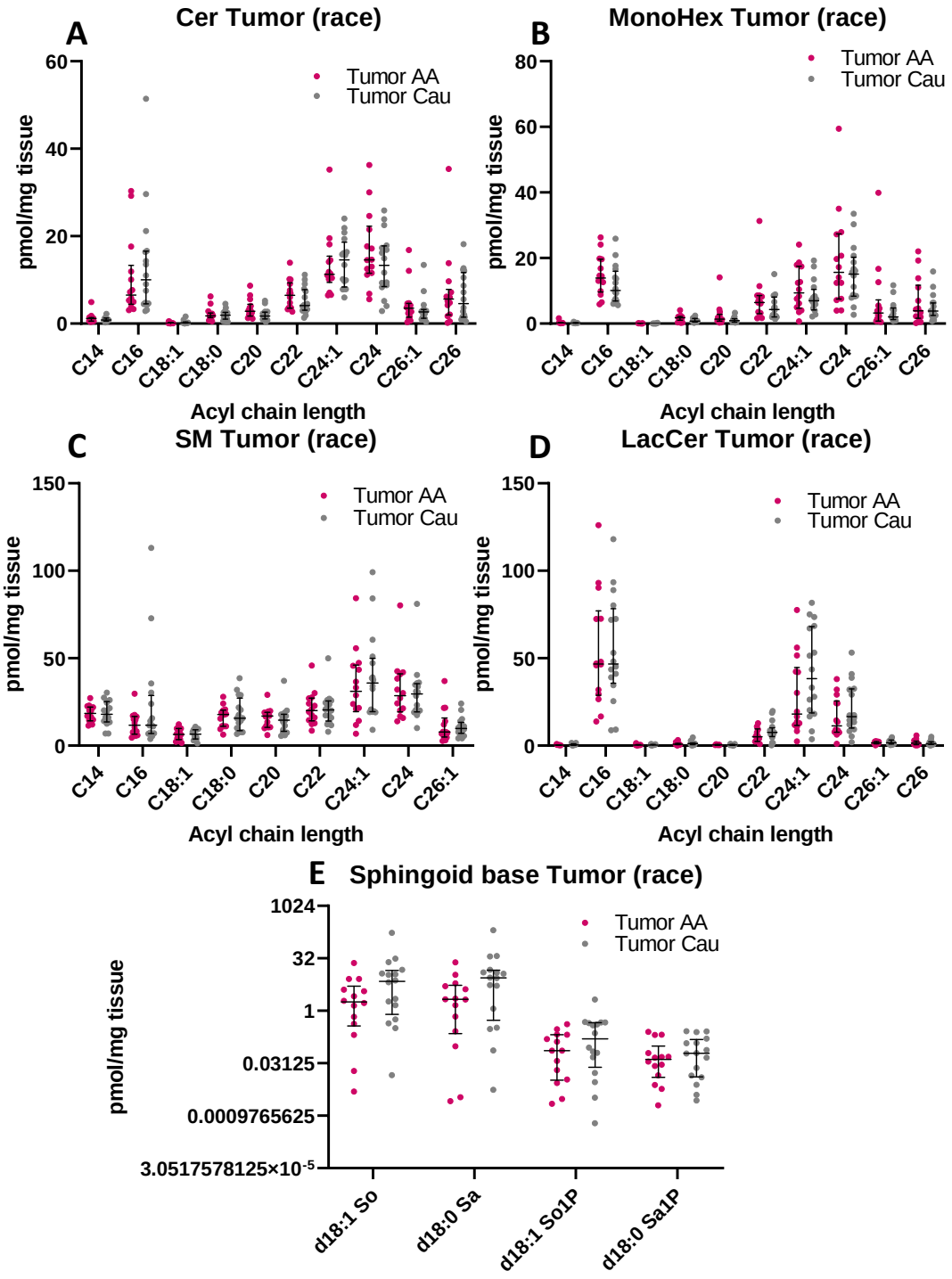

Figure 32. Comparison of sphingolipids in tumor tissues by race. 30 head and neck tumor tissues were analyzed by race (AA n=14, Cau n=16) by MS. **A:** Concentrations of Cer in African American and Caucasian tumor tissues. **B:** Concentrations of SM in African American and Caucasian tumor tissues. **C:** Concentrations of MonoHex in African American and Caucasian tumor tissues. **D:** Concentrations of LacCer in African American and Caucasian tumor tissues. **E:** Concentrations of So, DHSo, S1P, and DHS1P in African American and Caucasian normal tissues (with a log(2) y-axis). All samples were normalized to internal standards and tissue weight. 2-way ANOVA using Sidak's multiple comparisons test was used. Grouped interleaved scatter plots showing SEM bars and median box plot were used. All values are nonsignificant.

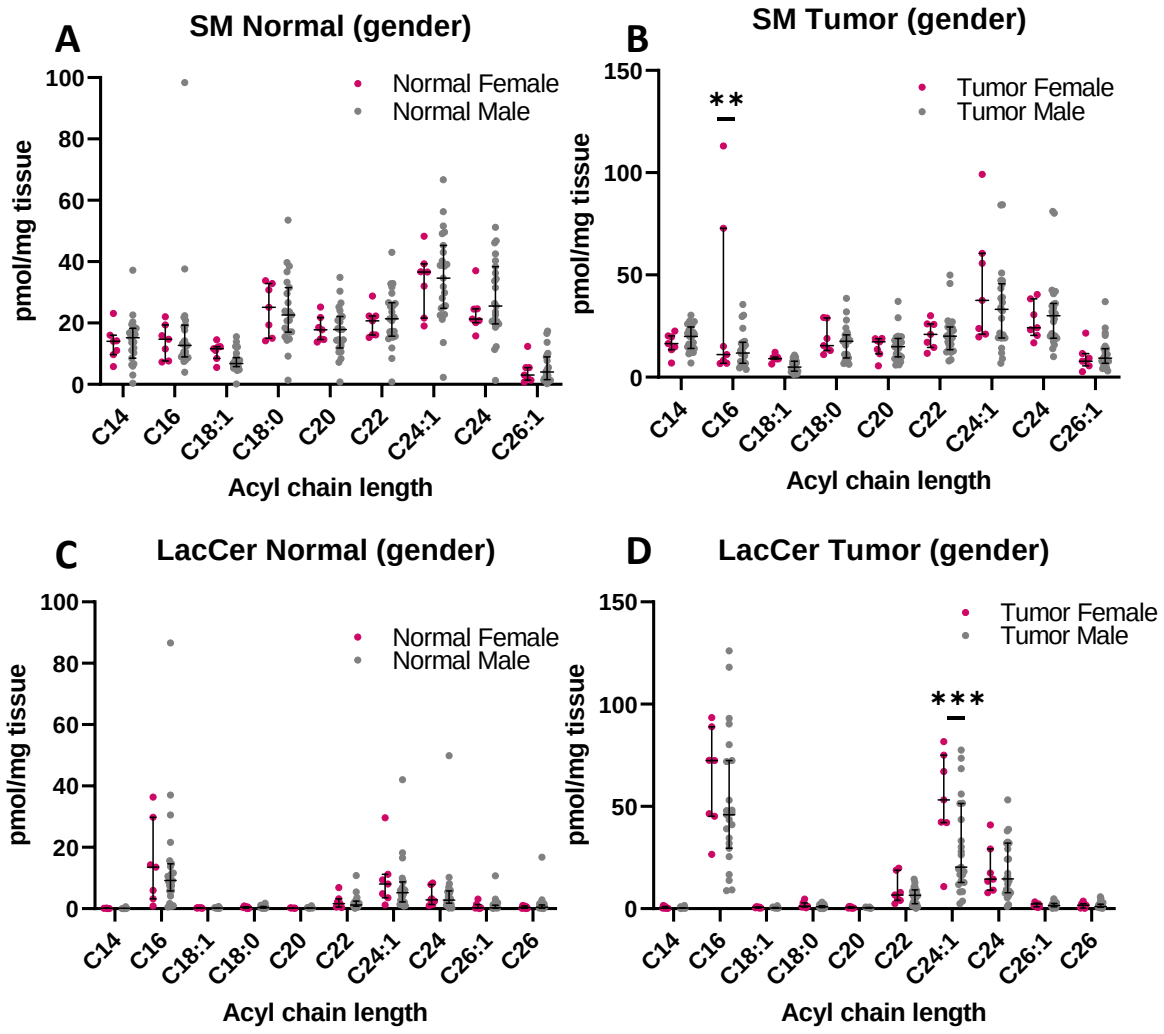

Figure 33. Comparison of SM and LacCer by Gender. 60 paired head and neck normal and tumor tissues were analyzed by MS (Female n=7, Male n=23 for both normal and tumor). Both normal and tumor tissues were insignificant at all chain lengths for Cer, MonoHex, and So/DHSo/S1P/DHS1P. **A:** Concentrations of SM in male and female HN normal tissues. **B:** Concentrations of SM in male and female HN tumor tissues. **C:** Concentrations of LacCer in male and female HN normal tissues. **D:** Concentrations of LacCer in male and female HN tumor tissues. All samples were normalized to internal standards and tissue weight. 2-way ANOVA using Sidak's multiple comparisons test was used. interleaved scatter plots showing SEM bars and median box plot were used. * $p \leq 0.05$, ** $p \leq 0.01$, *** $p \leq 0.001$, and **** $p \leq 0.0001$; all other measurements are non-significant.

References

1. Ogretmen B. Sphingolipid metabolism in cancer signalling and therapy. Nature reviews. Cancer. 2018 Jan;18(1):33-50.

2. Newton J, Lima S, Maceyka M, Spiegel S. Revisiting the sphingolipid rheostat: Evolving concepts in cancer therapy. Experimental Cell Research. 2015 May 1,;333(2):195-200.

3. Chen Y, Liu Y, Sullards M, Merrill Jr A. An Introduction to Sphingolipid Metabolism and Analysis by New Technologies. Neuromol Med. 2010 Dec;12(4):306-19.

4. Bartke N, Hannun YA. Bioactive sphingolipids: metabolism and function. Journal of Lipid Research. 2009 /04/01;50:S91-6.

5. D'Angelo G, Capasso S, Sticco L, Russo D. Glycosphingolipids: synthesis and functions. The FEBS Journal. 2013;280(24):6338-53.

6. Schnaar RL, Kinoshita T. Glycosphingolipids. In: Varki A, Cummings RD, Esko JD, Stanley P, Hart GW, Aebi M, et al, editors. Essentials of Glycobiology. 3rd ed. Cold Spring Harbor (NY): Cold Spring Harbor Laboratory Press; 2015.

7. Regina Todeschini A, Hakomori S. Functional role of glycosphingolipids and gangliosides in control of cell adhesion, motility, and growth, through glycosynaptic microdomains. Biochimica et Biophysica Acta (BBA) - General Subjects. 2008 March 1,;1780(3):421-33.

8. Furukawa K, Ohmi Y, Ohkawa Y, Bhuiyan RH, Zhang P, Tajima O, et al. New era of research on cancer-associated glycosphingolipids. Cancer Science. 2019 May;110(5):1544-51.

9. Potapenko IO, Lüders T, Russnes HG, Helland Å, Sørlie T, Kristensen VN, et al. Glycan-related gene expression signatures in breast cancer subtypes; relation to survival. Molecular Oncology. 2015 April 1,;9(4):861-76.

10. Zhuo D, Li X, Guan F. Biological Roles of Aberrantly Expressed Glycosphingolipids and Related Enzymes in Human Cancer Development and Progression. Frontiers in physiology. 2018;9:466.

11. Liang Y, Wang C, Wang I, Chen Y, Li L, Lin C, et al. Interaction of glycosphingolipids GD3 and GD2 with growth factor receptors maintains breast cancer stem cell phenotype. Oncotarget. 2017 Jul 18,;8(29):47454-73.

12. Guan F, Handa K, Hakomori S. Specific Glycosphingolipids Mediate Epithelial-to-Mesenchymal Transition of Human and Mouse Epithelial Cell Lines. Proceedings of the National Academy of Sciences - PNAS. 2009 May 5,;106(18):7461-6.

13. Tyler A, Johansson A, Karlsson T, Gudey SK, Brännström T, Grankvist K, et al. Targeting glucosylceramide synthase induction of cell surface globotriaosylceramide (Gb3) in acquired

cisplatin-resistance of lung cancer and malignant pleural mesothelioma cells. Experimental Cell Research. 2015 August 1,;336(1):23-32.

14. Hasegawa H, Yamashita K, Otubo D, Fujii S, Kamigaki T, Kuroda D, et al. Allogeneic DCG promote lung NK cell activation and antitumor effect after invariant NKT cell activation. Anticancer research. 2014 Jul;34(7):3411-7.

15. Nozaki H, Yanagida M, Koide K, Shiotani K, Kinoshita M, Kobayashi Y, et al. Production and characterization of monoclonal antibodies specific to lactotriaosylceramide. Glycobiology. 2010 /12/01;20(12):1631-42.

16. Kanehisa M, Goto S. KEGG: Kyoto Encyclopedia of Genes and Genomes. Nucleic Acids Res. 2000 Jan 01,;28(1):27-30.

17. Togayachi A, Akashima T, Ookubo R, Kudo T, Nishihara S, Iwasaki H, et al. Molecular Cloning and Characterization of UDP-GlcNAc:Lactosylceramide β1,3-N-Acetylglucosaminyltransferase (β3Gn-T5), an Essential Enzyme for the Expression of HNK-1 and Lewis X Epitopes on Glycolipids. J Biol Chem. 2001 06/22/;276(25):22032-40.

18. Togayachi A, Kozono Y, Ikehara Y, Ito H, Suzuki N, Tsunoda Y, et al. Lack of lacto/neolacto-glycolipids enhances the formation of glycolipid-enriched microdomains, facilitating B cell activation. Proc Natl Acad Sci U S A. 2010 -6-29;107(26):11900-5.

19. Uhlen M, Zhang C, Lee S, Sjöstedt E, Fagerberg L, Bidkhori G, et al. A pathology atlas of the human cancer transcriptome. Science. 2017 08 18,;357(6352).

20. Wang Z, Wen L, Ma X, Chen Z, Yu Y, Zhu J, et al. High expression of lactotriaosylceramide, a differentiation-associated glycosphingolipid, in the bone marrow of acute myeloid leukemia patients. Glycobiology. 2012 Jul;22(7):930-8.

21. Etcheverry A, Aubry M, de Tayrac M, Vauleon E, Boniface R, Guenot F, et al. DNA methylation in glioblastoma: impact on gene expression and clinical outcome. BMC genomics. 2010 Dec 14,;11(1):701.

22. Newnham GM, Conron M, McLachlan S, Dobrovic A, Do H, Li J, et al. Integrated mutation, copy number and expression profiling in resectable non-small cell lung cancer. BMC cancer. 2011 Mar 7,;11(1):93.

23. Leiphrakpam PD, Patil PP, Remmers N, Swanson B, Grandgenett PM, Qiu F, et al. Role of keratan sulfate expression in human pancreatic cancer malignancy. Scientific Reports. 2019;9(1):9665.

24. Cerami E, Gao J, Dogrusoz U, Gross BE, Sumer SO, Aksoy BA, et al. The cBio Cancer Genomics Portal: An Open Platform for Exploring Multidimensional Cancer Genomics Data. Cancer Discov. 2012 -05-01 00:00:00;2(5):401-4.

25. Marcos NT, Magalhães A, Ferreira B, Oliveira MJ, Carvalho AS, Mendes N, et al. Helicobacter pylori induces β3GnT5 in human gastric cell lines, modulating expression of the SabA ligand sialyl–Lewis x. Journal of Clinical Investigation. 2008 May 1,;118(6):2325-36.

26. Magalhães A, Marcos-Pinto R, Nairn AV, dela Rosa M, Ferreira RM, Junqueira-Neto S, et al. Helicobacter pylori chronic infection and mucosal inflammation switches the human gastric glycosylation pathways. Biochimica et biophysica acta. 1961;1852(9):1928-39.

27. Astudillo L, Therville N, Colacios C, Ségui B, Andrieu-Abadie N, Levade T. Glucosylceramidases and malignancies in mammals. Biochimie. 2016 June 1,;125:267-80.

28. Liu Y, Li Y. Ceramide Glycosylation Catalyzed by Glucosylceramide Synthase and Cancer Drug Resistance. Adv Cancer Res. 2013;117:59-89.

29. Shayman JA. ELIGLUSTAT TARTRATE. Drugs Future. 2010 -8-1;35(8):613-20.

30. Koybasi S, Senkal CE, Sundararaj K, Spassieva S, Bielawski J, Osta W, et al. Defects in Cell Growth Regulation by C18:0-Ceramide and Longevity Assurance Gene 1 in Human Head and Neck Squamous Cell Carcinomas. The Journal of biological chemistry. 2004 Oct 22,;279(43):44311-9.

31. Kanto T, Kalinski P, Hunter OC, Lotze MT, Amoscato AA. Ceramide mediates tumor-induced dendritic cell apoptosis. J Immunol. 2001 -10-01;167(7):3773-84.

32. Schiffmann S, Sandner J, Birod K, Wobst I, Angioni C, Ruckhäberle E, et al. Ceramide synthases and ceramide levels are increased in breast cancer tissue. Carcinogenesis. 2009 May 1,;30(5):745-52.

33. Kitatani K, Idkowiak-Baldys J, Hannun YA. The sphingolipid salvage pathway in ceramide metabolism and signaling. Cell Signal. 2008 -06;20(6):1010-8.

34. Brachtendorf S, El-Hindi K, Grösch S. Ceramide synthases in cancer therapy and chemoresistance. Progress in lipid research. 2019 Apr;74:160-85.

35. Schiffmann S, Birod K, Männich J, Eberle M, Wegner M, Wanger R, et al. Ceramide metabolism in mouse tissue. The International Journal of Biochemistry & Cell Biology. 2013 August 1,;45(8):1886-94.

36. Hartmann D, Lucks J, Fuchs S, Schiffmann S, Schreiber Y, Ferreirós N, et al. Long chain ceramides and very long chain ceramides have opposite effects on human breast and colon cancer cell growth. The International Journal of Biochemistry & Cell Biology. 2012 April 1,;44(4):620-8.

37. 293FT Cell Line [Internet]. [cited Jul 8, 2021]. Available from: https://www.thermofisher.com/order/catalog/product/R70007.

38. Lundberg AS, Randell SH, Stewart SA, Elenbaas B, Hartwell KA, Brooks MW, et al. Immortalization and transformation of primary human airway epithelial cells by gene transfer. Oncogene. 2002 -07-04;21(29):4577-86.

39. Rohrbach TD, Boyd AE, Grizzard PJ, Spiegel S, Allegood J, Lima S. A simple method for sphingolipid analysis of tissues embedded in optimal cutting temperature compound. Journal of lipid research. 2020 Jun;61(6):953.

40. Lee S, Lee DK. What is the proper way to apply the multiple comparison test? Korean J Anesthesiol. 2018 -10;71(5):353-60.

41. Outlier elimination and robust nonlinear regression [Internet]. [cited 08/13/2021]. Available from: https://www.graphpad.com/guides/prism/latest/curve-fitting/reg_robust_nonlinear_regresson_and.htm.

42. Marshall J. Transwell® Invasion Assays. In: Cell Migration. Totowa, NJ: Humana Press; 2011. p. 97-110.

43. Shaw LM. Tumor cell invasion assays. Methods in molecular biology (Clifton, N.J.). 2005;294:97-105.

44. Guy J, Espenel S, Vallard A, Battiston-Montagne P, Wozny A, Ardail D, et al. Evaluation of the Cell Invasion and Migration Process: A Comparison of the Video Microscope-based Scratch Wound Assay and the Boyden Chamber Assay. J Vis Exp. 2017 -11-17(129).

45. Kuribayashi K, Funaguchi N, Nakano T. Chemotherapy for advanced non-small cell lung cancer with a focus on squamous cell carcinoma. J Cancer Res Ther. 2016 Apr-Jun;12(2):528-34.

46. Kelland LR, Farrell NP. Platinum-Based Drugs in Cancer Therapy. Totowa, N.J.: Humana; 2000.

47. Alexander S, Swatson WS, Alexander H. Pharmacogenetics of Resistance to Cisplatin and Other Anticancer Drugs and the Role of Sphingolipid Metabolism. In: Dictyostelium discoideum Protocols. Totowa, NJ: Humana Press; 2013. p. 185-204.

48. Song M, Zang W, Zhang B, Cao J, Yang G. GCS overexpression is associated with multidrug resistance of human HCT-8 colon cancer cells. Journal of experimental & clinical cancer research. 2012 Mar 16,;31(1):23.

49. Chiu W, Su W, Li C, Chen C, Lin C. An increase in glucosylceramide synthase induces Bcl-xL-mediated cell survival in vinorelbine-resistant lung adenocarcinoma cells. Oncotarget. 2015 Aug 21,;6(24):20513-24.

50. Liu H, Fu Q, Lu Y, Zhang W, Yu P, Liu Z, et al. Anti-tubulin agent vinorelbine inhibits metastasis of cancer cells by regulating epithelial-mesenchymal transition. Eur J Med Chem. 2020;200:112332.

51. Vecchione L, Gambino V, Raaijmakers J, Schlicker A, Fumagalli A, Russo M, et al. A Vulnerability of a Subset of Colon Cancers with Potential Clinical Utility. Cell (Cambridge). 2016 Apr 7,;165(2):317-30.

52. Thomas P, Smart TG. HEK293 cell line: a vehicle for the expression of recombinant proteins. J Pharmacol Toxicol Methods. 2005 May-Jun;51(3):187-200.

53. Meng Q, Hu X, Zhao X, Kong X, Meng Y, Chen Y, et al. EBioMedicine. EBioMedicine. 2019 Jun 1,;44:250-60.

54. Therville N, Colacios C, Segui B, Andrieu-Abadie N, Levade T. Glucosylceramidases and malignancies in mammals. Biochimie. 2016 /06/01;125:267-80.

55. Lee L, Abe A, Shayman JA. Improved inhibitors of glucosylceramide synthase. The Journal of biological chemistry. 1999 May;274(21):14662–14669.

56. Adey A, Burton JN, Kitzman JO, Hiatt JB, Lewis AP, Martin BK, et al. The haplotype-resolved genome and epigenome of the aneuploid HeLa cancer cell line. Nature. 2013 -8-8;500(7461):207-11.

57. Biellmann F, Hülsmeier AJ, Zhou D, Cinelli P, Hennet T. The Lc3-synthase gene B3gnt5 is essential to pre-implantation development of the murine embryo. BMC developmental biology. 2008 Nov 12,;8(1):109.

58. Kuan C, Chang J, Mansson J, Li J, Pegram CN, Fredman P, et al. Multiple phenotypic changes in mice after knockout of the B3gnt5 gene, encoding Lc3 synthasea key enzyme in lacto-neolacto ganglioside synthesis. BMC Dev Biol. 2010 Nov 18,;10:114.

59. Merrill AH. Sphingolipid and Glycosphingolipid Metabolic Pathways in the Era of Sphingolipidomics. Chem Rev. 2011 -10-12;111(10):6387-422.

60. Li H, Kim WS, Guillemin GJ, Hill AF, Evin G, Garner B. Modulation of amyloid precursor protein processing by synthetic ceramide analogues. Biochimica et Biophysica Acta (BBA) - Molecular and Cell Biology of Lipids. 2010 August 1,;1801(8):887-95.

61. Gil Z, Fliss DM. Contemporary management of head and neck cancers. The Israel Medical Association journal. 2009 May;11(5):296-300.

62. Marur S, Forastiere AA. Head and Neck Cancer: Changing Epidemiology, Diagnosis, and Treatment. Mayo Clinic Proceedings. 2008 April 1,;83(4):489-501.

63. Senkal CE, Obeid LM. Sphingolipids in the Pathogenesis of Head and Neck and Lung Cancers: Translational Aspects for Therapy and Biomarker Development. Bioactive Sphingolipids in Cancer Biology and Therapy. 2015:235-57.

64. Molina MA, Cheung MC, Perez EA, Byrne MM, Franceschi D, Moffat FL, et al. African American and poor patients have a dramatically worse prognosis for head and neck cancer. Cancer. 2008 November 15,;113(10):2797-806.

65. Beckham TH, Elojeimy S, Cheng JC, Turner LS, Hoffman SR, Norris JS, et al. Targeting sphingolipid metabolism in head and neck cancer: rational therapeutic potentials. Expert Opinion on Therapeutic Targets. 2010 May 1,;14(5):529-39.

66. Sedić M, Grbčić P, Pavelić SK. Bioactive Sphingolipids as Biomarkers Predictive of Disease Severity and Treatment Response in Cancer: Current Status and Translational Challenges. Anticancer research. 2019 Jan;39(1):41-56.

67. Boyd AE, Allegood J, Lima S. Preparation of Human Tissues Embedded in Optimal Cutting Temperature Compound for Mass Spectrometry Analysis. JoVE (Journal of Visualized Experiments). 2021 /04/27(170):e62552.

68. Karahatay S, Thomas K, Koybasi S, Senkal CE, Elojeimy S, Liu X, et al. Clinical relevance of ceramide metabolism in the pathogenesis of human head and neck squamous cell carcinoma (HNSCC): attenuation of C(18)-ceramide in HNSCC tumors correlates with lymphovascular invasion and nodal metastasis. Cancer Lett. 2007 -10-18;256(1):101-11.

69. Chen L, Chen H, Li Y, Li L, Qiu Y, Ren J. Endocannabinoid and ceramide levels are altered in patients with colorectal cancer. Oncol Rep. 2015 -07;34(1):447-54.

70. Zhang X, Sakamoto W, Canals D, Ishibashi M, Matsuda M, Nishida K, et al. Ceramide synthase 2-C24:1-ceramide axis limits the metastatic potential of ovarian cancer cells. The FASEB Journal. 2021;35(2):e21287.

71. Fan S, Wang Y, Lu J, Zheng Y, Wu D, Zhang Z, et al. CERS2 Suppresses Tumor Cell Invasion and is Associated with Decreased V-ATPase and MMP-2/MMP-9 Activities in Breast Cancer. Journal of Cellular Biochemistry. 2015;116(4):502-13.

72. Moro K, Kawaguchi T, Tsuchida J, Gabriel E, Qi Q, Yan L, et al. Ceramide species are elevated in human breast cancer and are associated with less aggressiveness. Oncotarget. 2018 Apr 13,;9(28):19874-90.

73. Garner AE, Smith DA, Hooper NM. Sphingomyelin chain length influences the distribution of GPI-anchored proteins in rafts in supported lipid bilayers. Molecular Membrane Biology. 2007 January 1,;24(3):233-42.